UNIVERSIDAD COMPLUTENSE DE MADRID

FACULTAD DE CIENCIAS FÍSICAS

TeO2- BASED FILM GLASSES FOR PHOTONIC APPLICATIONS: STRUCTURAL AND OPTICAL PROPERTIES.

MEMORIA PARA OPTAR AL GRADO DE DOCTOR

PRESENTADA POR

David Muñoz Martín

Bajo la dirección del doctor

José Gonzalo de los Reyes

Madrid, 2010

- **ISBN: 978-84-693-1813-3**

TeO_2-based film glasses for photonic applications: structural and optical properties

David Muñoz Martín

Dirigida por el Dr. José Gonzalo de los Reyes

Memoria de tesis presentada en la
Facultad de Ciencias Físicas de
la Universidad Complutense de Madrid
para optar al grado de
Doctor en Ciencias Físicas

Consejo Superior de
Investigaciones Científicas

Laser Processing Group
Instituto de Óptica

Universidad
Complutense de Madrid

Madrid, septiembre 2009

A mi madre Mercedes

Si comienza uno con certezas, terminará
con dudas; mas si se conforma en
comenzar con dudas, llegará a certezas.
Francis Bacon

Agradecimientos

Una memoria de tesis nunca estaría completa sin recordar a todos aquellos que me han ayudado con el trabajo experimental, con el de redacción o que simplemente han estado allí cuando la tesis me saturó.

En primer lugar, es casi obligatorio situar a mi director de tesis. Gracias Pepe por tu cercania y tu ánimo, por las discusiones científicas en las que siempre estuviste dispuesto a escuchar mis opiniones y por los consejos de todo tipo durante la redaccón de este texto.

Agradezco también el apoyo de todos los miembros del Grupo de Procesado por Láser del Instituto de Óptica: A Carmen Nieves Afonso por confiar en mi y darme esta oportunidad y que además, junto con Jesús, Lorena y Alejandro, ha caracterizado las guias depositadas. Al "equipo no lineal" (Javier Solís, Héctor y Álex) por nuestras largas, pero finalmente productivas, discusiones sobre las propiedades ópticas no lineales. A José María Fernández Navarro por ser mi maestro en el mundo vidriero y en la cocina alemana. A Rosalía Serna y a Pablo por sus intentos con las medidas de fotoluminiscencia. A Miguel Jiménez por ayudarme con las medidas de absorción. Y a Jan Siegel por sus comentarios durante el proceso de escritura. Un agradecimiento especial para Ángel Perea por todas las veces que le he llamado gritando socorro desde el laboratorio.

Además agradezco a todo el personal de servicios del Instituto de Óptica, porque sin ellos ni mi tesis ni ningún otro trabajo de investigación sería posible. En especial, gracias al personal de gerencia (Eloy), de secretaría (Chary, Encarnita y Eva) y de de los talleres mecánico (Benito y Luis) y de vidrio (José).

La caracterización estructural de vidrios masivos no habría sido posible sin las aportaciones de Mª Ángeles Villegas, mientras que la caracterización composicional y estructural de las láminas depositadas me ha llevado a colaborar con varios investigadores externos al Instituto, cuyas contribuciones específicas

he preferido detallar en el capitulo dedicado a las técnicas experimentales usadas. Gracias a todos por vuestra ayuda.

Al personal de la secretaría de la Facultad de Física y del Departamento de Óptica de la Universidad Complutense y en especial a Gemma Piquero, Julio Serna y Rosa Weigand, por su ayuda con todos los trámites realizados.

Como personal investigador en formación, debo agradecer también al CSIC y a su programa JAE por la financiación de mi trabajo.

He compartido además estos cuatro años con muchas personas que, aun no estando todos directamente relacionados con mi trabajo, siempre me han ayudado a sobrevivir a la tesis y dado razones para seguir adelante. Siento no tener espacio para todos, pero me gustaría recordar especialmente a algunos de vosotros: A Sara, mi "compañera de piso", porque juntos hemos compartido las penurias de un becario del laboratorio 026. A Dani, por ser la "conciencia política" (si es que eso existe) del instituto. A Marcial, nuestro programador de LabView y chico-para-todo, sin ti esta tesis nunca habría podido hacerse. A Andrés, por enseñarme el abc del LaTeX. A Lorena e Isi, por su constante trabajo con la informática del grupo. A Vincenzo, por ser la primera persona que me enseñó el mundo PLD. A Victor por su simpatía. A Oscar, porque parte de este trabajo es una continuación del suyo. A los visionarios (Alberto, Enrique, Lucie, Lourdes, Patricia, Sergio, Carlos) y a los de las imagenes (Noemí, Elena, Rafa), porque simpre habéis estado dispuestos en comidas o cafés a oírme quejarme.

Gracias a todos los que estáis metidos en el IOSA porque la ciencia debe ser más que estar en un laboratorio encerrado. Las conferencias a chavales o la feria científica las recordaré siempre como uno de los mejores momentos de mi tesis.

A mis amigos de Guadalajara y de la carrera, porque su apoyo y preocupación por mi trabajo han sido constantes e incondicionales. En especial he de dar las gracias a José Alberto por su trabajo de corrector del inglés del texto.

He dejado para el final el agradeciemiento más sentido. Gracias a mis padres, Javier y Mercedes, que siempre han pensado que la educación es el mejor regalo que se le puede dar a un hijo. Ellos me han apoyado en todas las ideas extravagantes que he tenido, como estudiar física o hacer una tesis doctoral... Gracias por último a Bego, que ha aguantado y sufrido pacientemente mis neuras durante estos años y que llegado el momento ha trabajado de verdad para que este ejemplar que lees este impreso y presentado en la universidad.

Guadalajara, agosto de 2009

Contents

Chapter 1

Introduction

The last major scientific revolution has been, without any doubt, the spectacular development of the telecommunication technologies. Nowadays, mobile phones and the access to a massive amount of information through the Internet have changed the way people are connected to the world. Among the bases of this scientific, technological, and social change are the optical telecommunication systems, which allow the transmission of a much bigger amount of information ($\sim$ Gbit s^{-1}) than the classic transmission media such as radio waves ($\sim$ kbit s^{-1}) or copper wires ($\sim$ Mbit s^{-1}) at lower costs.[1]

Optical telecommunication networks are based on signal transmission through optical fibers with extremely low attenuation. For example, a single mode SiO_2 silicon fiber has an attenuation of $\sim$ 0.2 dB Km^{-1} at a wavelength of 1.5 μm, which allows the transmission of signals at distances of $\sim$ 100 Km at rates of several Gbit s^{-1} without any electronic regeneration.[2] Optical fibers are combined with optical amplifiers like the Er-doped fiber amplifier (EDFA), that allows amplifying the signal while it is propagating along the fiber,[3] and with the dense wavelength division multiplexing (DWDM) protocol, which allows dividing the optical transmission window into hundreds of closely packed wavelength bands, thus increasing the number of signals sent together.[4, 5] These improvements have greatly increased the capacity of fibers to transmit a large number of signals at long distances with a very high data transmission rate ($\sim$ 100 Gbit s^{-1}).

However, the telecommunication industry demands continuously larger bandwidths to meet the fast increase of traffic in the Internet, which was more than 9 Pbit per day in 2007, and which is expected to more than double to 21 Pbit per day by 2012, implying networks supporting transmission rates in the order

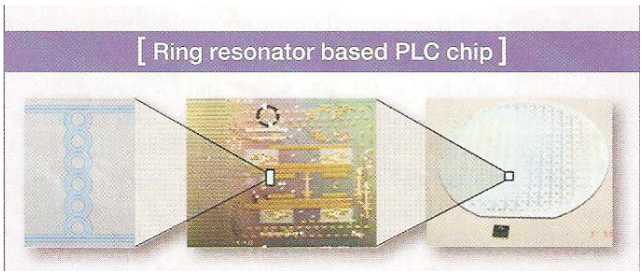

Figure 1.1: Microring resonator assembled to form large Si-based integrated optical chips (Planar Waveguide Circuits, PLC) designed by Infinera Corp. These PLC can then fabricated by hundreds to cover a large Si wafer. Figure taken from ref. [10].

of several Tbit s^{-1}.[6] These rates cannot be provided by the present network architectures that typically consist of electronic boxes (switches and routers) interconnected by pipes (point-to-point optical transmission systems). Although each pipe can provide a huge transmission capacity, the current boxes-and-pipes network architecture has certain limitations: the electronic box connected at the end of each pipe should be powerful and fast enough to process all the incoming traffic. However, this is not the case, and these electronic devices cause a data flow bottleneck due to their slow processing and transmission rates when compared to optical fibers.[4] The introduction of all-optical processing techniques will allow relieving the electronic bottleneck and enabling the future development of high-capacity digital all-optical photonic networks.[7]

Moreover, the successful application of this new all-optical devices in real networks depends not only on their capability for the optical processing of signals but also on their production on integrated configurations, since this implies size reduction, production costs savings, low power consumption and compatibility with the current fiber technology.[8, 9] For example, Figure 1.1 shows an image of a commercial planar waveguide device including an optical ring resonator, integrated in a Si wafer.[10]

The development of such all-optical integrated devices is a complex task due to the problems associated to their design and production, and due to the absence of materials having all the required properties. Ideally, these materials should have improved optical properties such as high transparency or large refractive indexes, which allow reducing the propagation losses and leads to strong light confinement during propagation.[1]

In particular, nonlinear optical properties have arisen as a significant challenge during the research for suitable materials, since active devices for the all-optical processing of signals based on nonlinear optical effects have been theoretically and experimentally proposed.[4, 7, 11] At the relatively low light intensities that normally occur in nature, optical properties of materials are independent of the intensity of illumination. These correspond to the optical response of matter that is familiar to us through our visual sense. On the contrary, if the illumination is made sufficiently intense, the optical properties of a medium begin to depend on the intensity of the light.[7] For example, the refractive index of a transparent medium is modified when a light beam with a high enough intensity travels through the medium (optical Kerr effect).[12]

Historically, nonlinear effects were considered not desirable, since intense beams propagating in a material could damage it through nonlinear effects. In this sense, early studies of optically induced changes of refractive index were mostly aimed at finding glasses with small nonlinearities, in order to avoid self-focusing in high power optical components or laser crystals.[11, 13] However, a great research effort has been directed since the mid-80s towards materials with the largest possible nonlinearities for their application in all-optical devices. For example, all-optical switches, in which an optical signal controls a gate that switches a second optical signal, have been proven possible in different interferometers (Sagnac, Mach-Zehnder, Michelson,...) with a nonlinear media in one of their arms.[7, 11] This is illustrated in Figure 1.2, where examples of three different nonlinear optical devices are shown. These devices allow selecting input signals depending on their intensities using an asymmetric Mach-Zehnder interferometer (Fig 1.2a), pulse selection in a directional coupler (Fig. 1.2b), or switch an incident signal by means of the optical bistability in a Fabry-Pérot interferometer (Fig. 1.2c).

Many materials have been studied as possible candidates for nonlinear optical devices. Ideally, these materials should have a high transparency in the wavelength range of interest, high nonlinear refractive index, short response time, as well as good mechanical and thermal properties. In order to define an objective parameter for the evaluation of the suitability of materials for nonlinear devices, several figures-of-merit have been proposed.[14] For instance, Jha *et al.* defined the figure-of-merit, F, as $F = \frac{n_2}{\tau\alpha}$,[15] where n_2 is the nonlinear refractive index, τ is the response time of the nonlinear process, and α is the absorption coefficient. According to that relation, materials such as metal-doped systems or semiconduc-

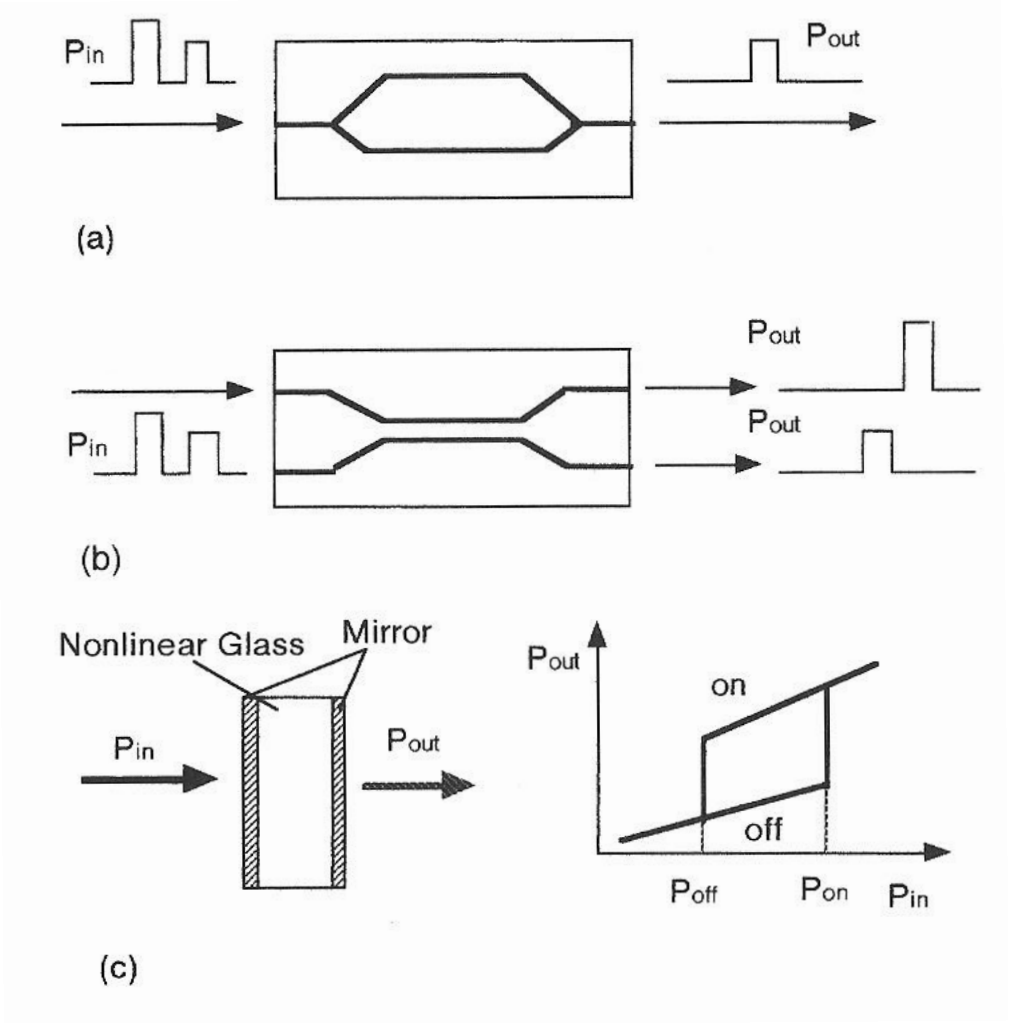

Figure 1.2: Nonlinear optical devices and their response to optical power: (a) Mach-Zehnder interferometer, (b) nonlinear directional coupler, and (c) Fabry-Pérot interferometer. Figure taken from ref. [11].

tors that show large n_2 would be promising candidates. However, they also show long τ and high absorption,[12, 16] which reduces their F. Other materials such as organic materials, which have a large F, show instead poor mechanical and thermal properties.[17] Finally, glass has proven to be one of the most promising materials due to its high intrinsic transparency (low α) and fast response times ($\sim$ fs – ps)[18] in spite of showing lower nonlinear optical responses than other materials. Moreover, glass shows a good mechanical and chemical durability and it can be produced with a high homogeneity, avoiding scattering losses or refrac-

tive index gradients. Actually, glass is the most important material in the field of optics, since most optical components are manufactured from glass [19] and it has already played an important role in the development of optical telecommunication networks, since SiO_2-based glasses are the basic materials for the fabrication of optical fibers.[4]

Glasses can be produced in multiple compositions that are very different from those of traditional SiO_2-based glasses.[11] Through tailoring the glass composition is possible to enhance different glass properties, like transparency range, nonlinear response, photoluminescent response,... when compared to SiO_2-based glasses. For example, regarding the nonlinear optical properties, chalcogenide glasses, such as GeS_3, As_2S_3, or As_2Se_3, show very high nonlinear refractive indexes, 100 or 1000 times higher than that of SiO_2.[11, 16] However, these glasses also show low gap energies and large density of defects, which increase their absorption and reduce their figure-of-merit.[18] Among oxide glasses, which have very low absorption at telecommunication wavelengths, the largest nonlinear responses have been shown by glasses containing heavy metal (HM) oxides or transition metal (TM) oxides.[18] In the present thesis, the optical properties of two different oxide glass systems have been studied: tellurite and germanate glasses, in which the network formers are TeO_2 (TeO_2-based glasses) or GeO_2 (GeO_2-based glasses) respectively, both containing a high amount of HM and TM oxides (TiO_2, Nb_2O_5, La_2O_3 Ta_2O_5, WO_3, PbO, and Bi_2O_3). In particular, tellurite glasses are in their own right promising materials for the development of nonlinear devices,[20] since they have a wide transparency range in the visible and near-IR (0.4 – 6 μm), show high linear refractive indexes ($n > 2$),[11, 20, 21] and the largest nonlinear refractive index and third order optical susceptibility, $\chi^{(3)}$ ($n_2 \propto \mathrm{Re}\left[\chi^{(3)}\right]$) among oxide glasses, with values up to 100 times than that of SiO_2 [11, 18, 21] as shown in Figure 1.3, where the nonlinear optical susceptibility of binary glasses based on different oxides (B_2O_3, SiO_2, GeO_2, TiO_2, and TeO_2) is shown. Moreover, these glasses have large rare earth ions solubility ($\sim 10^4$ ppm) and low phonon energies (~ 800 cm^{-1}), which increases their photoluminescent response when doped with these ions, and makes them also promising matrices for the synthesis of optical amplifiers.[22, 23] Finally, TeO_2-based glasses have also good thermal properties for the fabrication of real devices since they have low melting temperatures (~ 700 – 800 °C) and good thermal stability.[20]

For these reasons, tellurite glasses have been thoroughly studied and the synthesis and the characterization of tellurite glasses in advanced configurations like

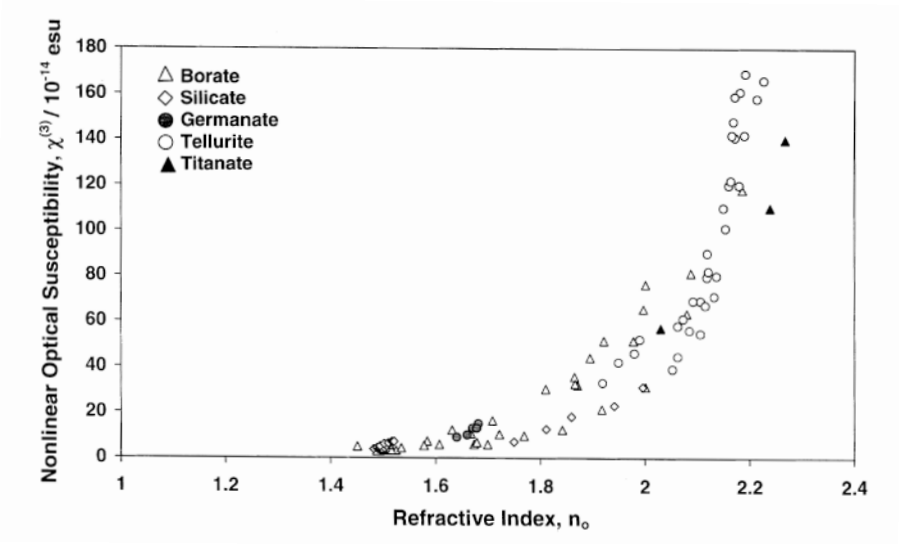

Figure 1.3: Nonlinear optical susceptibility, $\chi^{(3)}$, as a function of the refractive index, n_0, for different binary glasses. Figure taken from ref. [21].

fibers or films have been reported. In the case of fibers, there is much published evidence,[22, 23, 24, 25, 26] and, for example, Figure 1.4a shows a three core micron-size doped fiber.[27] Nowadays, commercial TeO_2-based glass fibers are already available,[28] as it is shown in Figure 1.4b. On the contrary, the production of high optical quality tellurite film glasses is still a challenge and there have been only a few attempts to produce them. During the 80s, tellurium suboxide (TeO_x) amorphous thin films were synthesized and characterized because of their possible application as optical memories for data storage.[29, 30] Later, TeO_2-based thin film glasses were studied due to their optical properties. In particular, transparent films with refractive indexes higher than 2 were produced,[31, 32] while the study of the photoluminescence response of Er-doped film glasses led to photoluminescent spectra similar to those of bulk glasses.[33, 34] Passive and active waveguides based on tellurite thin films with propagation losses lower than 1 dB cm^{-1} have been reported.[35, 36] Regarding the large nonlinear optical response of tellurite glasses, D´Amore *et al.* studied the dispersion of the linear and nonlinear refractive indexes of pure-TeO_2 glass films,[37] measuring an out-of-resonance $\chi^{(3)}$ value of 1.3×10^{-12} esu.

Different deposition techniques have been attempted to synthesize tellurite thin film glasses with good optical properties. They include chemical deposi-

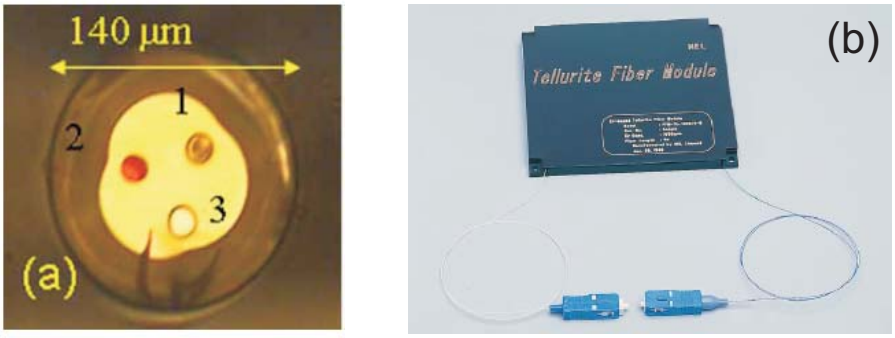

Figure 1.4: TeO_2-based glass fibers: (a) Three-core fiber with different core doping giving different color cores in transmission, taken from ref [27]. (b) Commercial Er-doped tellurite optical fiber amplifier fabricated by NTT Electronics.[28]

tion techniques such as sol-gel,[32, 38, 39, 40, 41] or physical deposition techniques, such as thermal evaporation,[31, 42] sputtering,[34, 35, 37] or pulsed laser deposition.[33, 36] In all cases, the stoichiometry, the structure, the presence of crystalline phases, or the density of the obtained films are major issues on the optical response, as it has proven to be strongly dependent on the deposition conditions used and on thermal annealing treatments.

In the present thesis, we have chosen the technique of Pulsed Laser Deposition (PLD) for the synthesis of multicomponent TeO_2-based thin film glasses. PLD is a simple and versatile deposition technique based on the use of a high-power pulsed laser to vaporize material from a target, which is then collected on a substrate to produced a thin film.[43] PLD is a very flexible technique since it can be carried out either in vacuum or in an inert or reactive environment. It is also possible to use several targets with different compositions in a single film growth process to lead to complex nanostructures. Moreover, PLD possesses several interesting characteristics for the production of functional optical thin films [44]: First, the laser ablated material has a very high kinetic energy (10 – 100 eV), which eases the formation of high density films with good adherence to the substrate. Second, PLD is in itself a pulsed process with a high instantaneous deposition rate ($\sim 10^4$ Å s^{-1}) that favors the formation of metastable phases. And finally, films with very complex compositions can be produced by PLD due to its stoichiometric character.[1] These properties of PLD, and in particular the

[1]The characteristics and advantages of PLD will be widely discussed in Chapter 2.

ability to produce metastable phases from targets with complex compositions, and the compatibility with an oxidizing enviorement, make this technique highly adequate for the deposition of multicomponent glasses. It was first applied for the deposition of vitreous materials by Vogel *et al.* for gallate, titanium-niobium silicate, and borosilicate glasses.[45] After that, it has been widely applied for the deposition of simple glasses such as silica,[46] chalcogenide glasses,[47] or complex oxide glasses such as phosphate,[48] lead-niobium germanate,[49] or tellurite glasses.[33, 36] These works prove that transparent film glasses with good optical properties can be synthesized by PLD when the deposition conditions are adequate. However, PLD has some drawbacks like the surface roughness that is related to the appearance of particulates or molten droplets on the film surface, or compositional deviations from the starting bulk material. As in the case of the optical properties, these drawbacks can be avoided by carefully choosing the experimental deposition conditions, such as the laser wavelength, the laser energy density on the target surface, or the gas background pressure.[43]

In particular, previous works have shown the influence of the experimental parameters in the deposition tellurite and heavy metal oxide glasses by PLD. In the case of tellurite glasses, Caricato *et al.* have found that the propagation losses in planar waveguides depend on the oxygen pressure used.[36] In the case of lead-germanate glasses, the laser energy density and the oxygen pressure strongly affect the optical properties of glasses.[50, 51] Therefore, PLD is a promising technique for the synthesis of TeO_2-based film glasses, but it is necessary to determine the optimum deposition conditions and to understand the relation between those experimental parameters and the optical properties of the film.

1.1 Aim of the thesis

This thesis aims at designing advanced TeO_2-based glasses in thin film configuration with optimized optical properties for photonic applications. Since the optical properties of glasses are strongly related to their composition and structure, the achievement of such a goal requires the optimization of the deposition process, the study of the glass network structure, and the characterization and optimization of the linear and nonlinear optical properties of TeO_2-based glasses. The latter implies understanding the influence of glass composition and structure on the nonlinear response to tailor the glass composition in order to obtain the highest possible nonlinear optical response.

1.2 Methodology and structure

The Laser Processing Group (LPG) of Instituto de Óptica (CSIC) has a wide experience in both the fundamental and applied aspects of PLD, and in particular in the application of PLD for the deposition of optical materials.[52, 53, 54, 55, 56, 57] In fact, the group has successfully applied the technique to the deposition of thin films of different glass systems.[48, 50, 58] The know-how acquired there serves as the starting point for the present thesis.

The first step of this work has been the synthesis of TeO_2-based bulk glasses and their characterization by Raman spectroscopy to determine the fundamental structural units and the role that different oxides play in the glass network. This study is the basis for the description of the structural properties of tellurite film glasses deposited by PLD and their relation with their linear and nonlinear optical response. Three tellurite glass systems containing TM and HM oxides have been selected: TeO_2–TiO_2–Nb_2O_5, TeO_2–WO_3–R_xO_y (with R_xO_y = TiO_2, Nb_2O_5, Ta_2O_5, WO_3, La_2O_3, Bi_2O_3, and PbO), and TeO_2–WO_3–PbO, as these oxides are know to enhance the optical response of glasses.[18]

The experimental deposition parameters of PLD are known to have a strong effect on the composition and optical properties of the deposited films. Therefore, we have initially performed a systematic study of the relation between deposition parameters and the composition, structure, and optical properties of TeO_2-based thin film glasses. The obtained results are discussed in terms of the plasma expansion dynamics and the deposition mechanisms in PLD, allowing us to determine the optimum deposition conditions.

Subsequently, we have deposited films in a wide range of compositions using the optimum experimental conditions. The linear and nonlinear optical properties of these films have been determined and compared to those of bulk glasses. The differences between the optical response of film and bulk glasses have been discussed in terms of the compositional and structural changes induced in the films during the deposition process.

Finally, the knowledge developed in the structural characterization and compositional analysis of TeO_2-based film glasses has helped us to explain the linear and nonlinear optical response of film glasses belonging to the Nb_2O_5–PbO–GeO_2 glass systems.

The work developed in this thesis has been structured in six chapters:

- Chapter 1 corresponds to the present introduction, where the motivation, the aim, the methodology and the structure of the thesis are described.

- Chapter 2 describes the experimental techniques used for the synthesis of bulk and film glass samples and the characterization of their composition, structure and optical properties.

- Chapter 3 focuses on the characterization of the structure and linear optical properties of bulk glasses.

- Chapter 4 is dedicated to determine the optimum deposition conditions for the synthesis of TeO_2-based thin film glasses by PLD by means of the characterization of their composition, structure, and linear optical properties.

- Chapter 5 describes the nonlinear optical properties of multicomponent bulk and film glasses. The differences between film and bulk samples are discussed in terms of their structural and compositional characterization.

- Chapter 6 summarizes the main conclusions of the thesis.

Chapter 2

Experimental techniques

This chapter aims at describing the experimental techniques used for the synthesis and characterization of multicomponent tellurite glasses both in bulk and film configurations. In the first case, bulk glasses have been prepared by mixing and melting powder oxides. The composition of these glasses has been designed in order to improve their optical response. Those glasses with the most promising properties have been selected for their production in thin film configuration by pulsed laser deposition.

The composition, structure and optical properties of both bulk and film glasses have been characterized using different methods. Ion beam analysis techniques and X-ray photoelectron spectroscopy provide information about the glass composition and chemical state of the atoms in the samples while Raman spectroscopy has been used to identify the structural units that form the vitreous network of the samples. Finally, the optical properties of bulk and film glasses have been analyzed. In particular, the linear optical response has been characterized by determining their complex refractive index and transmission, while the nonlinear optical characterization has been based on the determination of the third order optical susceptibility.

2.1 Glass preparation

2.1.1 Bulk tellurite glasses

Bulk tellurite glasses have been prepared using the standard melting technique [59] from commercial high-purity, at least 99.99% in weight, powder reagents. These reagents were mechanically mixed using a ball mill. Thereafter, they were heated for 45 minutes in a gold or platinum crucible placed in an electrical vertical furnace at a temperature between 700 to 750 °C, depending on their compositions. Once the powder mixture had melt, this was homogenized using an electrical platinum stirrer. The melt was then poured on a preheated brass mould with the desired shape. The glass sample was immediately introduced into an annealing furnace to avoid thermal stress that could break it. The sample was kept in the annealing furnace for 15 min at temperatures ranging from 350 to 450 °C and then cooled down to room temperature at a controlled rate of 3 °C min^{-1}.

2.1.2 Thin film glasses by pulsed laser deposition

Pulsed Laser Deposition (PLD) is a thin film deposition technique based on the interaction between a high-power pulsed laser beam and a target of the material we want to deposit in thin film configuration. The laser beam is focused on the target surface and, if the energy density is higher than an energy threshold, the material is ablated from the target surface.[60, 61] The vaporized material forms a plasma which expands perpendicularly to the target surface. This plasma is constituted by a mixture of energetic species including atoms, electrons, ions, and in some cases molecules, clusters of atoms, micron-sized solid particulates, or molten globules.[62] If a substrate is placed in the path of the expanding plasma, it is possible to collect a fraction of the ablated material, which leads to the growth of a thin film. All the process (laser ablation, generation and expansion of the plasma, and film deposition) occurs inside a vacuum chamber with a controlled atmosphere, as one of the characteristics of PLD is to be compatible with reduced atmospheres (up to hundreds of Pa) of either inert or reactive gases.[43]

The plasma is characterized by the presence of a significant fraction of species with a high kinetic energy (10 – 100 eV), which is one order of magnitude higher than in the case of ion-beam techniques, like sputtering (5 – 10 eV), and some orders of magnitude higher than that of other traditional deposition techniques like chemical vapor deposition or thermal evaporation ($\sim$ 0.1 eV).[44, 63, 64] Such

high energies improve the adherence of the material to the substrate and lead to denser films,[65] but it can also produce re-sputtering of a fraction of the deposited material.[66, 67] The average deposition rate of PLD is 10 Å s^{-1}, which is a similar rate than other deposition techniques.[64] However, the pulsed character of the process implies that a high amount of material is ejected in a short period of time. In fact, the process of ablation, generation, and expansion of the plasma takes place in tens of microseconds, leading to an instantaneous material flux of the order of 10^4 Å s^{-1}.[64] Therefore, film nucleation and growth is determined by the high material flux, which implies a large instantaneous deposition rate with a high energy transfer rate from the species present in the plasma to the substrate.[43] This favors the deposition of films far from the thermal equilibrium and may lead to the formation of metastable phases.[63, 68]

Another of the advantages of PLD is its stoichiometric character. This has to be understood as the ability to transfer the composition of the target to the deposited film, provided that the adequate experimental conditions are used.[69, 70] The reason for this is that once the laser pulse hits the target, the heating rate of the irradiated target, related to the ablation process,[71] is so fast that material removal occurs before the individual components can segregate and thus the vaporization is congruent.[60] Moreover, the presence of an atmosphere allows controling the kinetic energy of the species in the plasma [43, 61] and, in the case of a reactive gas, allows establishing chemical reactions between the ablated material and the gas atoms or molecules.[60, 69] These properties of PLD, together to the fact that PLD allows the production of metastable material phases, make PLD highly adequate for the production of thin film oxide glasses with complex compositions.[43, 68]

Although the physical and chemical process involved in laser ablation, generation, and expansion of the plasma are quite complex[1], the experimental setup for PLD is relatively simple. Figure 2.1 shows a scheme of the setup used in the present work. The laser source was an ArF excimer laser (λ = 193 nm) with a pulse duration τ = 20 ns (full width at half maximum). The energy and the repetition rate of the laser was adjusted in function of the deposited material, in order to control the total amount of power used to ablate the target. The laser beam was focused using a fused silica lens onto the surface of the target placed inside the vacuum chamber. The angle of incidence was 45° and the spot

[1]The study of these processes are not the subject of this thesis. Extensive literature on the fundamental processes involved in PLD can be found in refs. [43, 60, 61, 44, 63, 68, 70, 72]

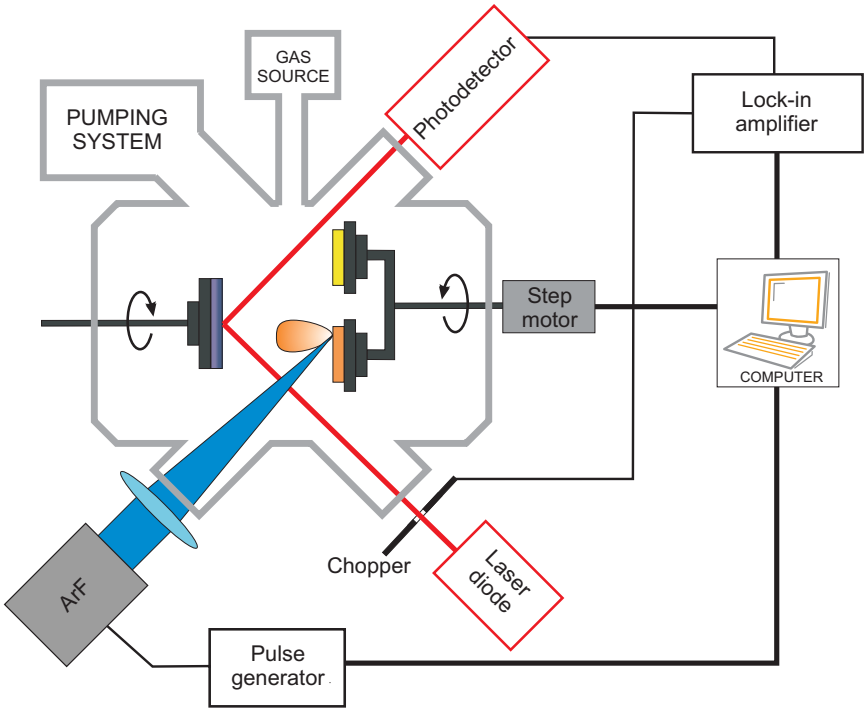

Figure 2.1: Scheme of the experimental setup used for pulsed laser deposition

size on the target surface was approximately 1.5 – 1.8 mm^2. The substrate was placed parallel to and in front of the target at a distance of 3 – 4 cm. The target and the substrate were rotated during all the deposition process. This allowed avoiding the accumulative damage on the surface of the target while in the latter case allowed us to homogenize the distribution of material deposited on the substrate. The deposition took place at room temperature in a controlled oxygen atmosphere. The vacuum chamber was evacuated to a residual pressure of 7 $\times$ 10^{-4} Pa and then filled with oxygen up to a dynamic pressure in the range of 1 – 10 Pa.

In all cases, the deposition process was monitored by in-situ reflectometry using a laser diode ($\lambda = 670$ nm) as shown in Fig. 2.1. The diode was focussed onto the maximum of the deposit at an angle of 45°. The reflection of the diode was detected using a Si detector and a lock-in amplifier. Due to the interference between the beams reflected on the air-film and film-substrate interfaces, the measured intensity is a periodic signal whose amplitude and period are related to the film thickness and to the optical properties of both film and substrate.[73] Therefore, the in-situ measurement of reflectivity allows controlling the film thickness and

checking if the sample has the expected optical properties, *i.e.* if the sample is transparent. Figure 2.2 shows the evolution of the reflectivity during the deposition of a slightly absorbent tellurite film glass with a thickness of approximately 200 nm on a Si substrate. The experimental reflectivity has been fitted using the Fresnel reflection coefficients for different film thickness. This informs us about the total film thickness and the linear refractive index at the diode wavelength and thus, the deposition rate and the linear optical response of the film can be quantitatively evaluated.

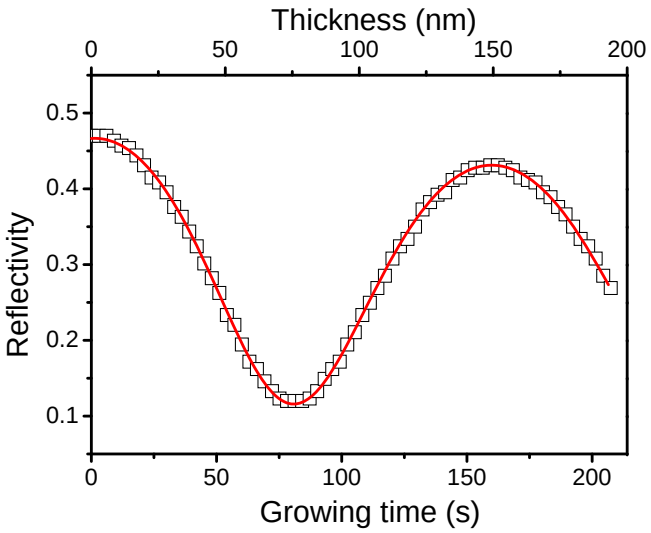

Figure 2.2: (□) In-situ temporal evolution of the reflectivity during the deposition process. The experimental values have been compared to (red line) the theoretical reflectivity of a film with refractive index $\hat{n} = 2.4 + 0.07i$ calculated for different film thickness according to Fresnel reflection coefficients.

Finally, films have been deposited on two different substrates suited to the different structural and optical characterization techniques considered:

- Crystalline Si wafers for compositional analysis and linear optical characterization.

- Borosilicate glasses with a thickness of 1 mm or 0.1 mm to measure the transmission and the nonlinear optical properties of the deposited glasses, respectively.

2.2 Compositional and structural analysis

2.2.1 Ion beam techniques

The atomic composition of the films was determined using Rutherford Backscattering Spectrometry (RBS), Nuclear Reaction Analysis (NRA), and Particle-Induced X-ray Emission (PIXE). These techniques are based on different physical processes induced in a sample by bombarding it with high-energy ions. RBS analyzes the fraction of backscattered ions by the material, which depends on the concentration and nature of the atoms in the sample. RBS is sensitive to heavy elements, while for the analysis of light elements such as oxygen other techniques such as NRA are required. This technique is based on the study of the nuclear reactions induced by the incident ion beam. Finally, in the case of films with heavy elements with similar masses, RBS is not accurate enough to distinguish among them and thus, RBS is performed simultaneously with PIXE. This technique is based on the detection of X-ray photons excited by the incident ion beam, whose energies are characteristic of each element.

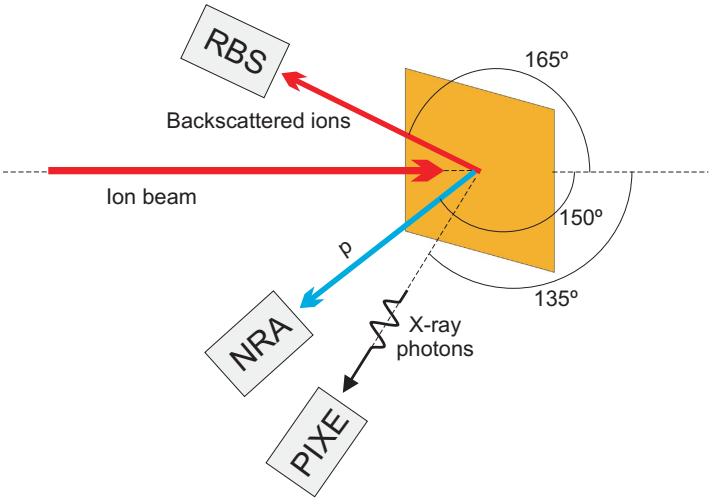

Figure 2.3: Scheme of the geometry used in the ion beam analysis experiments.

Figure 2.3 shows a scheme of the experimental geometry used. The diameter of the incident ion beam is 1-3 mm and the nature and energy of the incident ions depend on each particular technique. In the case of RBS, the ion beam consisted of $^{4}He^{++}$ ions with an energy of 1.98 MeV, while the backscattered ions were detected using a detector placed at 165°. The measured spectra were simulated

with the SIMNRA code.[74] In the case of NRA, the analyzed nuclear reaction was $^{16}O(d,p)^{17}O$ at 878 KeV, in which ^{16}O and deuteron react to form ^{17}O with the emission of a proton. The signal was detected using a detector placed at 150° and the absolute oxygen content was determined within 10% using a Ta_2O_5/Ta reference, which has 697.7±3 % × 10^{15} ^{16}O atoms cm^{-2}. Finally, the beam used for the simultaneous measurement of RBS and PIXE consisted of protons at 2.96 MeV or $^4He^{++}$ at 4 Mev. In this case, the X-ray signal was detected with a Li-doped Si detector placed at 135° and the PIXE spectra were simulated with the GUPIXWIN software.[75]

Ion beam analysis experiments were performed in Centro Nacional de Aceleradores (Sevilla), with the collaboration of Dr. J. Garcia-Lopez and Dr. I. Ortega. Figure 2.4 shows representative RBS and PIXE spectra corresponding to tellurite thin film glasses using (a) RBS and (b) PIXE.

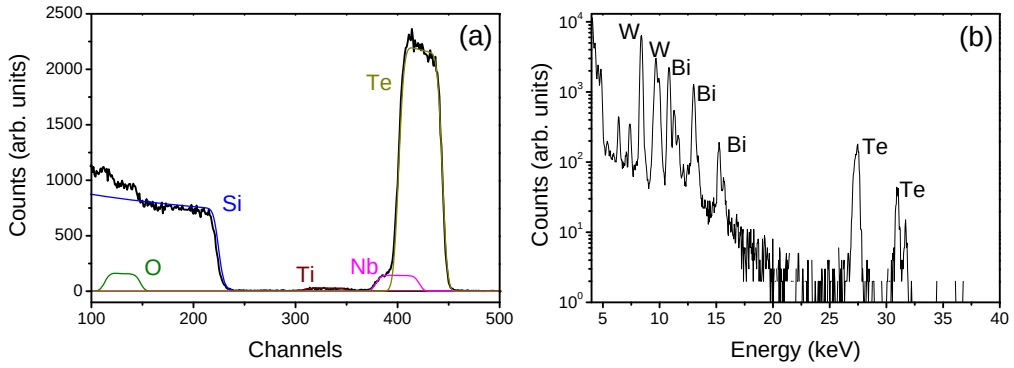

Figure 2.4: (a) Rutherford backscattering spectrum of a $90TeO_2 \cdot 5TiO_2 \cdot 5Nb_2O_5$ thin film glass deposited on a Si substrate. The content of the different atoms present in the sample (Te, Nb, Ti, O, and Si) has been obtained by fitting the spectrum using the SIMNRA code (color lines). (b) PIXE spectrum of a $80TeO_2 \cdot 15WO_3 \cdot 5Bi_2O_3$ film glass. The spectrum peaks have been assigned to the X-ray emitted by Te, Bi, and W atoms.

2.2.2 X-ray photoelectron spectroscopy

X-Ray Photoelectron Spectroscopy (XPS) has been used to analyze the atomic concentration and chemical state of bulk and film glasses. Samples are irradiated with X-ray photons, which leads to the photoemission of electrons from the atomic core levels or from the valence bands of the atoms present in the solid. The kinetic

energy of these photoelectrons depends on the incident X-ray photon energy and on the binding energy (BE) of the photoemitted electron in the atom.[76] Since BEs are characteristic of each element, the technique allows the identification and quantification of the elements present in the sample. Moreover, BE may show small changes in its value that are result of the chemical environment of the emitting atom and thus XPS also gives information about the chemical state and bonding of atoms in the sample.

The experimental setup used consists of a Mg Kα ($\hbar\omega$ = 1253.6 eV) X-ray source (12 kV and 10 mA) and a spectrometer equipped with a hemispherical electron analyzer. The base pressure of the analysis chamber was maintained below 3×10^{-7} Pa. Peak intensities were estimated by calculating the integral of each peak after smoothing and subtracting a Shirley-type background, in which every point of the background is proportional to the height of the peak.[77] Binding energies were referenced to the C 1s line at a BE of 284.9 eV. The absolute errors in the quantitative XPS compositional measurements were estimated to be 5% in the cases of major elements, while in the case of weaker XPS peaks, related to elements in a low concentration, the error was estimated to be 20%. XPS spectra of bulk and film glasses were recorded in collaboration with Prof. J. L. G. Fierro from Instituto de Catálisis y Petroleoquímica (CSIC, Madrid) to determine the atomic oxidation state and composition of the samples. The spectra of the original powder reagents were also measured in order to have reference values of the BE of the molecules present in the films glasses. As an example, Figure 2.5 shows the XPS spectra of some cations present in the powder reagents.

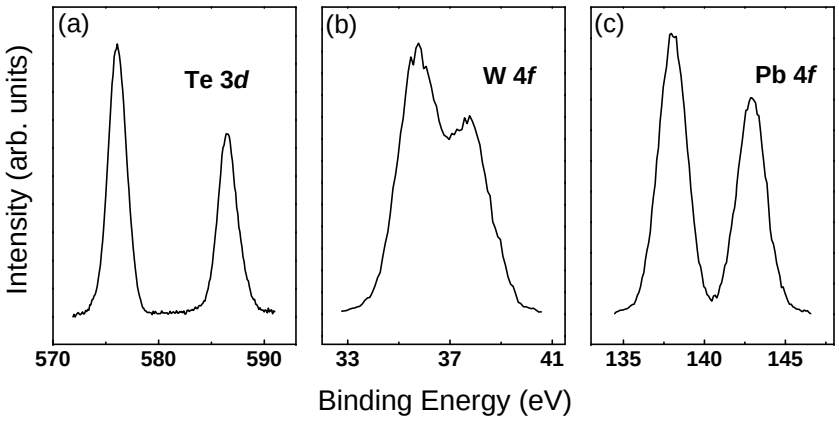

Figure 2.5: XPS spectra of the core electrons of (a) Te in TeO_2, (b) W in WO_3 and (c) Pb in PbO.

2.2.3 Raman spectroscopy

The structure of the glass network of tellurite glasses has been studied using Raman spectroscopy. This is based on the study of the light scattered by a sample due to the Raman effect. When a light wave interacts with a molecule, it can be either absorbed or scattered.[78] In the first case, the energy of the photon matches the difference between two energy levels of the molecule and therefore the light is absorbed, and the molecule is promoted to an excited state. In the second case, the light wave distorts the electron cloud around the nuclei, resulting in a high energy short-lived state, called virtual state, which does not correspond to any energy level of the molecule, and then light is immediately re-emitted. If the scattering process is elastic and the energy of the incident and the emitted photon are the same, it is the usual Rayleigh scattering, which is the most intense form of scattered radiation and it occurs when the electron cloud relaxes with any nuclear movement.[78]

However, the interaction light-molecule may be accompanied by a change in the motion of the nuclei. The intensity of the scattered radiation in this case, known as Raman scattering, is much less intense than in the case of Rayleigh scattering [78] as only one in 10^6 – 10^8 scattered photons is Raman scattered. Raman scattering is an inelastic process in which the energy of the emitted radiation is different from that of the incident radiation. This energy can be lower or higher depending on the starting energy of the molecule. If the molecule is in the ground state, the energy of the Raman scattered photon will be lower than that of the incident photon (Stokes scattering), while if the molecule is in an excited vibrational state, the Raman scattered photon will have a higher energy (anti-Stokes scattering). The relative intensities of Stokes and anti-Stokes scattering are related to the thermal population of molecules in the different vibrational levels and thus, the intensity of Stokes scattering is much higher than that of anti-Stokes scattering. Figure 2.6 show an energy-level diagram in which the different processes of absorption and Rayleigh and Raman scattering are shown.

Since the energy of Raman scattered photons is related to the energy of vibrational states of matter, Raman spectroscopy is widely used for the characterization of these vibrational states, which provides important information on the chemical structure and physical forms of molecules and structural units of solids, liquids or gases. This technique is also useful for the semi-quantitative determination of the amount of a substance in a sample.[78, 79] In Raman spectroscopy, the sample is irradiated with a monochromatic pumping beam and the

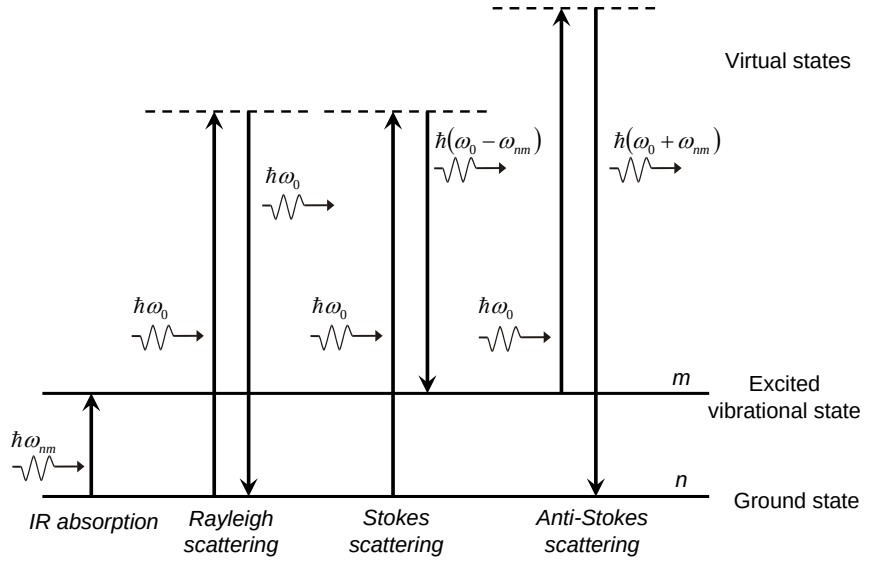

Figure 2.6: Diagram of IR absorption, Rayleigth scattering and Raman scattering processes.

intensity of the scattered radiation is registered using a monochromator and a detector. The measured intensity is often represented as a function of the the energy difference (Raman shift) between the pumping and the scattered beams.

From Fig. 2.6 it could be thought that the structural information given by IR absorption and Raman scattering is the same, since we are measuring the difference of energy between two vibrational levels in both cases. However, there are several important differences that have to be taken into account:

- IR absorption is a resonant process while Raman effect is a non resonant scattering process.[80]

- In the case of IR absorption, it is necessary to pump in a broad range of wavelengths and the measured spectrum consists of the intensity loss at certain energies, while in the case of Raman spectroscopy the sample is pumped with a monochromatic radiation and the scattered light is registered in a wide range of wavelengths .[79]

- The most important difference lies in the fact that not all the transitions are simultaneously Raman and IR active, since the selection rules for Raman effect and IR absorption are different. The Raman effect is related to a

change in the polarization of the electron cloud around the molecule, while the IR active vibrations are those which imply a change in the dipolar moment of the molecule.[78]

In this work two different experimental setups were used. In the first case, spectra were obtained using a confocal Raman microscope equipped with an Ar laser emitting at 514.5 nm having an output laser power of 150 mW. In the second case, the experimental setup consisted of a confocal Raman microscope too, but equipped with a diode laser emitting at 785 nm having an output laser power of 30 mW. In both cases, the laser beam was focused on the sample using a 50X objective. The elastic scattering was eliminated using a notch filter and the signal was detected through an electrically refrigerated CCD camera. The contribution to the spectra from the substrate was carefully subtracted in the case of film glasses. Raman spectra were recorded in collaboration with Prof. C. Domingo and Prof J. V. García Ramos from Instituto de Estructura de la Materia (CSIC, Madrid) and Prof. A. Jha and Dr. S. Shen from Institute of Materials Research (University of Leeds, United Kingdom).

The Raman spectra of glass samples were corrected using the so-called reduced spectrum correction [81]:

$$I_{red}(\Omega) \propto I_{exp}(\Omega)\frac{\Omega}{n(\Omega)+1}\frac{1}{(\omega_L-\Omega)^4} \tag{2.1}$$

where I_{red} and I_{exp} are respectively the reduced and the experimental Raman intensities, Ω is the Raman frequency shift, ω_L is the frequency of the pumping laser and $n(\Omega) = [\exp(\hbar\Omega/k_BT) - 1]^{-1}$ is the Bose distribution function for phonons at Stokes frequency. This correction is necessary to avoid spurious effects in the intensity of the peaks in the low-frequency part of the spectrum due to the scattering by thermally-excited low-energy phonons, represented by the Bose factor $n(\Omega) + 1$, and to the Rayleigh scattering, represented by the factor $(\omega_L - \Omega)^{-4}$.[81, 82] The reduced spectra were also normalized to the maximum of intensity to ease the comparison.

Figure 2.7 shows an example of a Raman spectrum obtained from a tellurite bulk glass once it has been corrected and normalized. Three main bands can be seen in that spectrum at 400 – 550 cm^{-1}, 600 – 700 cm^{-1} and 700 – 850 cm^{-1}. These bands correspond to modes of vibration of Te-O bonds in the different structural units that comprise the vitreous structural network of TeO_2 glass, as it will be shown in Chapter 3. Therefore, the band position and intensity in

the Raman spectrum provide information about the presence, type and relative amount of structural units in the glass network.

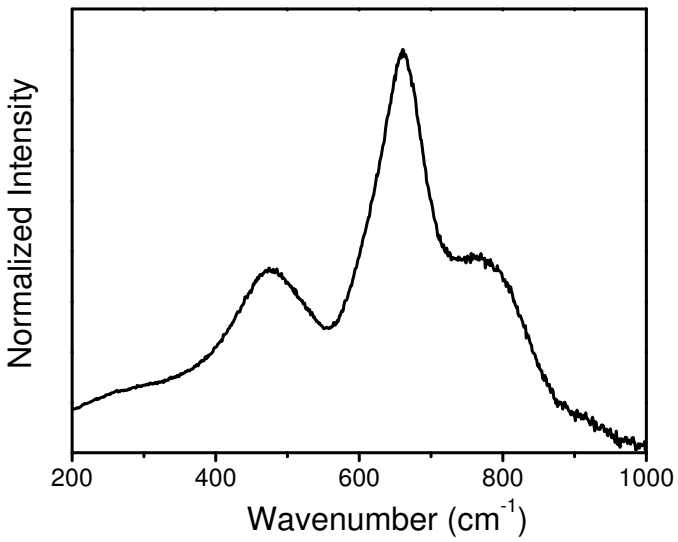

Figure 2.7: Reduced Raman spectrum of a $90TeO_2 \cdot 5TiO_2 \cdot 5Nb_2O_5$ bulk glass.

2.3 Optical properties

The interaction between light and matter can be described in terms of the dipole moment per unit volume or polarization ($\vec{P}(\omega)$) induced in the material by the electromagnetic field of the light wave.[73] $\vec{P}(\omega)$ can be then expressed as a power series of the electrical field ($\vec{E}(\omega)$) [83]:

$$\begin{aligned} \vec{P}(\omega) &= \chi^{(0)} + \chi^{(1)}(\omega)\vec{E}(\omega) + \chi^{(2)}(\omega)\vec{E}(\omega)\vec{E}(\omega) + \\ &\quad + \chi^{(3)}(\omega)\vec{E}(\omega)\vec{E}(\omega)\vec{E}(\omega) + \cdots \end{aligned} \tag{2.2}$$

where $\chi^{(n)}$ is a tensor of n+1 rank that describes the n^{th} order susceptibility of the material. $\chi^{(0)}$ is not null only in materials that show spontaneous polarization in absence of an external field, such as ferroelectrics. $\chi^{(1)}$ is related to the linear complex refractive index $\hat{n}$, while $\chi^{(2)}$ and $\chi^{(3)}$ describe second and third optical nonlinear effects in the material. The observation of higher order effects involves field intensities far beyond the ones used in the present thesis, and thus these effects will be not considered. In the case of centrosimmetric materials, such as

glasses, the second order term, $\chi^{(2)}$, is zero, and thus the first nonlinear term is $\chi^{(3)}$. Therefore, the optical properties of tellurite glasses can be characterized in terms of their linear optical response, related to $\chi^{(1)}$, and their nonlinear optical response, related to $\chi^{(3)}$:

$$\vec{P}(\omega) = \chi^{(1)}(\omega)\vec{E}(\omega) + \chi^{(3)}(\omega)\vec{E}(\omega)\vec{E}(\omega)\vec{E}(\omega) \tag{2.3}$$

In general, $\chi^{(1)}$ and $\chi^{(3)}$ are complex tensors. In the case of first order susceptibility, the real and imaginary parts of $\chi^{(1)}$ are directly related to the real and imaginary parts of the linear complex refractive index [73]:

$$\hat{n} = \sqrt{1 + \chi^{(1)}} = n + i\kappa \tag{2.4}$$

where n is the refractive index and κ is related to the absorption coefficient α:

$$\alpha = \frac{4\pi\kappa}{\lambda} \tag{2.5}$$

The nonlinear optical effects due to $\chi^{(3)}$ lead to a variation of the refractive index and the absorption coefficient. In the case of a nonabsorbing media, with a very small linear absorption coefficient, the variation of n and α depend linearly on the intensity of the electrical field:

$$n = n_0 + n_2 I \qquad \alpha = \alpha_0 + \beta I \tag{2.6}$$

where n_2 is the nonlinear Kerr refractive index and β is the nonlinear absorption coefficient. Both n_2 and β are directly related to the real and imaginary part of $\chi^{(3)}$ respectively in a nonabsorbing media [12]:

$$n_2 = \frac{3}{4{n_0}^2\epsilon_0 c}\mathrm{Re}(\chi^{(3)}) \qquad \beta = \frac{3\pi}{{n_0}^2\epsilon_0 c\lambda}\mathrm{Im}(\chi^{(3)}) \tag{2.7}$$

while the relation in the case of an absorbing media is more complex.[84]

In the next sections, the experimental techniques used for the characterization of the linear and nonlinear optical properties of bulk and film glasses are described.

2.3.1 Linear optical properties

The linear optical response of film and bulk glasses was characterized through their linear complex refractive index and their transparency range. The dispersion of the real ($n(\lambda)$) and imaginary ($\kappa(\lambda)$) parts of the refractive index were measured using spectroscopic ellipsometry while the transparency of the samples was determined from transmission measurements.

Spectroscopic ellipsometry

Ellipsometry is based on the change of the light polarization that occurs when a beam of polarized light is reflected by the interface of two materials.[85] This change is related to the optical properties and the structure of the media forming the interface. In fact, ellipsometry actually measures the ratio between the complex Fresnel reflection coefficients for the p- and s-polarization components of the beam [86]:

$$\rho = \frac{R_p}{R_s} \tag{2.8}$$

The ellipsometric parameter ρ is a complex number that can be expressed in terms of two real parameters, Ψ and Δ, as:

$$\rho = \tan\Psi e^{i\Delta} \tag{2.9}$$

where $\tan\Psi$ gives the intensity ratio between the p- and s-components of the reflected beam, and Δ provides the difference between the phase shifts experienced upon reflection by the p- and s-polarization components of the beam.[85] Since R_p and R_s are functions of the incidence angle of the beam and the complex refractive indexes of the media forming the interface,[73] it is possible to obtain the optical properties of both media from the values of Ψ and Δ at different angles and wavelengths.

In the case of thin films the determination of the optical properties is more complex due to interference effects at the interfaces. This makes necessary a numerical analysis of the experimental data, based on mathematical models or tabulated data for the optical properties of the substrate and the different layers. In the present work, films were treated as single layers of glass, which were modeled using a Cauchy-type dispersion for the real part of $\hat{n}$ and an exponential

decay for the imaginary part:

$$n(\lambda) = A_n + \frac{B_n}{\lambda^2} + \frac{C_n}{\lambda^4} \tag{2.10}$$

$$\kappa(\lambda) = A_\kappa + \exp\left[B_\kappa\left(\frac{1}{\lambda} - \frac{1}{\gamma}\right)\right] \tag{2.11}$$

where A_n, B_n, C_n, A_κ, B_κ are adjustable parameters and γ is the optical gap of the material expressed in nanometers.

The experimental ellipsometric data were measured using a variable angle spectroscopic ellipsometer with a rotating analyzer. The setup consisted of a light source emitting unpolarized light in the range from 250 to 1700 nm. The incident beam, whose wavelength and polarization state was selected by a monochromator and a linear polarizer, was reflected on the surface of the sample. The intensities of the p- and s-components of the reflected beam were measured using a continuously rotating analyzer and a solid state photodetector. The system was mounted in a motorized goniometer, which allowed measuring at different angles. The fitting of the experimental data to the model described was made using the Marquardt-Levenberg iterative algorithm [86] to minimize the mean square error of the fitting.

Figure 2.8a shows the best fit of the experimental Ψ and Δ data obtained for a representative tellurite thin film glass. Figure 2.8b shows the values of

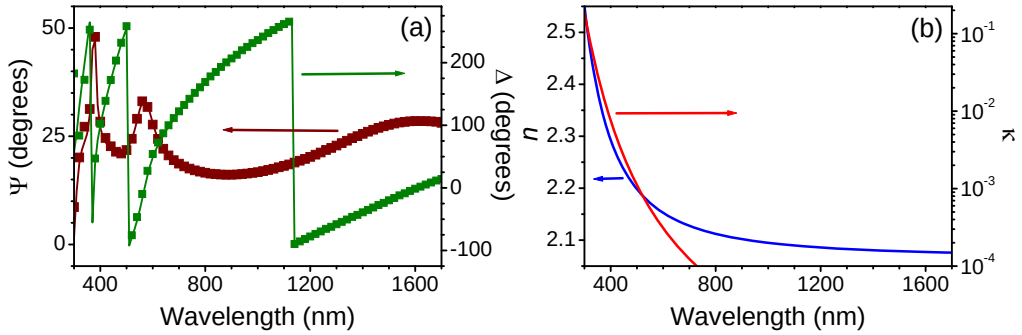

Figure 2.8: (a) Ellipsometric (■,■) experimental and (dark red line, dark green line) simulated Ψ and Δ data as a function of the wavelength, measured at an incidence angle of 65° in a TeO_2–TiO_2–Nb_2O_5 thin film glass deposited on a Si substrate. (b) (blue line) Real and (red line) imaginary parts of the linear refractive index deduced from the experimental data shown in (a).

n and κ deduced from that fit. The experimental error for n is in all cases $\pm$ 0.005, while in the case of κ is 1%. It is worth noting at this point that the accuracy in the determination of κ is lost for wavelengths in which the sample is transparent, since the experimental detection limit is 10^{-4}, which is several orders of magnitude higher than the typical κ value of transparent materials.

Optical transmission

The transparency range and the UV optical absorption edge of bulk and film glasses have been determined from their transmission spectra. These spectra were recorded at normal incidence using a comercial spectrophotometer. In these measurements, the fraction of light absorbed by the material was determined by comparing the intensity I_0 of an incident light beam to the intensity I detected after passing through a sample of known thickness L. The ratio between the two intensities is the transmission T. There are two sources for the reduction of the light intensity when the beam travels through the sample: the reflection of light at the interfaces air-sample and sample-air, and the intrinsic losses caused by absorption during propagation.[87] Therefore, the transmission can be expressed as:

$$T = \frac{I}{I_0} = (1 - R)^2 e^{-\alpha L} \tag{2.12}$$

where α is the absorption coefficient and R the Fresnel reflection coefficient at normal incidence in the interface air-sample. Besides the transmission T, the transparency of the samples can be expressed in terms of their optical density OD [87]:

$$OD = -\log_{10}(T) = -\log_{10}\left(\frac{I}{I_0}\right) \tag{2.13}$$

Figure 2.9 shows an example of T and OD measured in a $85TeO_2 \cdot 15WO_3$ bulk and a film glass.

The UV optical absorption edge is related to the light absorption caused by electronic transitions in the material. That edge was qualitatively estimated using the optical cutoff, *i.e* the wavelength at which the OD is 0.5.[88] Moreover, there are theoretical models that describe the different electronic mechanisms responsible for the absorption in the UV in amorphous materials. The structural disorder characteristic of amorphous solids modifies the band edges and thus, the UV optical absorption edge, with respect to crystalline systems. The main differences are the narrowing of the band gap and the formation of localized states

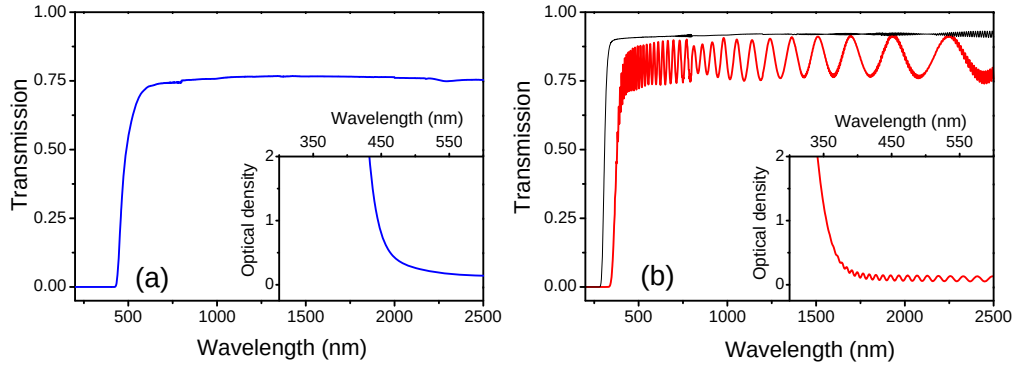

Figure 2.9: Transmission spectra of a $85TeO_2 \cdot 15WO_3$ (a) bulk and (b) film glasses. The insets show the optical density in the vicinity of the UV absorption edge. In the case of the film glass, the transmission spectrum of a (black line) borosilicate glass used as substrate is included.

within the band tails.[20, 89] According to these effects, two different regions can be distinguished in the absorption edge. At low absorption coefficients ($1 \lesssim \alpha \lesssim 10^4$ cm^{-1}), namely large wavelengths or small photon energies ($\hbar\omega$), α can be described by an exponential dependence on $\hbar\omega$ [90]:

$$\alpha(\hbar\omega) = B\exp\left(\frac{\hbar\omega}{E_U}\right) \tag{2.14}$$

where B is a constant and E_U is known as the Urbach energy. In that spectral range, known as Urbach region, the optical absorption is attributed to electronic transitions from the valence band to localized states in the band tail or from these localized states to the conduction band.[20, 89]

For higher photon energies and larger absorption coefficients ($\alpha \gtrsim 10^4$ cm^{-1}), transitions from the valence band to the conduction band may occur.[20, 89] In that region, known as the Tauc region, α values have been successfully described using the following relation[91, 92]:

$$\alpha(\hbar\omega) = C\frac{(\hbar\omega - E_g)^2}{\hbar\omega} \tag{2.15}$$

where C is a constant and E_g is the optical gap.[92]

In the present work, the maximum experimental resolution of the transmission measurements performed is 5×10^{-4}. Since the intrinsic transmission scales as

$e^{-\alpha L}$, the maximum measurable value for the absorption coefficient is limited by the thickness:

$$\alpha L \leq \ln\left(5 \times 10^{-4}\right) \tag{2.16}$$

In the case of bulk samples with thickness of the order of $\sim$ 1 mm, this value corresponds to $\alpha \lesssim 75$ cm^{-1}, while in the case of thin film glasses with thickness of the order of $\sim$ 1 μm, this is $\alpha \lesssim 7.5 \times 10^4$ cm^{-1}. This limiting values make necessary to use different expressions to describe the UV absorption edge of bulk and film samples. For the former, the Urbach relation has been use to fit the absorption coefficient, while in the case of films, α has been fitted using the Tauc relation. To illustrate this point, Figure 2.10 shows these fittings in a $85TeO_2 \cdot 15WO_3$ bulk and film glasses, whose transmission spectra have been shown in Fig. 2.9.

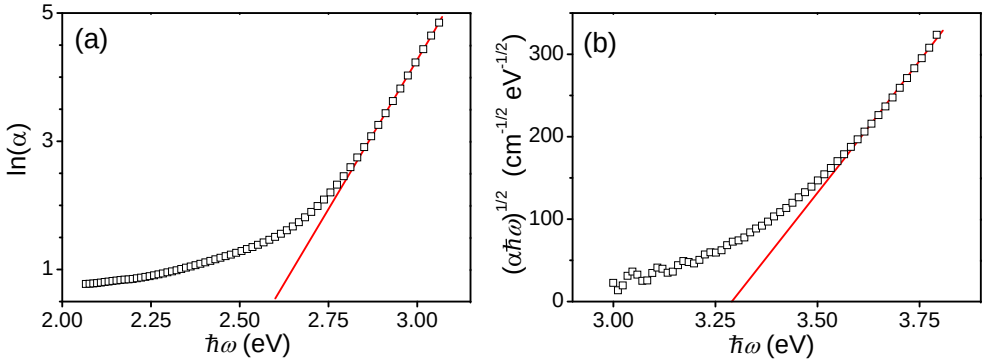

Figure 2.10: (a) Urbach and (b) Tauc plots for (a) a $85TeO_2 \cdot 15WO_3$ bulk glass and (b) a film deposited from this bulk glass. The (□) experimental values have been fitted to the Urbach and Tauc relations in the case of (a) bulk and (b) film glasses respectively.

2.3.2 Nonlinear optical properties

As it has been described above, the first nonlinear term of the optical susceptibility in the case of glasses is $\chi^{(3)}$. $\chi^{(3)}$ is a 4$^{\text{th}}$ rank tensor with 81 elements. In the case of isotropic materials, such glasses, only 21 of these elements are nonzero due to spatial symmetry considerations. Moreover, only 3 of the 21 nonzero elements are independent, and in the case of degenerate processes, *i.e.* when all the light waves involved have the same frequency, the number of independent elements is reduced to 2.[13, 83]

In the present thesis, we characterize the non-linear response of the studied glasses through the determination of the modulus of the diagonal element of the third order susceptibility tensor, as determined by Degenerate Four Wave Mixing (DFWM) measurements. This technique is based on a four-wave mixing process, in which a lossless nonlinear optical medium is illuminated by two strong pump waves and a probe wave, which generate a fourth conjugated beam. Intuitively, in the case of parallel polarizations, the four-wave mixing interaction can be seen as the effect of the interference of the two pump beams leading to a periodic field distribution. As a consequence of the refractive index dependence with the electric field intensity, this generates a refractive index grating that affects the probe beam, leading to the formation of the so-called conjugated beam.[83]

The experimental configuration used in the DFWM setup is the so-called "forward boxcar" configuration (Figure 2.11), in which three co-propagating and parallel beams are overlapped at the sample by means of a lens. If the three incident beams are in the vertices of a square centered in the lens axis, this configuration ensures the phase matching condition.[12] Usually, the beams placed in opposite vertices of the square are the pump beams, I_{p_1} and I_{p_2}, while the third beam is the probe beam, I_{pr}. The conjugated beam, I_c, generated by nonlinear interaction, is placed in the vertex opposite to I_{pr}.

In order to obtain the dependency of the conjugated beam intensity in terms of $\chi^{(3)}$, it is necessary to solve the nonlinear wave equation in which the third order polarization ($\vec{P}^{(3)}$) is the source of the electromagnetic field. If the variations of the electric field are small in the scale of the wavelength (slowly varying envelope approximation) and using the boundary conditions for the incident beams, it is

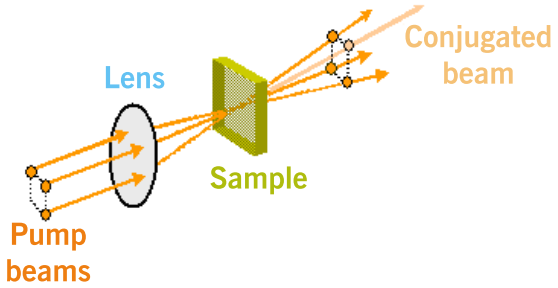

Figure 2.11: Forward boxcar configuration.

possible to calculate the intensity of the conjugated beam.[12] In the case of a centrosymmetric material with negligible linear absorption, incident beams with the same linear polarization and low conversion efficiency ($I_c \ll I_{p_1}, I_{p_2}, I_{pr}$), I_c can be expressed as function of the modulus of diagonal component of the tensor $\chi^{(3)}$:

$$I_c \cong \left(\frac{3\pi L}{\epsilon_0 n_0^2 c\lambda}\right) \left|\chi^{(3)}_{xxxx}\right| I_{p_1} I_{p_2} I_{pr} \tag{2.17}$$

where L is the overlapping length of the beams in the focus of the lens and n is the real part of the linear refractive index of the sample. For simplicity, we will refer to $\left|\chi^{(3)}_{xxxx}\right|$ from now on as $\chi^{(3)}$. If the three pump beams have the same intensity ($I_{p1} = I_{p2} = I_{pr} = I_0/3$) the intensity of the conjugated beam will follow a cubic dependence with the intensity of the pump beams ($I_c = bI_0^3$). The use of a reference material with negligible absorption and well known $\chi^{(3)}$ value, like SiO_2 ($\chi^{(3)}_{SiO_2} = 1.8 \pm 0.3 \times 10^{-14}$ esu),[12] allows simplifying the measure of $\chi^{(3)}$, since we can directly compare the conjugated signals of the sample and the reference.

$$\left|\chi^{(3)}_{(s)}\right| = \left(\frac{n_{(s)}}{n_{(r)}}\right)^2 \left(\frac{L_{(r)}}{L_{(s)}}\right) \left(\frac{b_{(s)}}{b_{(r)}}\right)^{1/2} \left|\chi^{(3)}_{(r)}\right| \tag{2.18}$$

where the subscripts (s) and (r) correspond to the sample and the reference respectively.

The DFWM experimental setup used in this work is shown schematically in Figure 2.12. The excitation laser beam is split in three parallel arms (1, 2, and 3 in the figure) having equal power, allowing separate control of the beam polarizations by means of half-wave plates. The relative delays of the pulses in each arm are controlled by two independent delay lines. The beams are overlapped at the sample by means of a 75 mm focal length lens leading to a beam waist of ~ 40 μm. The intensity I_c is measured using a solid state detector (InGaAs or Si depending on the beam wavelength) and the value of $\chi^{(3)}$ is finally determined using a fused silica plate as reference material. Two different optical excitation sources were used in order to measure $\chi^{(3)}$ at five different wavelengths (600, 800, 1200, 1300, and 1500 nm). The first of them was a 1 kHz repetition rate femtosecond Ti:Sapphire regenerative amplifier operating at $\lambda = 800$ nm. The pulse compressor of the amplifier was adjusted to precompensate the dispersion caused by the optical elements located in the beam path in order to produce the shortest possible pulse at the sample (~ 100 fs). The second source was an optical parametric amplifier pumped with the regenerative amplifier output and configured to operate at the four other indicated wavelengths (600, 1200, 1300,

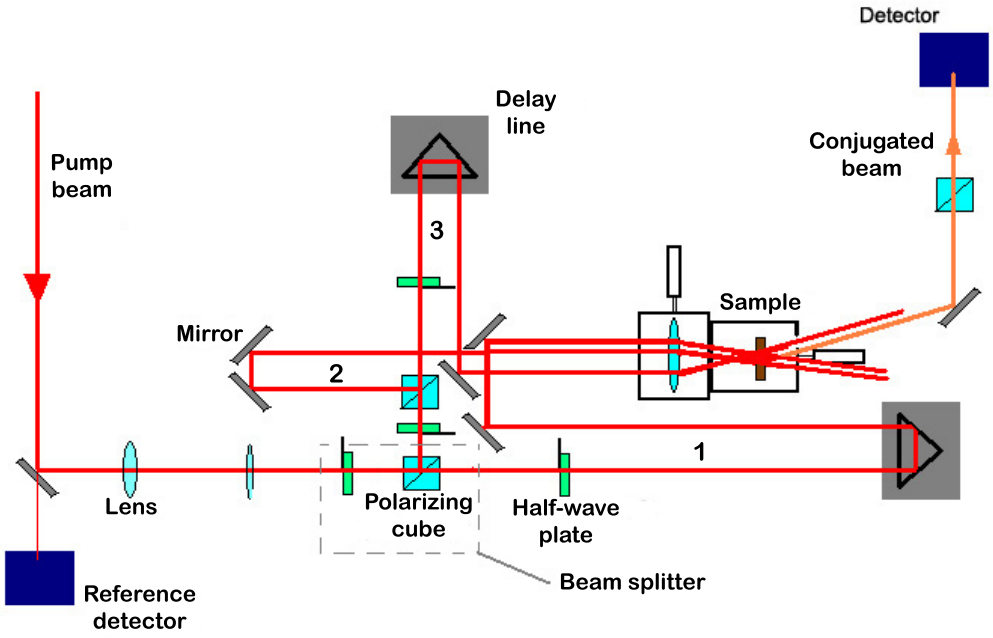

Figure 2.12: Scheme of the degenerate four wave mixing experimental setup.

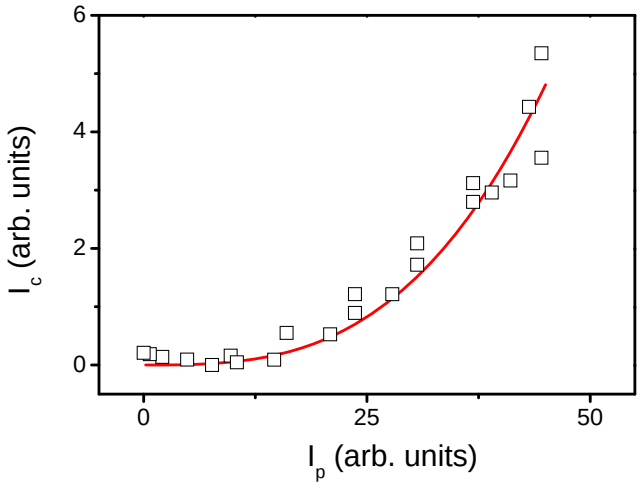

Figure 2.13: (□) Conjugated beam intensity measured for a $90TeO_2 \cdot 5TiO_2 \cdot 5Nb_2O_5$ bulk glass at a wavelength of 1500 nm. I_c has been fitted (red line) according to a cubic dependence with the pump beam intensity.

and 1500 nm). In all cases the contributions from scattered light were subtracted. As an example, Figure 2.13 shows the experimental I_c values and the cubic fitting obtained in the case of a $90TeO_2 \cdot 5TiO_2 \cdot 5Nb_2O_5$ bulk glass sample.

Considerations about the measurement of $\chi^{(3)}$ in thin film samples

The measurement of $\chi^{(3)}$ for film glasses by DFWM is much more complicated than for bulk glasses due to the reduced thickness of the films: while it is of the order of $\sim$ mm in bulk glasses, film samples are typically three orders of magnitude thinner ($\sim \mu$m). This strong thickness difference leads to two different problems that have to be solved in order to achieve reliable measurements in the case of thin film glasses. First, since films are deposited on a 100 μm thick substrate with small but not negligible third optical susceptibility, the nonlinear optical response of the film can be hidden by that of the substrate, *i.e* the contribution of the substrate to the total conjugated signal can exceed by much that of the film. Second, since the measurement of $\chi^{(3)}$ is based on the comparison between the conjugated signals of the sample and a reference, $\chi^{(3)}$ values calculated for the films according to relation 2.18 may yield wrong results if we do not take into account the large thickness difference between the sample and the reference, and the overlapping of the beams at different depths of them.

The total conjugated signal generated by a sample (film + substrate) is the sum of the contributions of the film alone and the substrate. Thus, the film contribution is obtained by subtracting from the total signal the conjugated signal generated from a bare substrate measured under the same experimental conditions. This method is only accurate if the intensity of the conjugated signals generated in the film and the substrate are comparable. Table 2.1 shows the typical values of the thickness and the optical properties, n and $\chi^{(3)}$, of the SiO_2 reference, the glass substrate, and the film glasses considered in the present thesis. According to relation 2.17 and the values shown in Table 2.1, the ratio

Sample	Thickness (μm)	n	$\chi^{(3)}$ (esu)
SiO_2 reference	1000	1.44	1.8×10^{-14}
Glass substrate	100	1.51	3.5×10^{-14}
Film glass	3-4	~ 2	$10^{-13} - 10^{-11}$

Table 2.1: Typical values of the thickness, refractive index and third order susceptibility of samples implicated in the measurement of the nonlinear response of film glasses in the present work.

between the conjugated signal intensity originated in the film (${I_c}^f$) and that of the substrate (${I_c}^s$) will be given by:

$$\frac{{I_c}^{(f)}}{{I_c}^{(s)}} \simeq \frac{1}{60}\frac{\chi^{(3)}_{(f)}}{\chi^{(3)}_{(s)}} \tag{2.19}$$

Therefore, the conjugated intensities from the film and substrate will be comparable only when $\chi^{(3)}_{(f)}$ is at least one order of magnitude larger than $\chi^{(3)}_{(s)}$. On the contrary if $\chi^{(3)}_{(f)} \lesssim \chi^{(3)}_{(s)}$, it is not possible to measure the nonlinear response of the film as the conjugated signal originated in the film can not be discriminated from the signal originated in the substrate.

The nonlinear susceptibilities of tellurite and heavy metal oxide glasses are several orders of magnitude higher than that of fused silica. Therefore, we can use the described method to measure $\chi^{(3)}$ of film glasses. Moreover, the sensitivity of the technique can be improved by reducing the ratio $\frac{{I_c}^f}{{I_c}^s}$. This implies depositing thicker films, using thinner substrates, or minimizing the conjugated signal of the substrate with respect to that of the film during the experiment.

In order to minimize the substrate contribution to the total conjugated signal, one could use, in principle, optics with large numerical apertures so as to minimize the confocal parameter of the beam at the focus. However, this would imply the use of microscope objectives with a small entrance pupil which would make the alignment at the system much more complicated. As an alternative approach it can be useful to locate the film sample in a position with respect to the focusing lens that helps to increase the signal associated to the film with respect to that associated to the sample. Figure 2.14 shows the intensity of the conjugated signal of a bare substrate as a function of its position along the beam propagation axis in the vicinity of the focus of the lens used to overlap the beams in the DFWM experiment. In this case, the lens used has a confocal parameter much larger than the substrate thickness and therefore, we can observe that the intensity of the conjugated signal mirrors the expected Gaussian distribution of intensities associated to the focal volume of a Gaussian beam. Fig. 2.14 clearly shows that the contribution to the conjugated signal of the substrate is maximum when the substrate is located right at the focus of the lens ($\Delta x = 0$ mm) and is smaller as we move away from it.

We can use this to improve to some extent the ratio of the signals associated to the film and the substrate. In the position indicated in Figure 2.15a, both

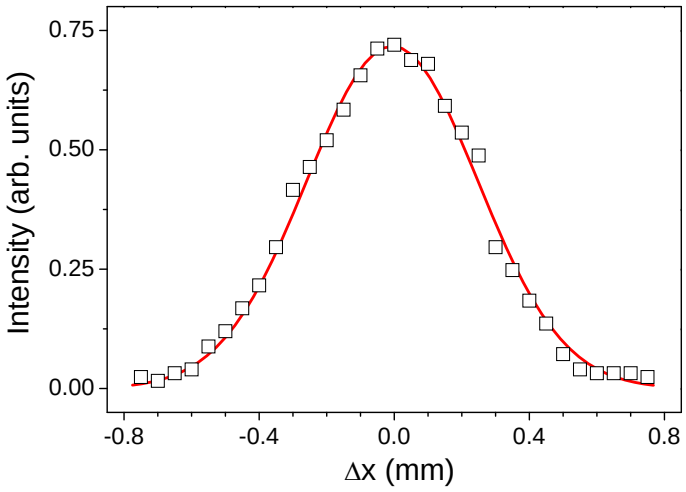

Figure 2.14: (□) Intensity of the conjugated signal of a 100 μm-thick bare substrate measured at different distances from the focus of the lens. The position $\Delta x = 0$ mm corresponds to the maximum intensity detected. The experimental data has been fitted according to a Gaussian function (red line).

the film and the substrate contribute with the same weight to the DFWM signal. However, if we move the sample several hundreds of microns away from the focus, the contribution of the film will be higher, while the contribution of the substrate is reduced by the decrease of the overlapping of the beams as we move away from the focus. We can then estimate an effective overlapping length if we assume that the total conjugated signal generated by the substrate is the sum of the

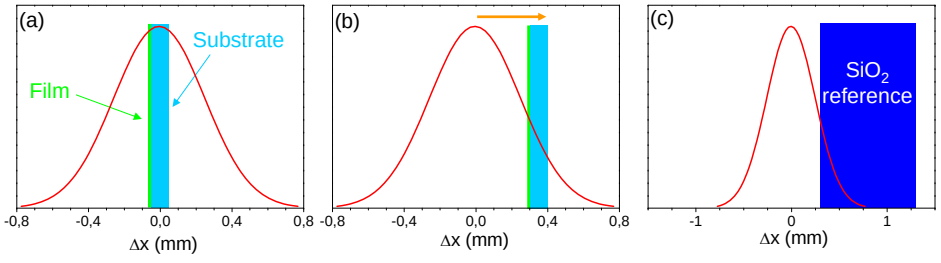

Figure 2.15: Position of the (a,b) film (green line) and substrate (light blue rectangle) and (c) SiO_2 reference (navy blue rectangle) with respect to the the beam overlapping distribution.

conjugated signals generated by differential thicknesses of the substrate weighted by the overlapping distribution Gaussian function, $f(x)$:

$$I_c = \int_{\Delta x_0}^{\Delta x_0 + L_{(s)}} I(x)dx = I_0 \int_{\Delta x_0}^{\Delta x_0 + L_{(s)}} f(x)dx \tag{2.20}$$

where $L_{(s)}$ is the substrate thickness, Δx_0 the distance from the maximum overlapping to the surface of the substrate, and I_0 the intensity of the conjugated signal at Δx_0. We can then define an effective substrate thickness, $L_{(s)}^{eff}$, as the thickness of an equivalent substrate which generates the same total conjugated signal I_c if the overlapping distribution was constant and equal to $f(\Delta x_0)$:

$$I_c = I_0 \int_{\Delta x_0}^{\Delta x_0 + L_{(s)}} f(x)dx = I_0 \int_0^{L_{(s)}^{eff}} f(\Delta x_0)dx \tag{2.21}$$

$$L_{(s)}^{eff} = \frac{1}{f(\Delta x_0)} \int_{\Delta x_0}^{\Delta x_0 + L_{(s)}} f(x)dx \tag{2.22}$$

Thus we can consider $L_{(s)}^{eff}$ as the overlapping length inside the substrate. In the case of the film, we can assume that $f(x)$ is constant within the film due to its small thickness. Therefore, it is not necessary to do the same calculation, since the effective film thickness should be practically equal to the total thickness.

To illustrate this point, we have calculated that by moving the sample away from the focus 300 μm as it is shown in Fig. 2.15b, $L_{(s)}^{eff}$ is 76 μm and the ratio between the conjugated signal intensities increases by $\sim 25\%$:

$$\frac{{I_c}^{(f)}}{{I_c}^{(s)}} \simeq \frac{1}{45} \frac{\chi_{(f)}^{(3)}}{\chi_{(s)}^{(3)}} \tag{2.23}$$

In the case of the reference sample, the difference between the total thickness and the effective thickness is much larger since the reference is 1 mm thick and the pumping beams are only effectively overlapped over a few hundreds of microns inside the sample (Fig.2.15c). For example, in the same conditions than those described above with the reference moved away 300 μm from the focus of the lens, $L_{(r)}^{eff}$ is just 150 μm. In this case, the use of the total reference thickness instead of the effective one for the calculation of $\chi^{(3)}$ of the film can lead to serious mistakes, due to the great difference between the two lengths.

In conclusion, films with thickness of the order of several μm and third order optical susceptibilities at least 10 times higher than those of SiO_2-based glasses ($\sim$

10^{-14} esu) can be characterized by DFWM with an accuracy of around 50%. In these measurements, we have precisely estimated the contribution of the substrate to the total conjugated signal generated by a film sample. We have minimized this contribution by moving away the sample from the center of the overlapping region. Then, the film contribution is isolated by subtracting the contribution of a previously measured bare substrate. Finally, the previous considerations regarding the effective thickness have no sense in the case of bulk samples, since their thicknesses are similar or even larger than the overlapping length. Therefore, the measuring of their conjugated signal or the comparison with the reference are not affected by the finite size of the overlapping region.

Chapter 3

TeO_2-based bulk glasses

In this chapter, we introduce first the vitreous state and describe the general structure and optical properties of oxide glasses. In the case of tellurite glasses, their structure has been previously discussed in the literature and described in terms of the structural units of crystalline TeO_2. Based on these results, we analyze the vitreous network of multicomponent tellurite glasses using Raman spectroscopy in order to determine the effect of the structure on the optical response of bulk and film glasses.

In the first place, the basic structural units are described using the Raman spectrum of a TeO_2–TiO_2–Nb_2O_5 glass with a high molar content of TeO_2 (90 mol%). These results are the basis to study the structure of different glasses with lower TeO_2 molar content belonging to the TeO_2–WO_3–R_xO_y and TeO_2–WO_3–PbO systems. Finally, the linear optical properties of these glasses, namely their refractive indexes and transmission spectra, are determined and discussed in terms of the glass composition and network structure.

3.1 The vitreous state

Glasses are materials with particular structural, physical and chemical properties that render them difficult to define or classify, as it is proven by the fact that there is not a universally accepted definition for vitreous state. They show a high structural disorder similar to that of liquids, but their mechanical properties are typical of brittle solids. A large number of materials in a wide range of compositions can be produced in vitreous state and, furthermore, there is no need of stoichiometric relations between the components of multicomponent glasses. The most widely known glasses are those based on SiO_2, but there are many oxides that can be obtained in vitreous state, like P_2O_5, B_2O_3, GeO_2, TeO_2, or heavy metal oxides among others. Moreover, glasses can also be made from other inorganic chemical compounds such as halides, chalcogenides, oxysalts, or certain metallic alloys, and finally, even fundamental organic compounds like the poly(methyl methacrylate) (PMMA) or the polyethylene are also considered vitreous materials.

A suitable definition of glass could be based on the phase transition between the liquid and the vitreous state: a glass is a material that can be cooled below and heated above continuously and reversibly between the melted and the rigid states, without the apparition of any crystalline phase.[59] If we consider a material in equilibrium in its liquid state, when it is slowly cooled down to its melting temperature, T_f, the liquid crystallizes and the specific volume of the material suddenly decreases. However, if the cooling process is fast enough, namely faster than the crystallization rate, the melted material remains liquid in a super-cooled state, as it is shown in Figure 3.1. The viscosity of the melt grows as the cooling process continues until a temperature at which the liquid reaches such a high viscosity ($\sim 10^{12}$ Pa s) that it becomes rigid and brittle and thus, its mechanical properties result similar to that of a solid material. In this case, the variation of the specific volume with the temperature is continuous.[59, 93] The temperature at which the transition between the super-cooled liquid and the glass occurs is called the glass transition temperature, T_g. However, this is not a well defined transition temperature since the glass transition is continuous between the two states and the exact value of T_g depends on the cooling process.[93] Unlike crystalline phases which are stable phases, the vitreous state is thermodinamically metastable and the increase of its temperature above T_g for a time long enough could lead the glass to show signs of crystallization (devitrification).[59]

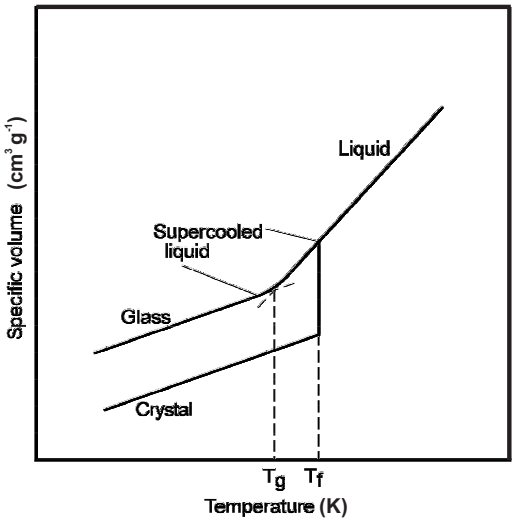

Figure 3.1: Relationship between the specific volume and the temperature in the transition from the liquid state to the vitreous and the crystalline state. Figure taken from ref. [59].

Therefore, glasses are non crystalline solids and they lack the long-range regularity characteristic of crystals. However, glasses are not amorphous materials either, since they show short-range regularity.[59] There are different models that describe the structure of glass,[59] but the most intuitive model that allows understanding most of its properties is the Zachariasen's random network model.[94] This model proposes that both the crystalline and the vitreous state of a given material consist of the same basic structural units, but the relative orientation of these units is different in the glass with respect to the crystal. In the latter case the structural units are periodically arranged while in glasses they are randomly bonded. To illustrate this idea, Figure 3.2 shows a plane view of the crystalline SiO_2 structure (Fig. 3.2a) and a scheme of vitreous SiO_2 (Fig. 3.2b). In the first case, the network consists of periodically ordered [SiO_4] tetrahedra, in which each Si atom is bonded to four O atoms. Three of these O atoms are shown in Fig. 3.2a while the fourth O atom is in a plane above or below the one shown. In the case of vitreous SiO_2, the [SiO_4] tetrahedra are randomly arranged in space. Therefore, while the short-range regularity is maintained, the long-range regularity is completely lost. This lack of long-order regularity allows considering glasses as isotropic solids. Moreover, glasses have a continuous structure without any grain boundaries, although they can show microstructural heterogeneities due to inmiscibilities of some of its components during the preparation of the

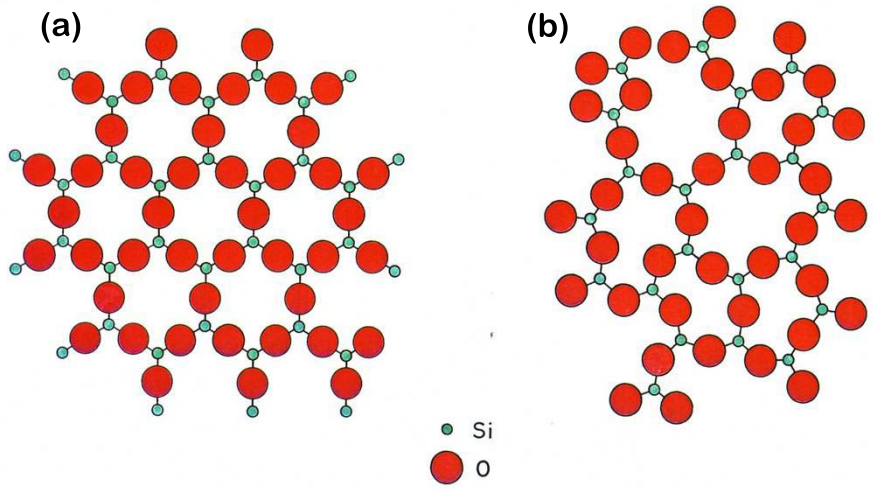

Figure 3.2: Schemes of (a) crystalline and (b) vitreous network of SiO_2. Figures taken from ref. [59].

glass.

SiO_2 is able to form a glass network as shown in Fig. 3.2b. Oxides that present this ability are known as network formers. In this case, each Si atom is bonded with other Si atoms through oxygen atoms, which are called bridging oxygens (BO). However, glasses typically have more than one component, and in this case not all the oxides play an equivalent role. Figure 3.3 shows the Zachariasen's model for a binary glass SiO_2–Na_2O, where the incorporation of Na_2O breaks the Si-O-Si linkages. In this case, there is a second type of oxygens, called nonbridging oxygens (NBO), which are only bonded to one Si atom and do not contribute to the formation of the glass network. Oxides that act like Na_2O are called network modifiers. The role of network modifiers in the glass structure is very important since they break the glass network and weaken the structure, easing the melting of the glass, but reducing its thermal stability and favoring its crystallization

The modifications induced in the glass network by the addition of different components or due to the glass preparation process have a significant effect on the chemical and physical properties of the glass and thus, these modifications determine the suitability of a glass for a particular application. In the case of the

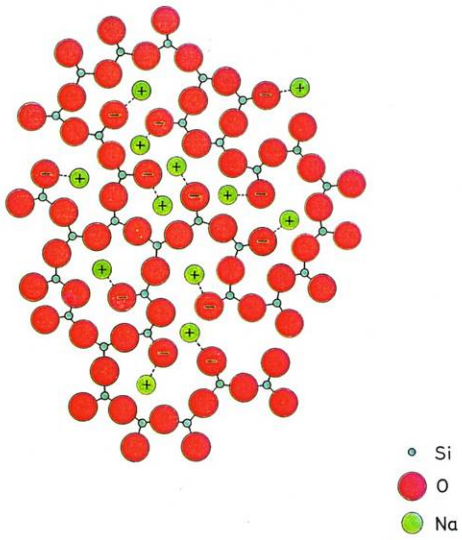

Figure 3.3: Scheme of the glass network of SiO_2-Na_2O taken from ref. [59].

present work, we are focussed on the relation between the structure of the glass and its optical properties as discussed in the following sections.

3.1.1 Optical properties of oxide glasses

The optical response of glasses is typically characterized by three different properties: optical transmission spectral range, and linear and nonlinear refractive indexes.

Since there are neither grain boundaries nor interfaces within glass structures, the intrinsic scattering losses of a glass are very small. Therefore, glasses are transparent in the region where intrinsic absorption does not occur.[11] In the case of oxide glasses, this region usually ranges from near-UV to near-IR. The UV absorption is due to the excitation of electrons. Glasses are dielectric materials without free electrons and thus, they are transparent in the visible region.[87] Only UV photons have enough energy to excite the electrons which are forming the oxygen bonds in the network to higher energy levels. Therefore, the position of the UV absorption edge is determined by the electron binding energies which are related to the bonding energy of the atoms in the network.[59] On the opposite extreme of the transparency region, the vibration modes of the structural units

that form the glass network are the origin of the IR absorption. The frequency of these vibrations and, thus, the position of the IR absorption edge are related to the type of vibration (bonding, stretching,...), the atomic mass of the atoms that vibrate, and the force of the linkages that bonds the atoms.[59] Apart from the intrinsic absorption, it is important to take also into account the scattering due to possible glass heterogeneities (gas bubbles, undissolved particles or microcrystallization), and the absorption due to impurities, dopants, or vibrations of the hydroxyl group (OH^-) in the range 2.8–3.5 μm.[11, 59, 87, 93] These absorption sources are related to the preparation of the glass and the purity of the starting reagents. Therefore, the fabrication of good optical quality glasses demands a high control of the production process.

In the transparency range, the optical properties of a glass are usually described in terms of its refractive index. The linear and nonlinear refractive indexes are macroscopic measurements of the distortion of the atomic electron clouds by the electromagnetic field of an external incident light beam. This field distorts the electron cloud in a quantity determined by the polarizability, α, of the atom or the molecule.[11] Therefore, materials including atoms with large polarizabilities easily interact with the light and they are characterized by high refractive indexes, according to the Lorentz-Lorenz formula [73]:

$$\frac{4}{3}\pi N\alpha = \frac{n^2-1}{n^2+2} \tag{3.1}$$

where N is the number of molecules per unit volume.

Finally, the nonlinear refractive index arises from the nonlinear terms of the polarization induced in the glass by the external electromagnetic field. The nonlinear response may be dominated by either resonant processes, produced by electronic transitions, or by nonresonant processes involving distortions of the electron cloud.[18] Electronic transitions imply absorption and attenuation of the propagating optical signal, while the nonresonant response is caused by photons with energies far from any fundamental absorption. As a consequence, the nonlinear nonresonant response is smaller than its resonant counterpart and it is only significant for intense optical fields, but it has fast response times ($\lesssim 10^{-12}$ s) and minimum power dissipation by absorption.[16] Both properties make nonresonant nonlinear glasses highly adequate for the development of photonic devices such as ultra-fast optical switches.[11]

The microscopic origin of the nonlinear response of a glass can be understood

in terms of the hyperpolarizability of the constituents in a manner analogous to the description of the linear optical response in terms of the polarizability.[13] Several simple, semi-empirical models have been proposed to predict the nonlinear susceptibility of a material from its linear optical properties,[95, 96, 97] as it is widely known that glasses with high linear refractive indexes show large nonlinear optical responses [13, 18] since atoms with large polarizabilities show large hiperpolarizabilities too.[16, 98, 99] All of them have in common that the higher the linear refractive index, the larger the nonlinear susceptibility, as it is proposed in the extremely simple Miller's rule [16]:

$$\chi^{(3)} \propto n^4 \tag{3.2}$$

Qualitatively, the linear and nonlinear response will be largest in materials that contain large numbers of highly polarizable loosely bound valence electrons. [18] In the case of oxide glasses, this translates into oxides containing empty d band transition metal (TM) cations like Ti^{4+}, V^{5+}, Cr^{6+}, Mo^{6+}, W^{6+}, Nb^{5+}, Ta^{5+},... or heavy metal (HM) cations like Pb^{2+}, Bi^{3+}, or Tl^{+}.[16, 18] Moreover, the glass network structure also affects the nonlinear optical response since the presence of NBO, more polarizable than the BO, in SiO_2-based glasses increases the linear and nonlinear refractive indexes.[13, 59, 100] However, among the different contributions to the hyperpolarizability, there is not an universal agreement in the literature regarding which is the dominant factor. Depending on the glass composition, the presence of NBO, HM oxides, TM oxides, or even structural factors have been pointed to be responsible for high nonlinear refractive indexes.[16]

Since one of the objectives of the present thesis is the production of glasses with large nonlinear indexes, we will focus on those glasses with the most promising compositions to achieve such a goal. According to Lines,[18] transition or heavy metal cations are the best potential candidates to enhance the glass nonlinear optical response. However, since neither TM nor HM oxides are single-component glass network formers in their own right, it is necessary to consider multicomponent glasses. Among the glass forming oxides, TeO_2 stands out since TeO_2-based glasses have refractive indexes higher than 2 and some of the highest nonlinear refractive indexes among oxide glasses (10 – 100 times larger than that of SiO_2) and comparable to those of the TM or HM oxides.[20] However, the exact origin of the nonlinearity of tellurite glasses is still object of active research. The high hyperpolarizability of TeO_2 has been attributed to the empty

$5d$ orbitals [101] or the electron lone pair at the Te atom,[102] whereas recent *ab initio* calculations have also related the hyperpolarizability of TeO_2 glass to the network structure.[103]

3.2 Tellurite glasses

The different multicomponent tellurite glasses considered in the present thesis have been designed in order to improve their nonlinear optical response. We have used TeO_2 as network former, while different TM oxides (TiO_2, Nb_2O_5, Ta_2O_5, WO_3, and Nb_2O_5) and HM oxides (Bi_2O_3 and PbO) have been chosen as network modifiers. Three different glass systems have been considered in the present work: TeO_2–TiO_2–Nb_2O_5, TeO_2–WO_3–R_xO_y, where R_xO_y is one the oxides mentioned before, and TeO_2–WO_3–PbO. Table 3.1 summarizes the molar composition of the glasses corresponding to the three different systems studied.

Glass system	Sample name	Molar composition (mol%)
TeO_2–TiO_2–Nb_2O_5	TTN	$90TeO_2 \cdot 5TiO_2 \cdot 5Nb_2O_5$
TeO_2–WO_3–R_xO_y	TW15	$85TeO_2 \cdot 15WO_3$
	TW20	$80TeO_2 \cdot 20WO_3$
	TWTi	$80TeO_2 \cdot 15WO_3 \cdot 5TiO_2$
	TWNb	$80TeO_2 \cdot 15WO_3 \cdot 5Nb_2O_5$
	TWTa	$80TeO_2 \cdot 15WO_3 \cdot 5Ta_2O_5$
	TWLa	$80TeO_2 \cdot 15WO_3 \cdot 5La_2O_3$
	TWBi	$80TeO_2 \cdot 15WO_3 \cdot 5Bi_2O_3$
	TWPb	$80TeO_2 \cdot 15WO_3 \cdot 5PbO$
TeO_2–WO_3–PbO	TWPb1	$85TeO_2 \cdot 15WO_3$
	TWPb2	$80TeO_2 \cdot 20WO_3$
	TWPb3	$80TeO_2 \cdot 15WO_3 \cdot 5PbO$
	TWPb4	$80TeO_2 \cdot 10WO_3 \cdot 10PbO$
	TWPb5	$80TeO_2 \cdot 20PbO$
	TWPb6	$70TeO_2 \cdot 20WO_3 \cdot 10PbO$
	TWPb7	$70TeO_2 \cdot 10WO_3 \cdot 20PbO$
	TWPb8	$60TeO_2 \cdot 30WO_3 \cdot 10PbO$
	TWPb9	$60TeO_2 \cdot 20WO_3 \cdot 20PbO$
	TWPb10	$50TeO_2 \cdot 30WO_3 \cdot 20PbO$

Table 3.1: Glass system, sample name, and molar composition of bulk glass samples considered. TWR- and TWPb-series have several samples in common, which have been named differently depending on the series in order to keep the name coherence: sample TWPb1 is the same as TW15, TWPb2 as TW20, and TWPb3 as TWPb.

The glass $90TeO_2 \cdot 5TiO_2 \cdot 5Nb_2O_5$, with a large TeO_2 molar content, has been selected as starting point since the LPG group had previous experience in the TeO_2–TiO_2–Nb_2O_5 system.[88] This composition has been considered to study and describe the basic structural units of TeO_2-based glasses. Thereafter, we have considered the other network modifiers mentioned. In particular, we have selected the system TeO_2–WO_3–R_xO_y, in which we intended to study the effect of substituting mol by mol a small quantity (5 mol%) of TeO_2 in a binary TeO_2–WO_3 glass by different R_xO_y oxides (TWR-series). Among these glasses, we have selected the system TeO_2–WO_3–PbO, due to its large glass forming region and the presence of a heavy metal cation such as Pb^{2+}, to perform a study of the glass properties along the vitrification region. Figure 3.4 shows the glass samples prepared in the latter system. Transparent glasses were produced either with contents of PbO below 30 mol% or WO_3 below 40 mol%, while for higher PbO or WO_3 contents samples devitrified. Samples with very low contents of WO_3 and PbO could not be produced. The extension of the devitrified region agrees with previous results in this system.[104, 105] Among all the prepared transparent glasses shown in Fig. 3.4, we have selected 10 representative samples (TWPb-series), summarized in Table 3.1, that allow studying the effect of varying the relative content of TeO_2, WO_3, and PbO on the structure and optical properties.

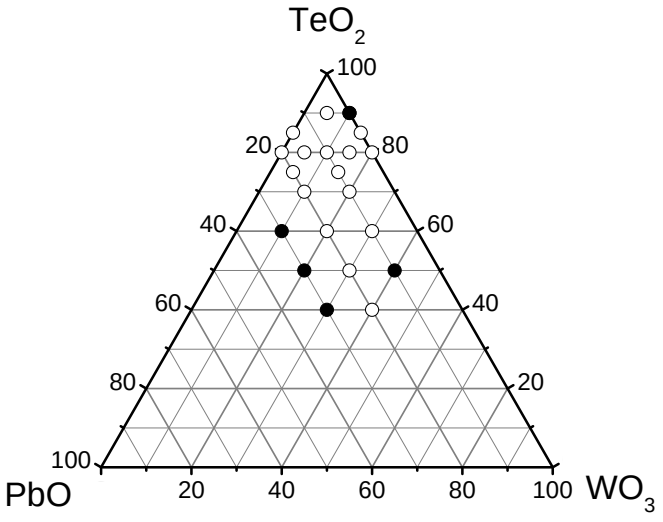

Figure 3.4: (○) Transparent glasses and (●) devitrified samples prepared in the system TeO_2–WO_3–PbO.

3.2.1 Structure of tellurite glasses

The structure of tellurite glasses has been studied since the 80s taking as starting point the crystalline TeO_2.[20] Crystalline TeO_2 has two polymorphic forms: tetragonal α-TeO_2 (paratellurite) and orthorhombic β-TeO_2 (tellurite), although in the last years new crystalline phases have been reported.[106] The structure of TeO_2 glass is accepted to be similar to the network of α-TeO_2 in which the Te is fourfold coordinated and the basic structural unit is [TeO_4] (Figure 3.5). This unit has the shape of a trigonal bipyramid (tbp), formed by two unequivalent pairs of oxygen atoms: two equatorial oxygens (O_{eq}) at a distance of 1.9 Å from the Te atom and two axial oxygens (O_{ax}) at 2.1 Å. The tbp is distorted due to the Te electron lone pair, placed in the equatorial plane. The angle O_{eq}-Te-O_{eq} is 102.0° while the angle O_{ax}-Te-O_{ax} is 168.5°.[107] The crystalline network is built up by [TeO_4] tbp units with each oxygen atom shared by two units and bonded in the equatorial position to one Te atom and in the axial position to another (Te-$_{eq}O_{ax}$-Te linkages).

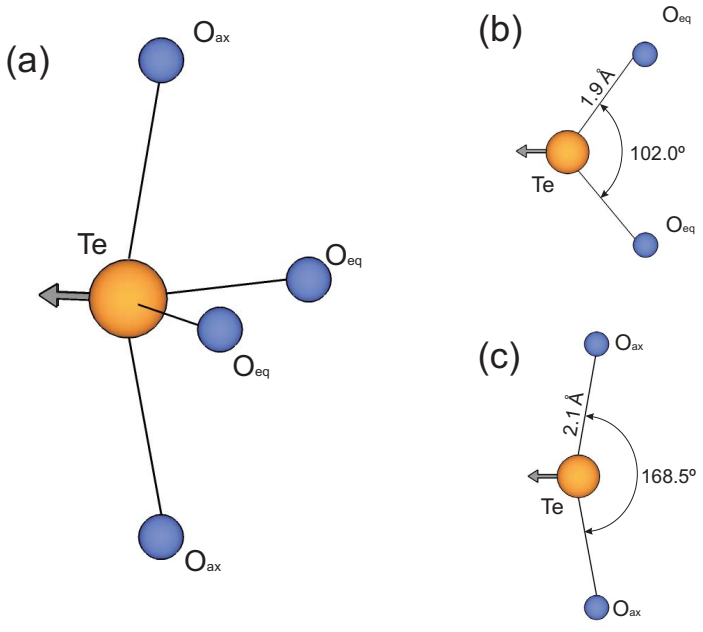

Figure 3.5: (a) [TeO_4] trigonal bipyramid structural unit, which is formed by two unequivalent pair of oxygen atoms: (b) two equatorial oxygens (O_{eq}) and (c) two axial oxygens (O_{ax}). The arrow indicates the position of the electron lone pair of Te^{4+}.

In the case of glasses, due to the more disordered state of the glass network and the presence of network modifiers, some of the Te-$_{eq}$O$_{ax}$-Te linkages are broken and there is a transition in the Te coordination state from 4 to 3. The main structural unit is still the [TeO_4] tbp (Figure 3.6a) but now new structural units appear like the [$TeO_{3+\delta}$] polyhedra (Fig. 3.6b) and the [TeO_3] trigonal pyramids (tp) (Fig. 3.6c). The structural units in which the linkage is broken have a Te-O^- NBO while one of the other Te-O bonds elongates up to a distance higher than 2.2 Å (coordination 3+δ, $0 < \delta < 1$).[108] If the long bond is cleaved this implies the formation of a structural unit with coordination 3 ([TeO_3] tp) with one or two NBO (Te-O^- or doubled bonded oxygen atoms Te=0), stabilized by the resonance between them.[108].

The structure of tellurite glasses and the process of network breaking by the addition of network modifiers have been previously studied by IR absorption and Raman spectroscopy.[20] Sekiya *et al.* [109] compared the Raman spectra of α-TeO_2 and β-TeO_2 with that of pure TeO_2 glass (Figure 3.7). The Raman spectra of the latter was deconvoluted using Gaussian peaks and the frequency of the deconvoluted peaks agreed with the frequencies of the peaks observed in α-TeO_2 (400, 600, and 660 cm^{-1}). In a later work, the same author [108] also studied

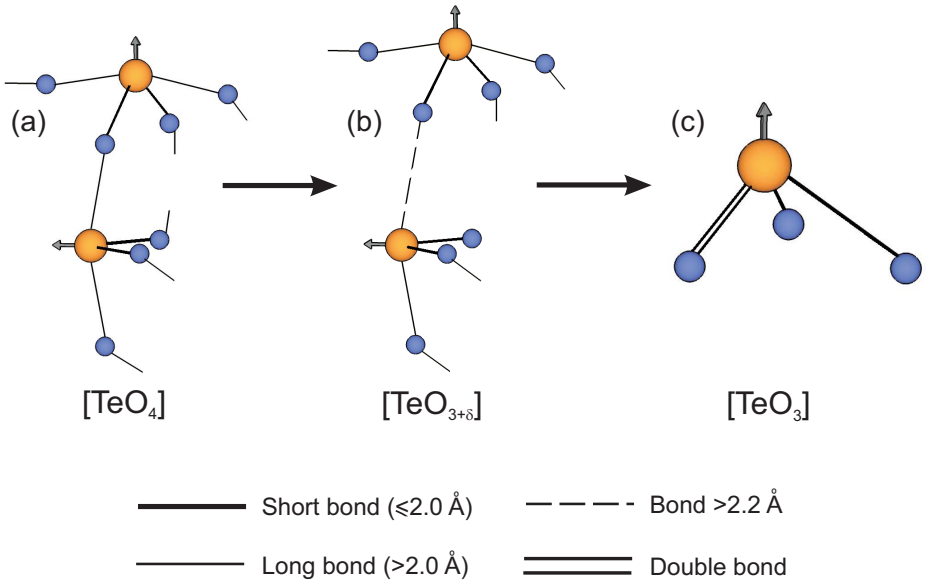

Figure 3.6: Structural units observed in TeO_2-based glasses: (a) [TeO_4] tbp (coordination 4), (b) [$TeO_{3+\delta}$] polyhedra (coordination 3+δ, $0 < \delta < 1$), and (c) [TeO_3] tp (coordination 3). The width and the style of the lines representing the Te-O bonds correspond to different bond lengths and types as indicated in the legend.

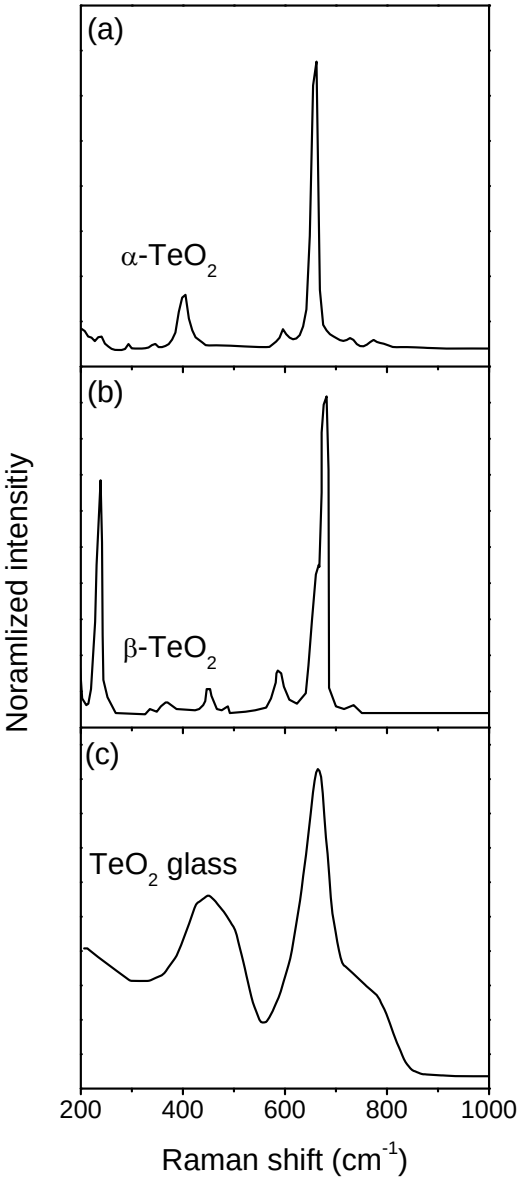

Figure 3.7: Raman spectra of (a) α- and (b) β-TeO_2 crystalline phases and (c) pure TeO_2 glass. Graphs taken from ref. [109].

the Raman spectra of different TeO_2-based glasses, assigning the deconvolunted Gaussian peaks to the vibrations of TeO_2 structural units. The results obtained in these works have been the basis of the structural characterization of different TeO_2-based glasses in a wide range of compositions and systems, like TeO_2–Tl_2O,[110] TeO_2–RO (R = Mg, Sr, Ba, and Zn),[111] TeO_2–R_2O_3 (R = B, Y, In, and La),[112, 113] TeO_2–RO_2 (R = Hf and Th),[114] TeO_2–Nb_2O_5,[115] TeO_2–RO_3 (R = W and Mo),[116, 113] TeO_2–BaO–SrO–R_2O_5 (R = Nb and Ta).[117, 118]

Structure of $90TeO_2 \cdot 5TiO_2 \cdot 5Nb_2O_5$ glass

We have chosen the glass $90TeO_2 \cdot 5TiO_2 \cdot 5Nb_2O_5$ as starting point to characterize the structure of bulk and film tellurite glasses. The high TeO_2 molar content of the glass (90 mol%) suggests that its Raman spectrum should be similar to that of pure TeO_2 glass.

The measured Raman spectrum is shown in Figure 3.8. It has the same three main bands at 400 – 550 cm^{-1}, 600 – 700 cm^{-1} and 700 – 850 cm^{-1} than TeO_2 glass (Fig. 3.7c). The spectrum has been deconvoluted in Gaussian peaks in the range from 300 to 1100 cm^{-1}. Most of the peaks correspond to different

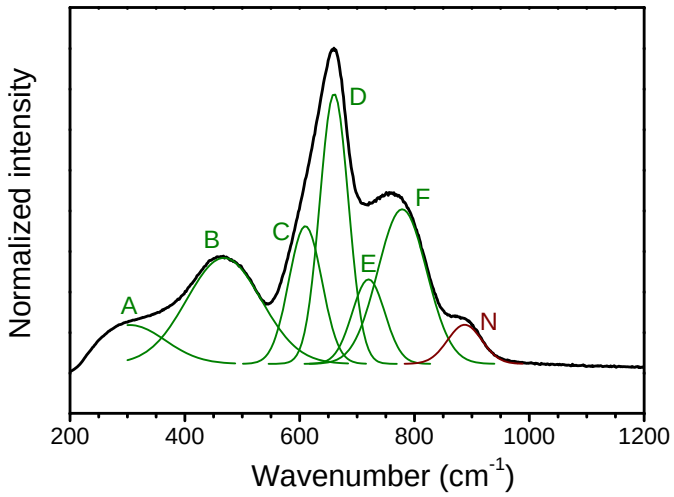

Figure 3.8: Raman spectrum and peak deconvolution of a $90TeO_2 \cdot 5TiO_2 \cdot 5Nb_2O_5$ glass. Peaks A – F are assigned to vibrations of TeO_2 structural units while peak N is assigned to vibrations of $[NbO_6]$ structural units.

vibrations of TeO_2 structural units as described below [108] and summarize in Table 3.2:

- A broad peak (A) at low frequencies, around 305 cm^{-1}, that is assigned to the bending vibrations of [TeO_3] tp.
- Peak B at 470 cm^{-1} that is assigned to the stretching and bending vibrations of Te-O-Te linkages formed by vertex-sharing [TeO_4] tbp, [$TeO_{3+\delta}$] polyhedra, and [TeO_3] tp. The presence of this peak indicates a continuous glass network.
- Peak C at 610 cm^{-1} that is related to the vibration of a continuous network composed of [TeO_4] tbp.
- An intense peak D at 660 cm^{-1} that is due to antisymmetric vibrations of Te-$_{eq}$O$_{ax}$-Te linkages (Fig. 3.6a). This peak is also the main peak in the α-TeO_2 spectrum since its network comprises Te-$_{eq}$O$_{ax}$-Te linkages.
- Peaks E and F, at 720 and 780 cm^{-1} respectively, are both assigned to stretching vibrations between Te and NBO in [$TeO_{3+\delta}$] polyhedra and [TeO_3] tp units (Fig. 3.6b and 3.6c). The frequency of the vibration depends not only on the linkage, but also on the surrounding atoms. In peak F the NBO has little interaction with adjacent Te atoms while in peak E the NBO strongly interacts with adjacent Te atoms and thus the vibration is shifted towards lower frequencies.
- Finally, there is also a small peak at 885 cm^{-1}, named N. This peak is not related to the TeO_2 network but to the presence of highly distorted [NbO_6] octahedral structural units.[117, 119]

Peak	Position (cm^{-1})	Assignment
A	305	bending of [TeO_3] units
B	470	stretching and bending of Te-O-Te linkages
C	610	vibration of a continuous [TeO_4] network
D	660	antisymmetric vibrations of Te-$_{eq}$O$_{ax}$-Te linkages
E	720	stretching of NBO with strong interaction with adjacent Te atoms
F	780	stretching of NBO with little interaction with adjacent Te atoms
N	885	Nb-O vibrations in [NbO_6] units

Table 3.2: Assignment of peaks observed in the deconvoluted Raman spectrum of the $90TeO_2 \cdot 5TiO_2 \cdot 5Nb_2O_5$ glass.

Structure of TeO_2–WO_3–R_xO_y glasses

The composition of glasses belonging to the system TeO_2–WO_3–R_xO_y (TWR-series) is the same in a 95 mol%, but each one has an additional 5 mol% of different oxides, as it is shown in Table 3.3. In spite of this small compositional differences, the addition of that third oxide has an important effect on the glass network.

Sample	Molar composition (mol%)
TW15	$85TeO_2 \cdot 15WO_3$
TW20	$80TeO_2 \cdot 20WO_3$
TWTi	$80TeO_2 \cdot 15WO_3 \cdot 5TiO_2$
TWNb	$80TeO_2 \cdot 15WO_3 \cdot 5Nb_2O_5$
TWTa	$80TeO_2 \cdot 15WO_3 \cdot 5Ta_2O_5$
TWLa	$80TeO_2 \cdot 15WO_3 \cdot 5La_2O_3$
TWBi	$80TeO_2 \cdot 15WO_3 \cdot 5Bi_2O_3$
TWPb	$80TeO_2 \cdot 15WO_3 \cdot 5PbO$

Table 3.3: Molar composition of TWR-series bulk glasses.

The network of TeO_2–WO_3 glasses is mainly built up by the already described structural units of TeO_2 glasses ($[TeO_4]$ tbp, $[TeO_{3+\delta}]$ polyhedra and $[TeO_3]$ tp), but the glass network is deeply affected by the inclusion of WO_3. WO_3 acts as conditional network former, since its addition breaks the Te-O-Te linkages with the formation of new W-O-W and W-O-Te linkages that contribute to the glass network.[82, 116] WO_3 forms $[WO_6]$ octahedral units with W^{6+} cations in a sixfold coordination, as shown in Figure 3.9,[82] in which one of the oxygen atoms is double bonded to the W atom. The modifications in the network induced by the presence of $[WO_6]$ have their fingerprint effect on the Raman spectra.

Figure 3.10 shows the Raman spectrum of a $85TeO_2 \cdot 15WO_3$ binary glass (TW15). The spectrum has the same general shape as the spectrum of the $90TeO_2 \cdot 5TiO_2 \cdot 5Nb_2O_5$ glass (Fig. 3.8), but with broader bands in the 700-900 cm^{-1} region and a strong peak around 925 cm^{-1}. This spectrum has been deconvoluted in 8 Gaussian peaks assigned according to the the vibrations of TeO_2 structural units and $[WO_6]$ units,[82, 108, 116] as it is summarized in Table 3.4. Peaks B centered at 485 cm^{-1}, C at 605 cm^{-1}, D at 660 cm^{-1}, E at 730 cm^{-1} and F at 805 cm^{-1} are assigned to the same vibrations of the TeO_2 network as in the case of $90TeO_2 \cdot 5TiO_2 \cdot 5Nb_2O_5$ glass, while the three remaining peaks (X, Y and Z) are related to vibrations of $[WO_6]$ octahedra:

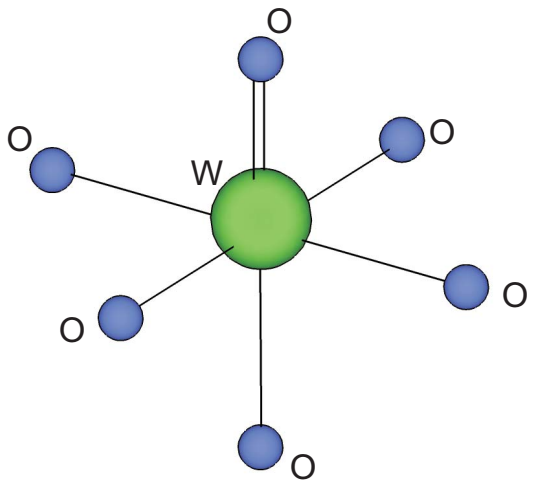

Figure 3.9: $[WO_6]$ octahedral structural unit present in tungsten-tellurite glasses. The upper oxygen atom is double bonded to the W atom.

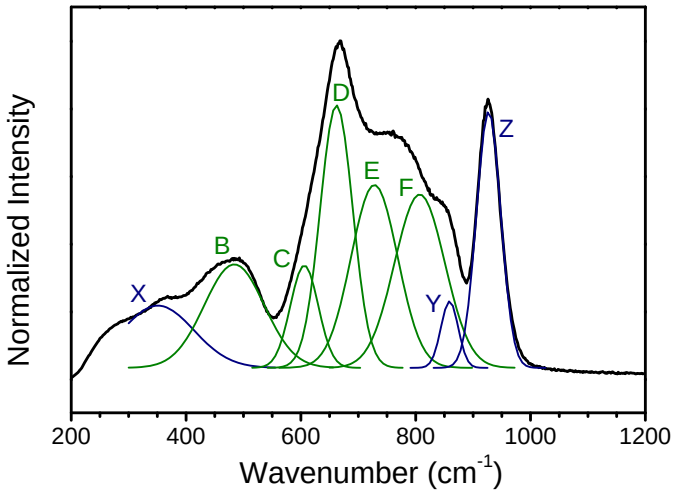

Figure 3.10: Raman spectrum and peak deconvolution of a $85TeO_2{\cdot}15WO_3$ binary glass. Peaks B – F are assigned to vibrations of TeO_2 structural units while peaks X, Y, and Z are assigned to vibrations of $[WO_6]$ structural units.

Peak	Position (cm^{-1})	Assignment
X	350	deformation vibrations of [WO_6]
B	485	stretching and bending of Te-O-Te linkages
C	605	vibration of a continuous [TeO_4] network
D	660	antisymmetric vibrations of Te-$_{eq}$O$_{ax}$-Te linkages
E	730	stretching of NBO with strong interaction with adjacent Te atoms
F	805	stretching of NBO with little interaction with adjacent Te atoms
Y	860	stretching of W-O bonds in [WO_6]
Z	925	stretching vibration of the double bond W=O in [WO_6]

Table 3.4: Assignment of the peaks observed in the deconvoluted Raman spectrum of the $85TeO_2{\cdot}15WO_3$ glass.

- Peak X, centered at 350 cm^{-1}, is assigned to deformation vibrations of [WO_6] units. The bending vibrations of [TeO_3] tp (peak A in Fig. 3.8) should also contribute to peak X and thus worsen the fitting at low frequencies.

- Peak Y at 860 cm^{-1} is assigned to the stretching vibrations of W-O bonds.

- Peak Z at 925 cm^{-1} is assigned to the stretching vibration of the W=O double bond.

Furthermore, there should be a non negligible contribution of the vibration of Te-O-W linkages to the Raman spectra around 730 cm^{-1}.[82, 116] The increase of the intensity and the shift towards higher frequencies of peaks E, from 720 to 730 cm^{-1}, and F, from 780 to 805 cm^{-1}, observed in this case when compared to the spectra of $90TeO_2 \cdot 5TiO_2 \cdot 5Nb_2O_5$, are most likely related to that contribution.

The effect of the addition of a third component on the glass structure can be investigated through its impact on the Raman spectra. Figure 3.11 shows the spectra in the range between 200 to 1200 cm^{-1} measured for TWR-series glasses containing a constant WO_3 molar content (15 mol%). Since all glasses have the same amount of WO_3, the intensity of the peak at 925 cm^{-1} should be similar in all cases. Therefore, Raman spectra have been normalized in all cases to the intensity of that peak, and they have been deconvoluted using Gaussian peaks according to the peak assignment of the TW15 binary glass summarized in Table 3.4.

Spectra of glasses containing TiO_2, Nb_2O_5 and Ta_2O_5 are similar to that of

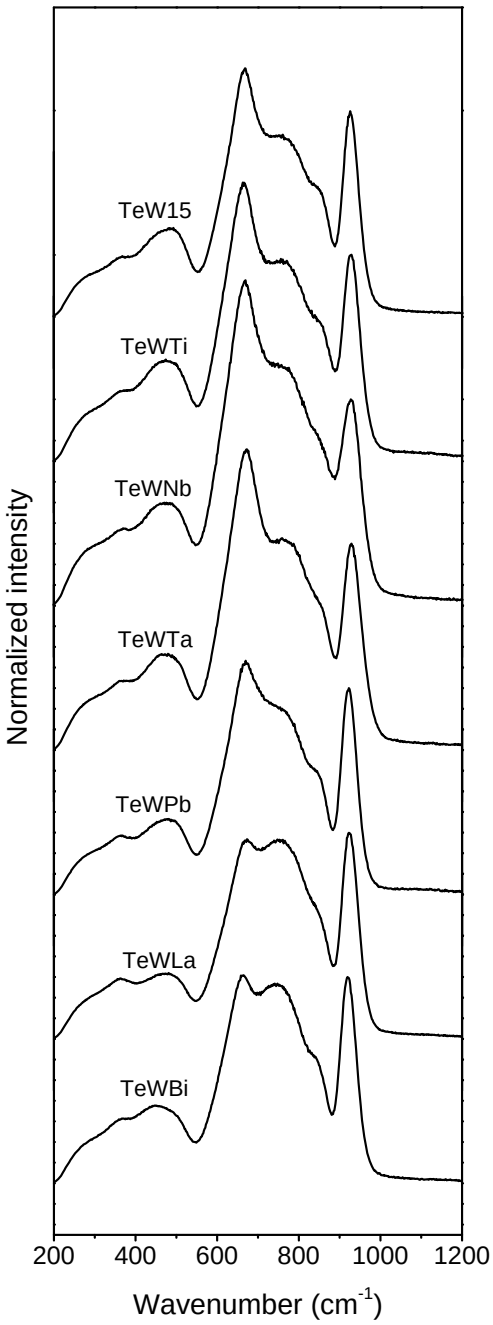

Figure 3.11: Raman spectra of glasses belonging to the TeO_2–WO_3–R_xO_y system with a constant molar content of WO_3 (15 mol%). The intensity is normalized in all cases to the intensity of the peak at 925 cm^{-1}, related to the vibration of W=O bonds.

the binary glass. However, glasses containing PbO, La_2O_3 and Bi_2O_3 show an enhancement of the width (TWPb) and the intensity (TWLa and TWBi) of the band at 700-800 cm^{-1}, while the relative intensity of the main peak at 660 cm^{-1}, due to Te-O-Te linkages in [TeO_4] tbp continuous network, clearly decreases. This decrease of the band at 660 cm^{-1} and the increase of the width and intensity of the 700-800 cm^{-1} band indicate a change in the coordination of Te atoms, from 4 ([TeO_4] tbp) to 3 ([TeO_3] tp). Therefore, the addition of Pb, Bi, and La breaks the Te-O-Te linkages and increases the fraction of NBO in the network.

The structural changes induced by the different cations can be understood in terms of their role in the network as formers or modifiers, which is determined by the properties of the chemical bonding established by them. The ability of different oxides to form a glass network has been successfully discussed in terms of the field intensity of the cations, which quantifies the polarization of the surrounding anions due to the charge and size of each cation. It can be estimated from the electrostatic force between the cation and the anion.[59] For a cation with charge Z_c, bonded to a anion with charge Z_a, that force F is:

$$F \propto \frac{Z_c Z_a e^2}{a^2} \tag{3.3}$$

where e is the electron charge and a the distance between the cation and the anion, *i.e.* the sum of their ionic radii. Since in the present work the anion is O^{2-} in all cases, $Z_a e^2$ is considered constant. We can define then the field intensity, f, as:

$$f = \frac{Z_c}{a^2} \tag{3.4}$$

The values of coordination index,[120] ionic radius,[121] and field intensity for the cations considered in the present thesis are shown in Table 3.5.

It is empirically known that oxides of cations having high field intensities are network formers while low values of f correspond to network modifiers [59] and thus, it is possible to relate f of the different cations to the fraction of NBO induced in the network by their presence. The amount of NBO in TeO_2-based glasses can be qualitatively estimated through the ratio (I_R) between the intensities of the deconvoluted peaks E (I_E) and F (I_F) related to NBO vibrations, and the intensity of peak D (I_D) at 660 cm^{-1}, related to the [TeO_4] tbp continuous network [110, 122, 123]:

$$I_R = \frac{I_E + I_F}{I_D} \tag{3.5}$$

Ion	Coordination index	Ionic Radius (Å)	Field Intensity
O^{2-}	-	1.40	-
Pb^{2+}	8	1.29	0.28
La^{3+}	7	1.10	0.48
Bi^{3+}	6	1.03	0.51
Te^{4+}	4	0.66	0.94
Ti^{4+}	6	0.61	0.99
Nb^{5+}	6	0.64	1.20
Ta^{5+}	6	0.64	1.20
W^{6+}	6	0.60	1.50

Table 3.5: Coordination index, ionic radii and field intensity for the different ions present in the samples considered in the present thesis.

This ratio shows the depolimerization of the glass network, since it measures the transformation of Te-$_{eq}$O$_{ax}$-Te linkages into NBO. Figure 3.12 shows the values of I_R calculated for TWR-series glasses as a function of the field intensity of the cations. Two different regions are observed. Cations such as Pb^{2+}, La^{3+}, and Bi^{3+}, which have field intensities lower than Te^{4+}, are related to high values of I_R. These cations act as network modifiers and lead to an increase of the NBO fraction. The second region corresponds to Ti^{4+}, Ta^{5+}, Nb^{5+}, and W^{6+}, which have field intensities larger than Te^{4+} and slightly higher values of I_R. In this case, I_R increases when f increases. This behavior can be understood in

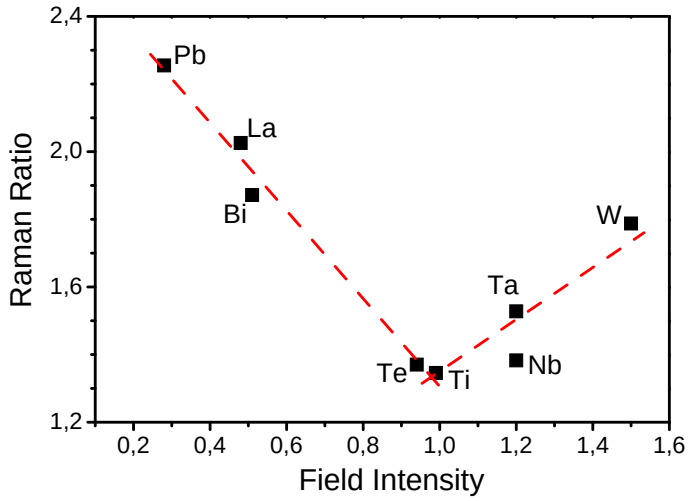

Figure 3.12: Ratio (I_R) between the intensities of the Raman peaks associated to NBO and the peak at 660 cm^{-1}. The dashed lines are guides for the eyes.

terms of these cations acting as network formers, breaking the Te-O-Te linkages to form highly polarized Te-O-R linkages instead of NBO. Since f is larger for these cations than for Te^{4+}, the vibrations of that kind of linkages are shifted to higher wavenumbers with respect to Te-O-Te linkages. As a consequence, I_R is higher in those cations than in Te^{4+} due to the lower number of Te-O-Te linkages and the contribution of Te-O-R vibrations to the band at 700 – 850 cm^{-1}. In particular, W^{6+} has the highest value of I_R among the cations acting as network modifiers. This agrees with the structure of tungsten-tellurite glasses having Te-O-Te, Te-O-W, and W-O-W linkages,[82, 116] where W^{6+} acts as conditional network former.

This behavior is further confirmed by the evolution of the band at 400 – 500 cm^{-1} (Fig. 3.11), related to a continuous glass network. In the case of network forming cations, that band is intense and is slightly affected by the change of the third component. However in the case of Pb, La and Bi modifiers, the band intensity decrease respect to binary glasses, proving their role as network modifiers.[108, 111]

Structure of TeO_2–WO_3–PbO glasses

TWPb-series glasses have been prepared in a wide range of compositions, with TeO_2 molar contents ranging from 85 to 50 mol% (Table 3.6). As it has been already discussed, such compositional differences must have an important effect on the structure of the glass network. In order to study the changes induced by increasing the molar content of WO_3 and PbO, we have compared the Raman spectra of samples in which the relative molar content of two of the oxides has been varied while maintaining constant the molar content of the third oxide. Figures 3.13, 3.14, and 3.15 show the Raman spectra in the range from 200 to 1200 cm^{-1} of glasses with a constant molar content of TeO_2, WO_3, and PbO respectively. The spectra were deconvoluted using the same peaks than in the case of the TW15 glass (Table 3.4), but the deconvolution and the peak assignment worsens as the molar contents of WO_3 and PbO increase, due to the increment in the amount of mixed T-O-W linkages and NBO oxygens. In that case, the glass network structure is far from that of TeO_2 glass shown in Fig. 3.7c.

Figure 3.13 shows the Raman spectra of glasses with a constant TeO_2 molar content of 80 mol% ($80TeO_2 \cdot (20 - x)WO_3 \cdot xPbO$, with x = 0 – 20). WO_3 is substituted mol by mol by PbO from the binary $80TeO_2 \cdot 20WO_3$ glass (TWPb2)

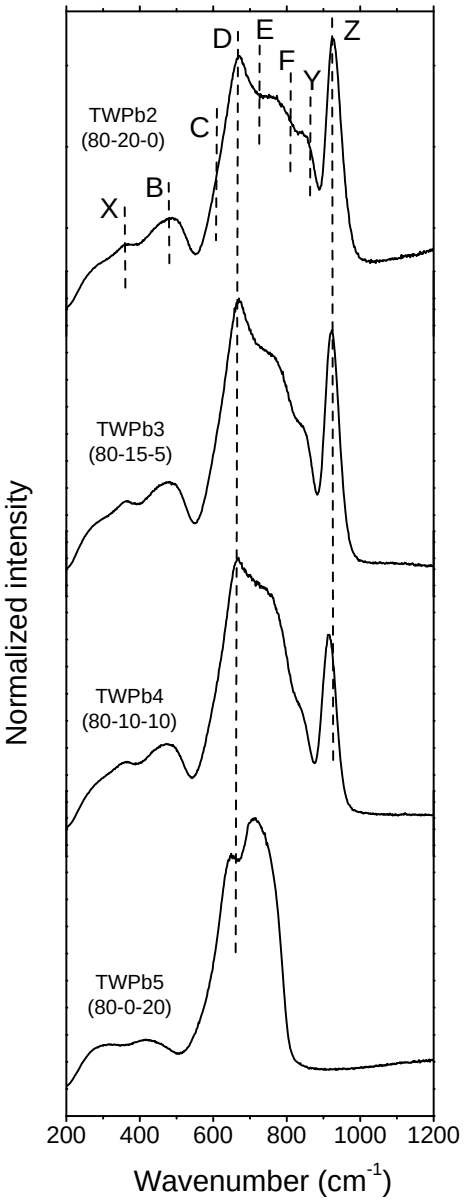

Figure 3.13: Raman spectra of glasses with composition $80TeO_2 \cdot (20 - x)WO_3 \cdot xPbO$. The dashed lines indicated the position of the deconvoluted peaks in the spectra of the TWPb2 binary glass.

Sample	Molar composition (mol%)
TWPb1	$85TeO_2 \cdot 15WO_3$
TWPb2	$80TeO_2 \cdot 20WO_3$
TWPb3	$80TeO_2 \cdot 15WO_3 \cdot 5PbO$
TWPb4	$80TeO_2 \cdot 10WO_3 \cdot 10PbO$
TWPb5	$80TeO_2 \cdot 20PbO$
TWPb6	$70TeO_2 \cdot 20WO_3 \cdot 10PbO$
TWPb7	$70TeO_2 \cdot 10WO_3 \cdot 20PbO$
TWPb8	$60TeO_2 \cdot 30WO_3 \cdot 10PbO$
TWPb9	$60TeO_2 \cdot 20WO_3 \cdot 20PbO$
TWPb10	$50TeO_2 \cdot 30WO_3 \cdot 20PbO$

Table 3.6: Molar composition of TWPb-series bulk glasses.

to the binary $80TeO_2 \cdot 20PbO$ glass (TWPb5). The peak position in the case of the deconvolution of the spectrum of TWPb2 glass is also shown. The intensities of bands Y and Z, related to $[WO_6]$ units, logically decrease when the WO_3 molar content decreases. Additionally, there is a shift in the positions of band Z, related to the vibration of W=O bond, and band D, related to $[TeO_4]$ tbp units, towards lower wavenumbers when the PbO molar content increases. These shifts are related to the lower field intensity of Pb^{2+} when compared to those of Te^{4+} and W^{6+} as it was discussed in the previous section. Simultaneously, the intensity of peak B at 490 cm^{-1}, related to a continuous glass network, and peak D decreases, whereas the intensity of peaks related to NBO (E and F) increases as PbO molar content increases. In particular, peak E assigned to NBO with strong interactions with the surrounding cations became the main band in the case of the TWPb5 glass. That trend indicates a cleavage of Te-O-Te linkages, decreasing the amount of $[TeO_4]$ tbp and breaking the glass network when increasing PbO molar content. Furthermore, when WO_3 is substituted mol by mol by PbO, the number of oxygen atoms in the glass network diminishes according to the ratio 3 to 1 and therefore the network closes, leading to a higher interaction of NBO and Te atoms that is evidenced by the increase of the intensity of band E.

In the case of glasses with a constant molar content of 20 mol% of WO_3 ($(80 - x)TeO_2 \cdot 20WO_3 \cdot xPbO$, with x = 0 – 20), TeO_2 is substituted mol by mol by PbO from the TWPb2 glass to the the $60TeO_2 \cdot 20WO_3 \cdot 20PbO$ glass (TWPb9). Their Raman spectra, shown in Figure 3.14, have a similar trend than glasses with constant TeO_2 molar content. Increasing the PbO molar content leads to shift the band Z towards lower wavenumbers, decrease the intensity of

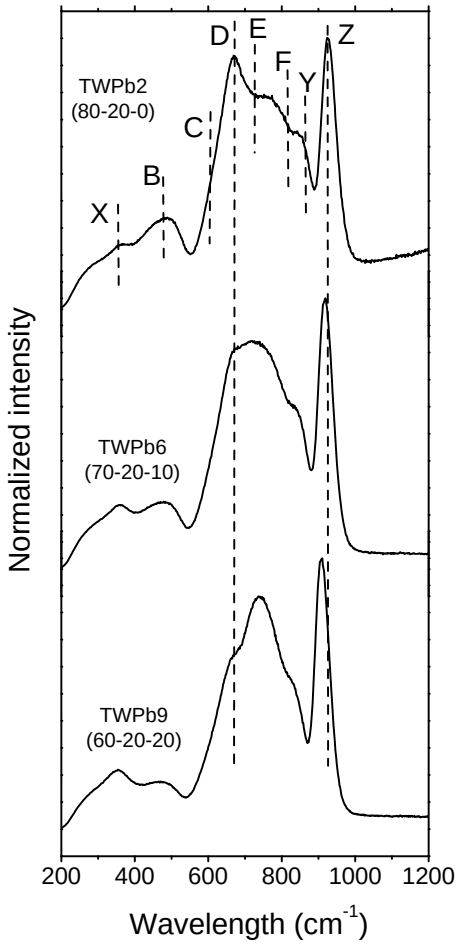

Figure 3.14: Raman spectra of glasses with composition $(80 - x)TeO_2 \cdot 20WO_3 \cdot xPbO$. The dashed lines indicated the position of the deconvoluted peaks in the spectra of the TWPb2 binary glass.

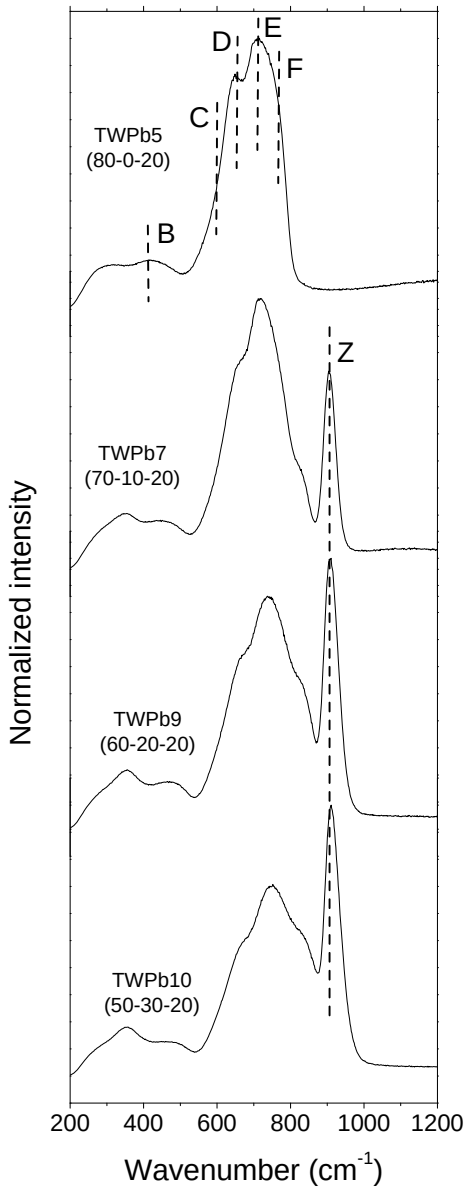

Figure 3.15: Raman spectra of glasses with composition $(80 - x)TeO_2 \cdot xWO_3 \cdot 20PbO$. The dashed lines indicated the position of the deconvoluted peaks in the spectra of the TWPb5 binary glass and peak Z in the TWPb7 glass.

the bands B and D, and increase of the intensity of the band E, which indicates the cleavage of Te-O-Te linkages and the increase of the amount of NBO. There is also a broad band at 300 – 400 cm^{-1} that increases its intensity when the PbO molar content increases. Since the WO_3 molar content is constant, this trend should not be related to the band X at 360 cm^{-1}, observed in TWPb2 glass. Instead, this low frequency band is related to vibrations of Pb-O bonds.[124, 125] The spectrum of sample TWPb9, having the highest PbO molar content, shows clear differences with respect to the spectra of glasses with higher TeO_2 molar contents. This spectrum has two main bands: one centered at 910 cm^{-1}, related to W=O bonds, and another centered around 740 cm^{-1}, which indicates that the network comprises Te-O-W linkages and a high amount of NBO.

Finally, Figure 3.15 shows the Raman spectra of glasses with composition $(80-x)TeO_2 \cdot xWO_3 \cdot 20PbO$ (x = 0 – 20). In these glasses the PbO molar content is constant and TeO_2 is substituted mol by mol by WO_3, from the binary $80TeO_2 \cdot 20PbO$ glass (TWPb5) to the $50TeO_2 \cdot 30WO_3 \cdot 20PbO$ glass (TWPb10). X, Y and Z peaks, assigned to vibrations of $[WO_6]$ units, do not exist obviously in the spectra of TWPb5 binary glass since it has no WO_3. However, these peaks are strongly enhanced in the other glasses as WO_3 molar content increases. There is also a slight shift of the band Z towards higher wavenumbers due to the higher field intensity of W^{3+} compared to Te^{4+} and the increasingly larger WO_3 molar content. Moreover, the intensity of the band D related to $[TeO_4]$ tbp diminishes, but in this case the breaking of Te-O-Te linkages is accompanied by the reduction in the amount of NBO, thus indicating the formation of a network based on Te-O-W linkages.

Thermal stability of TeO_2 - WO_3 - PbO glasses

Thermal properties of glasses, like thermal expansion coefficient, thermal conductivity, glass transition temperature, or crystallization temperature, are directly related to the structure of the glass since they depend on both the strength of interatomic bonds and the glass network connectivity.[59] In the present section, we study the glass transition, T_g, and crystallization temperatures, T_c, of samples belonging to the system TeO_2–WO_3–PbO using Differential Thermal Analysis (DTA). The values obtained are discussed in terms of the structural results obtained by Raman spectroscopy shown in the previous section.

Figure 3.16 shows the glass transition temperature as a function of the TeO_2

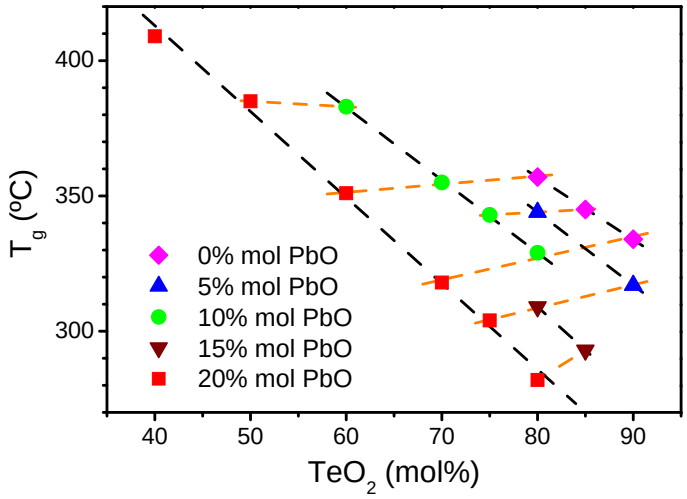

Figure 3.16: Glass transition temperature for TeO_2–WO_3–PbO glasses as a function of their molar composition. Dashed lines are guides for the eye indicating samples with (black dashed line) constant PbO molar content and (orange dashed line) constant WO_3 molar content.

molar content for all the prepared transparent glasses of the system TeO_2–WO_3–PbO (Fig. 3.4). T_g varies linearly with the molar fraction of each one of the three components. T_g strongly increases when the WO_3 molar content increases, from 282 °C for 0 mol% up to 409 °C for 40 mol%, and slightly decreases when TeO_2 is substituted mol by mol by PbO. The samples with the highest T_g values are those with the lowest molar contents of TeO_2 and PbO, *i.e.* with the highest WO_3 molar content, which indicates that WO_3 is the most contributing oxide to the increase of T_g.

Good thermal properties are also fundamental for the application of tellurite glasses in the fabrication of real photonic devices since their practical use demands avoiding any crystallization within the glass formation thermal range. The thermal stability of a glass can be evaluated in terms of the difference between the crystallization temperature, T_c, and the glass transition temperature. The wider the thermal stability range, the most favored is the glass forming process and, for example, the fabrication of optical fibres.[20, 118] The calculated thermal stability values for the glasses studied are shown in Figure 3.17a as a function of their WO_3 molar content. The highest values ($T_c - T_g > 160$ °C) are reached for glasses with WO_3 molar contents in the range from 10 to 30 mol%, which corresponds to the samples within the continuous line in the compositional

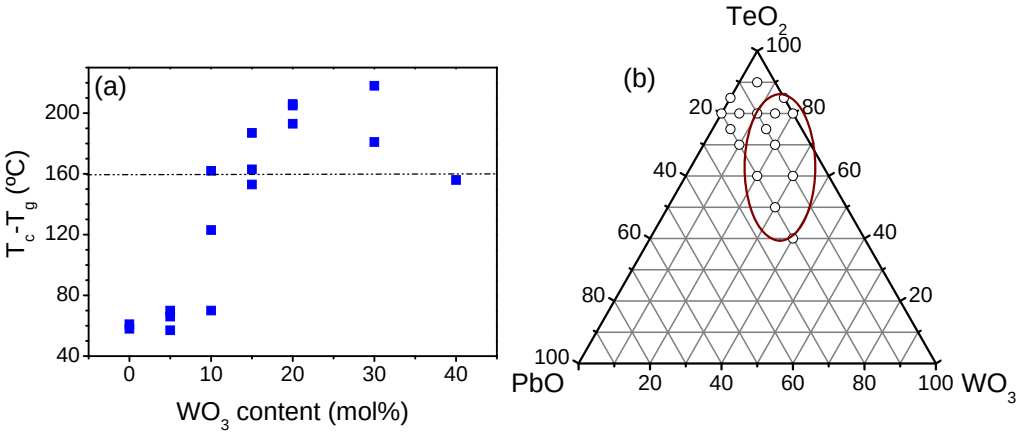

Figure 3.17: (a) Difference between the crystallization and the glass transition temperatures as a function of the WO_3 molar content. The dashed line corresponds to $T_c - T_g = 160$ °C. (b) Molar composition of glasses with the highest thermal stability (samples within the continuous line).

triangle (Fig. 3.17b).

The study of the glass transition and crystallization temperatures of TeO_2–WO_3–PbO glasses confirms the structural characterization deduced from Raman spectroscopy. In these glasses WO_3 acts as network former and thus their glass network mainly comprises [TeO_4] and [WO_6] structural units. W^{6+} and Te^{4+} cations form mixed linkages Te-O-W and W-O-W. Due to the high field intensity of W^{6+} cations, W-O bonds are stronger than Te-O bonds, thus increasing the glass transition temperature as the molar content of WO_3 is increased. On the contrary PbO acts as network modifier, weakening the structure and thus decreasing the glass transition temperature. Therefore, the addition of WO_3 allows producing TeO_2-based glasses with a good thermal stability in spite of a high molar content of a network modifier such as Pb^{2+}.

Summary of the structural results

The structure of TeO_2-based glasses has been studied with Raman spectroscopy. The tree basic structural units that form the tellurite glass network, [TeO_4] trigonal bipyramids, [$TeO_{3+\delta}$] polyhedra, and [TeO_3] trigonal pyramids, have been identified in a glass with a high TeO_2 molar content ($90TeO_2 \cdot 5TiO_2 \cdot 5Nb_2O_5$), and related to the different vibration modes observed in the Raman spectrum (Table 3.2). Then we have identified the same TeO_2 structural units in the case of glasses belonging to the system TeO_2–WO_3–R_xO_y (Fig. 3.11). In this case,

the spectra show bands associated to vibrations of WO_3 structural units, while the presence of a third R_xO_y oxide induces differences in the network structure with respect to that of binary glasses. Two different cases can be considered as a function of the field intensity of the third cation (Fig. 3.12). Those cations with low field intensities (Pb^{2+}, Bi^{3+}, and La^{3+}) have a higher amount of units containing NBO with respect to those cations with high field intensities (W^{6+}, Ti^{4+}, Nb^{5+}, and Ta^{5+}). In the first case, the cations act as network modifiers, breaking the Te-O-Te linkages which are forming the network, changing the coordination of the Te atom from 4 to 3, and increasing the fraction of NBO. In the second case, cations act as network formers through mixed T-O-R linkages. The Raman spectra of TeO_2–WO_3–PbO glasses (Figs. 3.13, 3.14, and 3.15) confirm these results, since Pb^{2+} has a very low field intensity and thus, the Raman spectra of glasses with large PbO molar content are characterized by a high intensity of peaks related to NBO.

The behavior of WO_3 as network former and PbO as network modifier is confirmed when studying the thermal stability of TeO_2–WO_3–PbO glasses. W^{6+} cations form strong W-O bonds in Te-O-W or W-O-W linkages. These linkages lead to a more stable glass network as suggested by the increase of the glass transition temperature and the thermal stability when increasing the WO_3 molar content. On the contrary, the substitution of TeO_2 or WO_3 mol by mol by PbO decreases the glass transition temperature, thus demonstrating the weakening of the network when adding PbO.

3.2.2 Optical properties of tellurite glasses

Composition and network structure are the basic parameters that determine the optical response of a glass. The results shown in the previous section clearly demonstrates that the presence and amount of the different cations affect the glass network and thus, it is expected an effect on the glass response. In the present section, the linear optical properties, namely transmission and linear refractive index, of samples belonging to the TeO_2–TiO_2–Nb_2O_5, TeO_2–WO_3–R_xO_y, and TeO_2–WO_3–PbO glass systems are characterized and discussed in terms of their composition and structure. The nonlinear optical properties of these glasses will be discussed in detail in Chapter 5.

Figure 3.18a shows the transmission spectrum of a $90TeO_2 \cdot 5TiO_2 \cdot 5Nb_2O_5$ glass, whereas the dispersion of the real part of the refractive index, n, determined

by ellipsometry, is shown in Fig. 3.18b. The transmission spectrum is characterized by a sharp UV absorption edge, as it is shown by the glass optical density, *OD* (inset in Fig. 3.18a), with an optical cutoff of 420 nm (2.95 eV). The position of that edge, inside the blue region of the visible part of the spectrum, gives tellurite glasses their typical orangish color. The value of the transmission in the transparency region is around 0.76. This value is related to the high reflectivity of the samples, which is associated to the large refractive index of the sample shown in Fig. 3.18a ($n > 2.1$). According to the transmission spectrum, tellurite glasses have no intrinsic absorptions in the range from their UV absorption edge up to wavelengths in the near-IR ($\sim$ 2500 nm) and thus, we can conclude that the imaginary part of the refractive index, κ, is negligible in the transparency region.

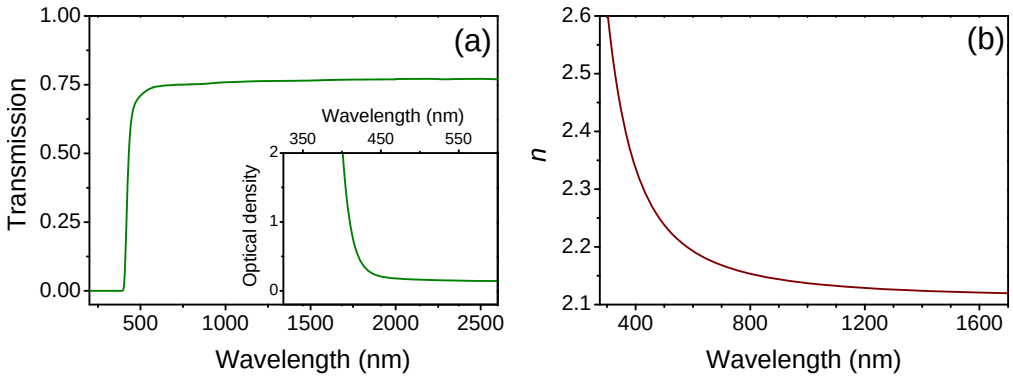

Figure 3.18: (a) Transmission spectrum and (b) real part of the refractive index of a $90TeO_2 \cdot 5TiO_2 \cdot 5Nb_2O_5$ glass. The inset in (a) shows the optical density of the sample in the vicinity of the UV absorption edge.

All the studied glasses show a similar trend in their linear optical properties: no intrinsic absorptions at wavelengths larger than that of the UV absorption edge and high refractive indexes in the transparency region ($n > 2$). However, the exact position of the absorption edge and value of the refractive index depends on the glass composition. In the next sections, we discuss the evolution of the optical properties of glasses belonging to the TWR- and TWPb-series.

TeO_2–WO_3–R_xO_y glasses

TWR-series glasses differ in their molar composition in only the 5 mol% of the R_xO_y oxide. However, this small variation has a non negligible effect in the posi-

tion of the UV absorption edge. Figure 3.19 shows the *OD* of three representative 1 mm thick TWR-series glasses. The TW15 binary glass ($85TeO_2 \cdot 15WO_3$) has its absorption edge red-shifted with respect to the others. The substitution of a 5 mol% of TeO_2 by a different oxide leads to blue-shift the absorption edge, except in the case of the $80TeO_2 \cdot 20WO_3$ binary glass (TW20), not shown in Fig. 3.19. The position of the optical cutoff of all the glasses belonging to TWR-series has been characterized through their optical cutoff values, shown in Table 3.7. The optical cutoff of the pure TeO_2 glass, deduced from data shown in ref. [126], is also shown for comparison.

Oxide glasses containing transition metal ions have shown semiconducting properties and, in the case of tellurite glasses, binary glasses such as TeO_2-V_2O_5 and TeO_2-WO_3 have high electrical conductivity values.[20] The increase of conductivity by adding these ions implies the decrease of the optical gap and thus, the absorption edge is red-shifted and the optical cutoff decreases with respect to pure TeO_2 glass. In particular, this red-shift in the position of the absorption edge has been previously observed in tungsten-tellurite glasses when substituting TeO_2 in binary glasses [127] or a modifier oxide(CaO) in ternary glasses [128] mol by mol by WO_3. Therefore, the addition of a third oxide in TWR-series glasses decreases the glass conductivity with respect to the binary glasses and thus, the UV absorption edge is blue-shifted (Fig. 3.19) and the optical cutoff increases (Table 3.7).

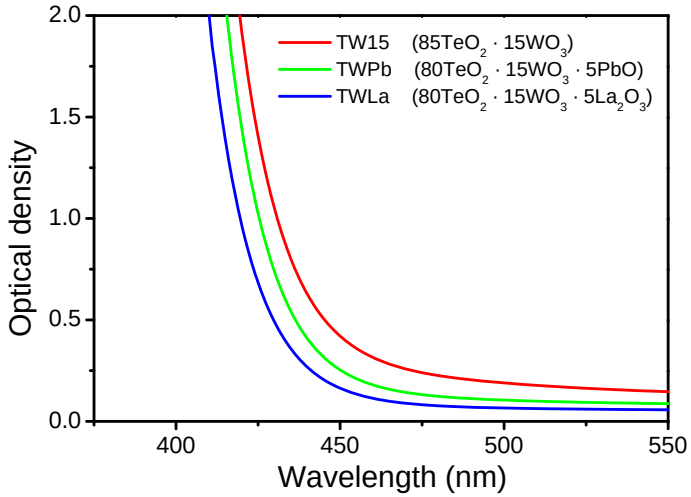

Figure 3.19: Optical density of three representative TWR-series glasses.

Sample	Optical cutoff ±0.01 eV	E_U ±0.001 eV	n at 1500 nm ±0.005
TW15	2.79	0.114	2.120
TW20	2.79	0.098	2.120
TWTi	2.80	0.097	2.120
TWNb	2.82	0.096	2.125
TWTa	2.85	0.097	2.110
TWLa	2.88	0.091	2.090
TWBi	2.85	0.107	2.140
TWPb	2.84	0.096	2.120
pure TeO_2	3.25	-	2.13

Table 3.7: Optical properties (optical cutoff, Urbach energy, and refractive index) of TWR-series glasses. The values of pure TeO_2 glass have been inferred from data shown in ref. [126].

The characterization of the UV absorption edge is completed with the determination of the Urbach energy, E_U, using the Urbach relation. The values obtained are included in Table 3.7. In the Urbach region, the optical absorption is due to transitions from the valence band to localized states in the band tails, or from these states to the conduction band.[20, 89] In fact, E_U measures the width of these band tails,[20] and thus, it estimates the density of localized states. All the values shown in Table 3.7 are close to 0.10 eV, thus indicating a similar density of states for all the glasses considered, and they are in good agreement with those reported in the bibliography for tungsten-tellurite glasses.[127]

Regarding the refractive index, the values of n at 1500 nm are shown in Table 3.7 The effect of the third oxide in the value of n is much smaller than in the case of the position of the absorption edge. In fact, the value of n is similar in all glasses ($n \simeq 2.12$) and similar to that reported in the literature for pure TeO_2 glass.[126] Only TWLa and TWBi glasses have clearly differentiated values of n with respect to the value of 2.12, larger in the case of TWBi (2.140) and smaller in the case of TWLa (2.090).

On the one hand, the enhancement of n when adding Bi_2O_3 is related to the high polarizability of that oxide.[16, 18] Bi^{3+} is a heavy metal cation with a very high ionic polarizability and, moreover, the presence of a lone electron pair in the valence shell of the Bi^{3+} cation also increases the polarizability of the oxygen ions in the Bi_2O_3 oxide.[98] On the other hand, TWLa has the lower n value. This is related to a reduced oxide polarizability [98, 129] in this case, as suggested by the high optical cutoff of TWLa glass that is related to a large optical gap.

TeO_2–WO_3–PbO glasses

In the case of the TWPb-series, the WO_3 and PbO molar contents have been increased up to 30 and 20 mol% respectively, which has an important effect on the optical response of these glasses. As in the previous case, the values of the optical cutoff, Urbach energy and refractive index at 1500 nm of glasses belonging to this series are included in Table 3.8.

Figure 3.20a shows the *OD* of representative 1 mm thick TWPb-series glasses. The absorption edge of glass TWPb5, with a composition of $80TeO_2 \cdot 20PbO$, is clearly blue-shifted with respect to the others, which have at least 10 mol% of WO_3. In order to study the evolution of the position of the absorption edge with the glass composition, the values of the optical cutoff of the TWPb-series glasses,included in Table 3.8, have been plotted as a function of the WO_3 molar content (Fig. 3.20b).

The experimental measured optical cutoff values are always smaller than that of pure TeO_2 glass [126] and they clearly decrease with the molar content of WO_3, from 2.97 eV in the case of the sample without WO_3 down to 2.74 – 2.75 eV in the case of the samples containing 30 mol% of WO_3. Moreover, the substitution of TeO_2 by PbO in glasses with a constant molar content of WO_3 below 20 mol% increases the values of the optical cutoff. These results are in very good agreement with the previous discussion regarding the semiconducting behavior of the tungsten-tellurite glasses and show that the key parameter in the position of the UV absorption edge is the WO_3 molar content: the higher the

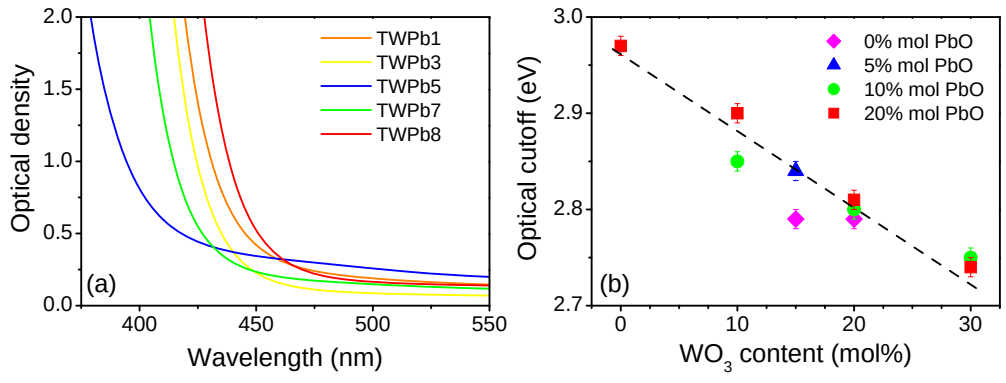

Figure 3.20: (a) Optical density and (b) optical cutoff of TWPb-series glasses. The dashed line is a guide for the eyes.

Sample	Optical cutoff ±0.01 eV	E_U ±0.001 eV	n at 1500 nm ±0.005
TWPb1	2.79	0.114	2.120
TWPb2	2.79	0.098	2.120
TWPb3	2.84	0.096	2.120
TWPb4	2.85	0.107	2.130
TWPb5	2.97	0.155	2.125
TWPb6	2.80	0.095	2.130
TWPb7	2.90	0.105	2.135
TWPb8	2.75	0.091	2.140
TWPb9	2.81	0.122	2.150
TWPb10	2.74	0.103	2.150
pure TeO_2	3.25	-	2.13

Table 3.8: Optical properties of TWPb-series glasses. The values of pure TeO_2 glass have been inferred from data shown in ref. [126].

WO_3 molar content, the higher is the electrical conductivity of the glass and the more red-shifted is the absorption edge.

As in the previous section, the absorption coefficient of the samples has been fitted to the Urbach relation to obtain E_U, which is shown in Table 3.8. E_U is in the range 0.10 – 0.12 eV in all cases except for the sample TWPb5 (0.155 eV). This fact is related again to the composition and structure of the glasses,

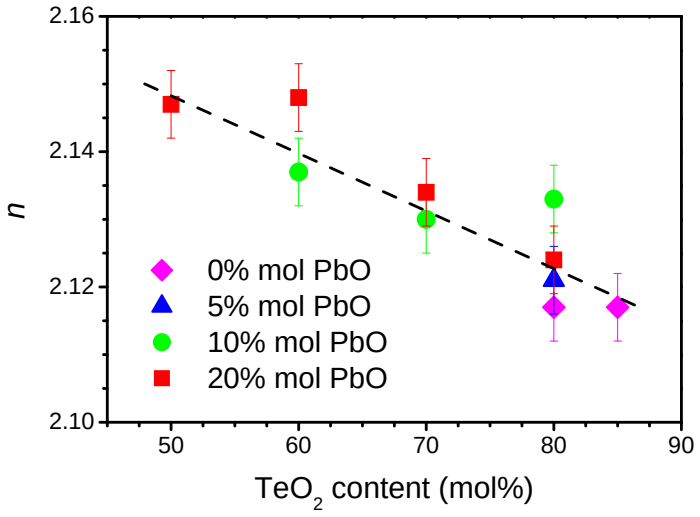

Figure 3.21: Refractive index of TWPb-series glasses as a function of the TeO_2 molar content. The dashed line is a guide for the eyes.

since TWPb5 is the only binary glass without WO_3. The Raman spectrum of that glass, shown in Figs. 3.13 and 3.15, suggested a highly disordered network. This is related to a higher density of localized states in the gap and thus to a higher value of E_U. On the contrary, in the case of glasses containing WO_3, the formation of Te-O-W linkages prevents the glass network from breaking and, therefore, E_U is similar in all the tungsten-tellurite glasses.

Finally, the values of the refractive index at 1500 nm of TWPb-series glasses are shown in Table 3.8 and Figure 3.21 as a function of the TeO_2 content. The substitution of WO_3 or PbO by TeO_2 decreases n from 2.150 for glasses with a TeO_2 molar content of 50 – 60 mol% down to 2.120 for the glass with the higher TeO_2 molar content (TWPb1). This behavior is the expected due to the high polarizability of both the transition, W^{6+}, and the heavy metal, Pb^{2+}, cations.

3.3 Summary and conclusions

The present chapter has focussed on the characterization of the structure and the optical properties of TeO_2-based bulk glasses in a wide range of compositions. Raman spectroscopy has been used to characterize the structure of the considered bulk glasses. The network of TeO_2-based glasses is formed by structural units with different coordinations of the Te atom, such as [TeO_4] tbp, [$TeO_{3+\delta}$] polyhedra, and [TeO_3] tp.

In the case of glasses belonging to the system TeO_2–WO_3–R_xO_y, we have shown that the addition of different oxides such as TM oxides (TiO_2, Nb_2O_5, Ta_2O_5, WO_3, and Nb_2O_5) and HM oxides (Bi_2O_3 and PbO) breaks the Te-O-Te linkages. On the one hand, when the oxide contains a cation R with a field intensity higher than that of Te^{4+}, new Te-O-R mixed linkages are formed, the connectivity of the network is maintained, and thus the oxide acts as network former. On the other hand, cations with field intensities lower than that of Te^{4+} induce the transformation of [TeO_4] tbp units into [TeO_3] tp units, characterized by the presence of NBO, thus breaking the network and acting as modifiers.

Such evolution is clearly shown in the case of the TeO_2–WO_3–PbO system, for which glasses with very different molar contents of TeO_2, WO_3, and PbO have been prepared. WO_3 and PbO have opposite roles in the glass network. On the one hand, W^{6+} in WO_3 has a very high field intensity and thus WO_3 acts as network former. In glasses with a high WO_3 molar content, Te-O-Te linkages are broken to form strong Te-O-W linkages. On the other hand, Pb^{2+} has very

low field intensity and thus PbO acts as network modifier, leading to a significant increase of the NBO fraction as shown by the Raman spectra.

The results regarding the evolution of the structure have been confirmed by the analysis of the thermal stability of TeO_2–WO_3–PbO glasses. The glass transition temperature varies linearly with the molar content of the different oxides, and it has been shown to increase with the WO_3 molar content due to the presence of strong W-O bonds that form Te-O-W linkages. Moreover, the thermal stability, defined as the difference between the crystallization temperature and the glass transition temperature, is higher in glasses with a 10 – 30 mol% of WO_3. Therefore, from the point of view of the thermal stability, tungsten-tellurite glasses are promising materials for the development of optical devices due to the strong linkages comprising their glass network.

The above mentioned compositional and structural changes have an impact on the optical properties of the glasses. Bulk glasses have high refractive indexes ($n > 2$ at 1500 nm) and show no intrinsic absorptions in their transparency region. The position of the UV absorption edge depends on the glass composition in both TeO_2–WO_3–R_xO_y and TeO_2–WO_3–PbO systems. Binary TeO_2–WO_3 glasses or ternary glasses with a high WO_3 molar content have their absorption edge red-shifted with respect to the other glasses. This behavior has been correlated to the high electrical conductivity reported on the literature for tungsten-tellurite glasses, while the addition of other oxides seems to reduce the conductivity and thus their UV absorption edge is shifted towards higher energies. The absorption coefficient in the UV absorption edge has been described according to the Urbach relation. Urbach energies, related to the density of localized states in the gap, are similar in all cases ($E_U = 0.10 - 0.11$ eV) except in the case of the binary $80TeO_2 \cdot 20PbO$ glass ($E_U = 0.155$ eV), which is the glass with the more distorted glass network according to the structural analysis. Finally, all glasses show similar refractive indexes (n = 2.09 – 2.15 at 1500 nm). The higher values of n are obtained in those glasses containing highly polarizable heavy metal cations, such as Bi^{3+} or Pb^{2+}.

In conclusion, we have established the correlation between composition, structure, and optical properties of TeO_2-based bulk glasses. Since in the case of bulk glasses the preparation process is well established, we do not expect significant effects from it on the final structure of the glasses. However, in the case of film glasses, the synthesis process can deeply affect both the composition and structure of the glass network due to uncertainties associated with the deposition

procedure. Therefore, in the next chapter we will define the optimum deposition conditions and thereafter we will study the composition, structure, and linear optical response of pulsed laser deposited tellurite thin film glasses, based on the results obtained for bulk glasses.

Chapter 4

TeO_2-based thin film glasses

In this chapter, we determine the optimum conditions for the pulsed laser deposition of tellurite thin film glasses. In particular, we study the effect of the laser energy density and the oxygen pressure on the composition and structure of films deposited from a transparent $90TeO_2 \cdot 5TiO_2 \cdot 5Nb_2O_5$ bulk glass, as they determine the optical response of the films. The results obtained are discussed in terms of the expansion dynamics of the laser generated plasma, since the kinetic energy and the spatial distribution of the ejected species are strongly correlated to the properties of the films. Films deposited at low laser energy densities or low oxygen pressures show strong compositional differences and glass network structures far from that of bulk glasses.

It is shown that only a narrow range of experimental parameters allows producing transparent TeO_2-based film glasses with a lower refractive index than that of bulk glasses. Finally, these optimum conditions have been proven to be valid to deposit transparent thick films from glasses belonging to the systems TeO_2–TiO_2–Nb_2O_5, TeO_2–WO_3–R_xO_y, and TeO_2–WO_3–PbO. Their linear optical properties, namely the refractive index and the optical gap, have beencompared in all cases to those of bulk glasses and discussed in terms of film composition and structure.

4.1 Experimental parameters of PLD

The key experimental parameters in PLD are those related to the laser (wavelength, pulse length and energy density), deposition geometry (position and distance target-substrate), temperature of the substrate, and pressure and nature of the background gas inside the deposition chamber.[43] In this thesis, films were deposited using an ArF excimer laser (λ = 193 nm). This type of laser has proven to be highly adequate for the deposition of smooth and good optical quality films by PLD.[130] Most materials show strong absorption in the near UV while excimer lasers are capable of delivering high energy densities (> 1 J cm^{-2}) at these wavelengths, making possible to ablate practically any material but wide band-gap dielectrics.

The deposition geometry described in Chapter 2 affects the deposition rate and the uniformity of the film obtained,[60] while the substrate temperature is known to favor the formation of crystalline films.[131] However, the most important parameters in the case of amorphous materials such as glasses, are the laser energy density and the background gas pressure, since the plasma expansion dynamics is directly related to these parameters.[43] In the present thesis, the film properties have been tailored through carefully controlling the laser energy density on the surface of the target and the pressure of oxygen gas in the chamber, while the distance target-substrate was fixed and the substrate was maintained at room temperature.

As it is described in Chapter 2, the laser generated plasma expands perpendicularly from the target surface. Initially, the plasma is confined to a small volume near the target. In vacuum, the plasma expands indefinitely due to the high density gradient between the plasma and the surrounding region. In the case of the presence of a background gas with pressures higher than a few Pa, the plasma expansion is severely affected.[65] Scattering of the plasma species by the background gas atoms or molecules reduces the velocity of the species, and affects the amount and angular distribution of material reaching the substrate and thus, the final characteristics of the deposited film. Now the plasma is confined in a finite size of a few cm with well defined boundaries.[61, 132] To illustrate this point, images of the plasma expansion both in vacuum and in a reduced gas pressure are shown in Figure 4.1.

Three different stages of propagation can be distinguished during the plasma expansion in a background gas [65]:

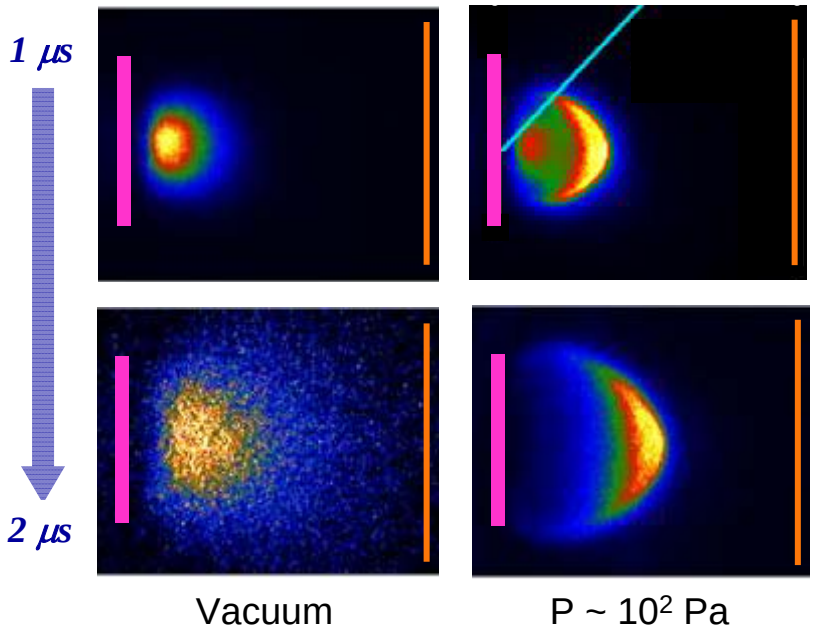

Figure 4.1: Images of the plasma expansion in vacuum and in a background gas atmosphere (P $\sim 10^2$ Pa) at two different delay times with respect to the laser pulse. The light blue straight line in the upper right image indicates the trajectory of position of the laser pulse. Images taken from ref. [133].

- Initially, just close to the target surface, the density of the ablated material is much higher than that of the surrounding gas and the initial expansion is unaffected by the gaseous background.[134] Then, the expansion dynamics is similar to those in vacuum.

- As the plasma expands, its density decreases and it becomes comparable to the density of the surrounding gas and thus, the effects of the background gas in the plasma expansion start to be significant. The collisional interaction between the plasma species and the gas atoms or molecules causes the modification of the angular distribution of species in the plasma and reduces their velocity. Depending on the gas pressure, two different regimes of interaction can be distinguished: If the gas pressure is below 10 Pa, the plasma species are scattered by the gas atoms while for pressures higher than 10 Pa, the plasma dynamics is similar to those of a fluid propagating in a gas.[135] In the latter case, the expansion of the plasma has success-

fully been described according to the shock wave model, in which the plasma sweeps up and drive the gas at a supersonic velocity as it propagates.[134]

- Finally, the plasma species move randomly by diffusion once they have lost their kinetic energy due to the interaction with the surrounding gas. The distance from the target at which the ablated material has lost all its kinetic energy is generally known as plasma or plume length (L_p). Dyer *et al.* [134] evaluated L_p in the frame of the shock wave model as a function of the laser energy density (E) and the gas pressure (P):

$$L_p = f(A, V, \gamma) \left(\frac{\mathrm{E}}{\mathrm{P}}\right)^{1/3\gamma} \tag{4.1}$$

where A is a geometrical factor related to the laser spot geometry, V is the initial volume of the plasma, and γ is the ratio of specific heats (C_p/C_v).

The three expansion regimes are mostly determined by the amount of ablated material and the kinetic energy of the plasma species, which are related to the laser energy density and the pressure of the background gas. Moreover, the target-substrate distance and its relation with L_p is critical for the film deposition since its composition and properties are determined by the expansion regime in which the films are deposited.[43, 70] For example, in the case of oxides the best films have been obtained when L_p is comparable to the distance target-substrate.[136]

In addition to the kinetic effects associated with the presence of a background gas, its reactive or inert character must be taken into account. In the first case, the atmosphere may also affect the composition of the film through chemical reactions between the ablated species and the surrounding gas molecules.[60] In fact, most of the complex oxides deposited by PLD can be only synthesized with the right composition when deposited in an oxidizing atmosphere, usually O_2,[44] as it has been widely investigated in the case of high temperature superconducting films [63, 137, 138], films for optical applications, such as $LiNbO_3$ [139], $BaTiO_3$,[136] or oxide glasses.[45, 46]

4.2 PLD of TeO_2-based thin film glasses

Heavy metal oxide and tellurite film glasses have been previously synthesized by PLD only in a narrow range of laser energy densities, in the order of a few J cm^{-2}, and oxygen pressures, in the range between 1 and 10 Pa,[36, 50, 51] as it

was described in Chapter 1. Since the exact deposition conditions depend on the actual geometry of the PLD setup, we have deposited tellurite thin film glasses at different oxygen pressures (P_{O_2}) and laser energy densities (E) from a transparent $90TeO_2 \cdot 5TiO_2 \cdot 5Nb_2O_5$ bulk glass in order to exactly define the optimum deposition conditions. The ranges of P_{O_2} and E studied have been chosen according to the optimum conditions determined previously for heavy metal oxide thin film glasses,[50, 51] while the distance between target and substrate was fixed (D = 3 cm). Two different experimental series of films were deposited as a function of the laser energy density (E-series) and the oxygen pressure (P_{O_2}-series). E-series films were deposited at a fixed P_{O_2} of 5 Pa using E ranging from 0.75 to 1.5 J cm^{-2}, while the P_{O_2}-series is composed by films deposited at a fixed E of 1.5 J cm^{-2} and in a P_{O_2} range from 3 to 11 Pa. The detailed deposition conditions are summarized in Table 4.1.

Sample	Energy density ± 0.15 J cm^{-2}	Oxygen pressure ± 0.5 Pa
E075P05	0.75	5.0
E100P05	1.00	5.0
E125P05	1.25	5.0
E150P03	1.50	3.0
E150P05	1.50	5.0
E150P08	1.50	8.0
E150P11	1.50	11.0

Table 4.1: Summary of film glasses and the experimental parameters used for film deposition.

4.2.1 Composition and structure of film glasses

Film composition has been determined by ion beam techniques (RBS and NRA) and XPS. Figure 4.2 shows the composition of E- and P_{O_2}-series films relative to the total cation content, [X], that is defined as:

$$[\mathrm{X}] = \frac{N_\mathrm{X}}{N_\mathrm{Te} + N_\mathrm{Ti} + N_\mathrm{Nb}} \tag{4.2}$$

with X = Te, Ti, Nb, or O and N_X is the number of atoms per unit of area of the element X determined experimentally. A very good agreement between the results obtained from the two techniques is observed. The cation content in the films is similar to that of the bulk glass for the whole E (Fig. 4.2a) and P_{O_2} (Fig. 4.2b) ranges. However, the oxygen content is strongly affected by the deposition

conditions. Films deposited at low E (Fig. 4.2a) show an oxygen deficiency that is close to 20% for the film deposited at the lowest E (0.75 J cm^{-2}). As E increases, the oxygen content increases to reach a value similar to that of the bulk glass for E = 1.5 J cm^{-2}. In the case P_{O_2}-series (Fig. 4.2b), the oxygen content increases with P_{O_2}, from values equal to that of the bulk glass up to an oxygen excess higher than 10% at $P_{O_2} \geq 8$ Pa.

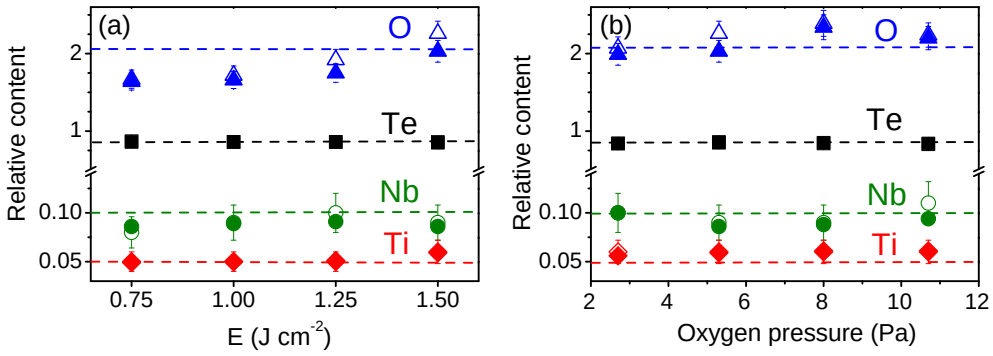

Figure 4.2: Relative atomic composition for (a) E- and (b) P_{O_2}-series films determined from (full symbols) RBS and NRA and (open symbols) XPS. The dashed lines correspond to the nominal relative atomic composition of the bulk glass.

The variation of the oxygen content in the films observed in both series clearly indicates a modification of the stoichiometry of the films with respect to the nominal composition of the bulk glass, which should be related to changes in the oxidation state of cations. XPS has been used to determine these changes. Figure 4.3 shows the Te $3d$ core-level spectrum for the bulk glass (Fig. 4.3a), and two representative films: E150P08 (Fig. 4.3b) and E075P05 (Fig. 4.3c). Film E150P08, which was deposited at the highest E (1.5 J cm^{-2}) and in a high P_{O_2} (8 Pa), shows a similar spectrum than that of the bulk glass with two peaks at binding energies (BE) of 576 and 586 eV, which correspond to the Te^{4+} $3d_{5/2}$ and $3d_{3/2}$ levels. However, film E075P05, which was deposited at the lowest E (0.75 J cm^{-2}) and low P_{O_2} (5 Pa), has two additional peaks at BE of 573 and 583 eV that are related to Te^0 $3d$ level. This indicates the presence of tellurium atoms in a reduced oxidation state. Figure 4.4 shows the percentage of reduced Te atoms respect to the total number of Te atoms, X_{Te^0} for all the films of E-

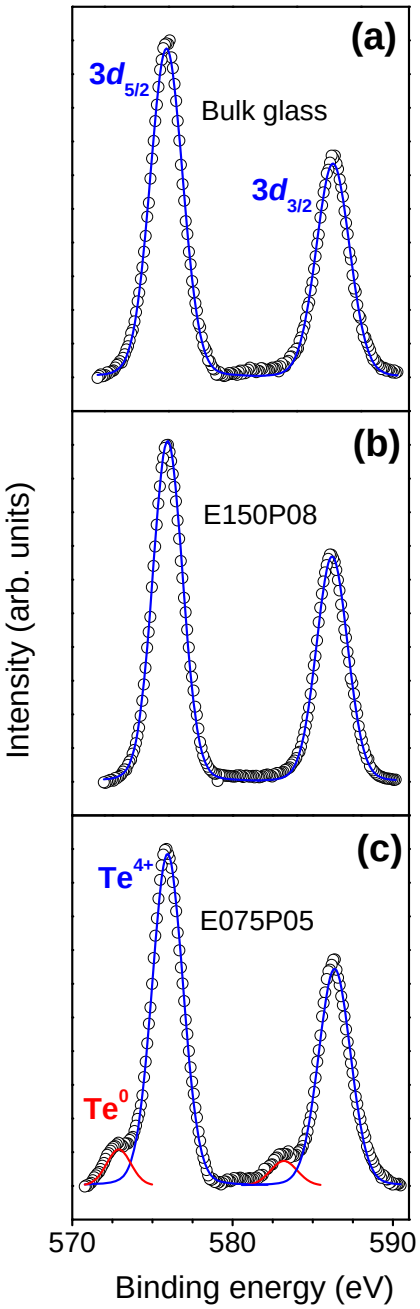

Figure 4.3: Te $3d$ core level XPS spectra measured for (a) the $90TeO_2 \cdot 5TiO_2 \cdot 5Nb_2O_5$ bulk glass and two films deposited at (b) E = 1.5 J cm^{-2} and P = 8 Pa (E150P08) and (c) E = 0.75 J cm^{-2} and P = 5 Pa (E075P05). The blue and red lines correspond to Te^{4+} and Te^0, respectively.

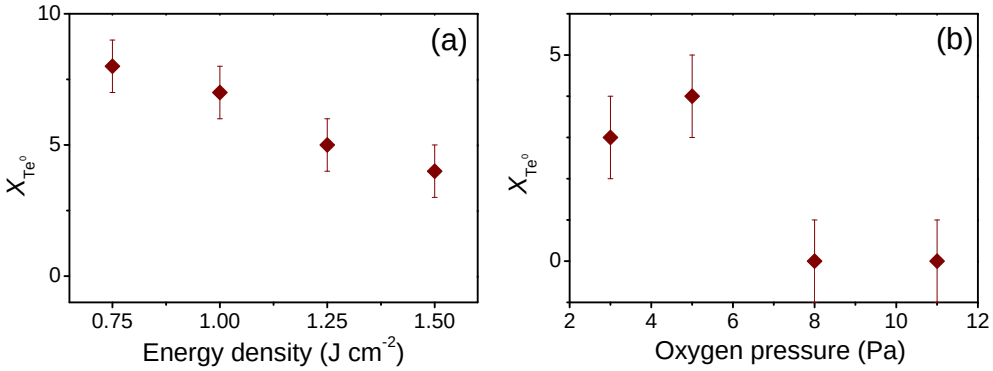

Figure 4.4: Percentage of reduced Te atoms (Te^0) respect to the total number of Te atoms and ions determined for the films deposited in the (a) E- and (b) P_{O_2}-series.

and P_{O_2}-series, calculated as:

$$X_{Te^0} = 100 \frac{N_{Te^0}}{N_{Te^0} + N_{Te^{4+}}} \tag{4.3}$$

where N_{Te^0} and $N_{Te^{4+}}$ are the the number of Te^0 atoms and Te^{4+} ions respectively. In the case of films belonging to the E-series, the content of Te^0 is 8% at E = 0.75 J cm^{-2} and decreases as E increases to reach a value of 4% at E = 1.5 J cm^{-2}. In the case of P_{O_2}-series, films deposited at $P_{O_2} \leq 5$ Pa have a content of Te^0 $\sim$ 4%, while films deposited at $P_{O_2} \geq 8$ Pa have no Te^0. The XPS spectra of levels $3d_{5/2}$ and $3d_{3/2}$ of Nb and $3p_{3/2}$ and $3p_{1/2}$ of Ti have been also studied, although they are not shown here. The BE of both cations are the same in the films and in the bulk glass, which indicates that Ti and Nb remain in the same oxidation state (Ti^{4+} and Nb^{5+}) than in the bulk glasses.

As it has been shown in Chapter 3, the role of oxygen in the formation of the vitreous network of oxide glasses is fundamental. Therefore the compositional changes observed in the films, namely the oxygen deficiency or excess, and the presence of reduced Te, must have a relevant effect in the structure of tellurite film glasses. This has been investigated by means of Raman spectroscopy. Figure 4.5 shows the reduced Raman spectra measured for bulk and film glasses in the region between 550 and 900 cm^{-1} for the E- (Fig. 4.5a) and P_{O_2}-series (Fig. 4.5b) films. The spectrum of the bulk glass, which has been previously discussed in Chapter 3, is included in the Figure as a guide. It shows two intense bands at 600 – 700 cm^{-1} and 700 – 800 cm^{-1}, which have been deconvoluted in four Gaussian

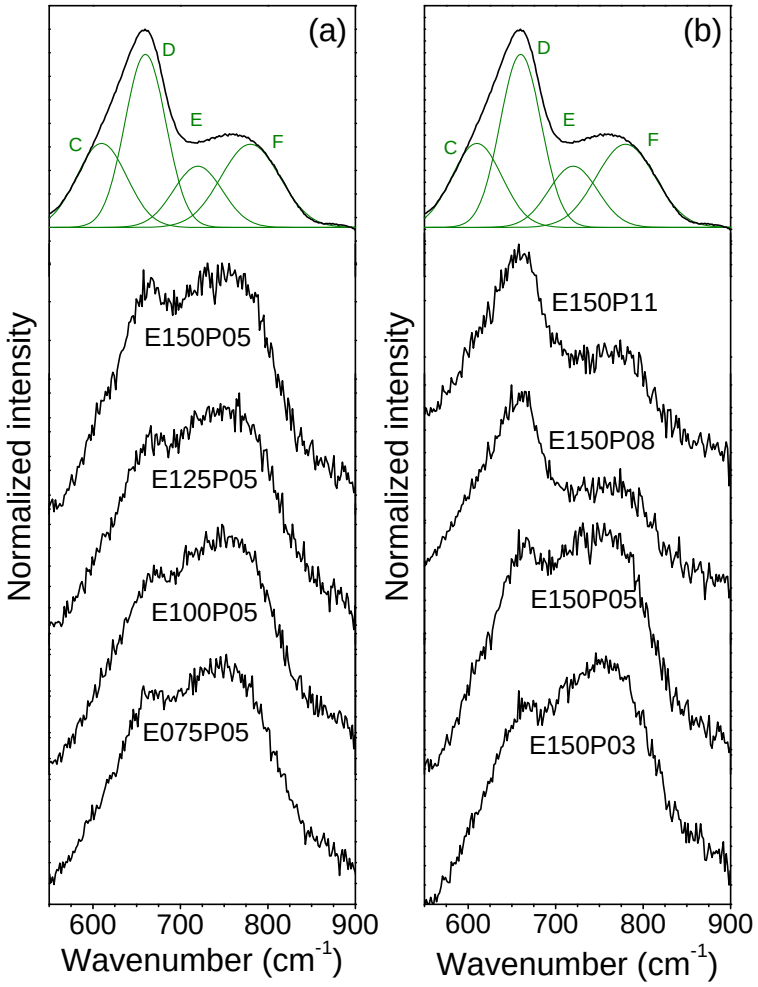

Figure 4.5: Raman spectra corresponding to (a) E- and (b) P_{O_2}-series films. The spectrum of the bulk glass and its deconvolution in Gaussian peaks are also shown for comparison.

peaks at 610, 660, 720, 780 cm^{-1}, as it was shown in Fig. 3.8 and Table 3.2. These peaks are related to the continuous network of [TeO_4] trigonal bipyramids (peaks C at 610 and D at 660 cm^{-1}) and to the vibration of nonbridging oxygens (NBO) associated to the [$TeO_{\delta+1}$] and [TeO_3] units (peaks E at 720 and F at 780 cm^{-1}).

Raman spectra of the E-series films (Fig. 4.5a) show that the peaks related to NBO are more intense than peak D in all cases as opposite to what it is observed for the case of bulk glass. In the case of P_{O_2}-series the behavior is more complex. Films at low P_{O_2} ($\leq$ 5 Pa) have similar spectra than E-series films. However, the relative intensities of peaks F and E decrease when increasing P_{O_2} and for film glasses deposited at $P_{O_2} \geq 8$ Pa, Raman spectra are similar to that of the bulk glass.

According to the peak assignment made in Chapter 3, we can qualitatively estimate the fraction of NBO in the film glasses from the ratio of the intensities of the deconvoluted peaks related to NBO (peaks E and F at 720 and 780 cm^{-1} respectively) and the deconvoluted peak D at 660 cm^{-1}, related to the [TeO_4] tbp continuous network [110, 122, 123]:

$$I_R = \frac{I_E + I_F}{I_D} \tag{4.4}$$

The ratio I_R is shown in Figure 4.6 for both the E- (Fig. 4.6a) and P_{O_2}-series (Fig. 4.6b). Films deposited at different E and low P_{O_2} show similar ratios,

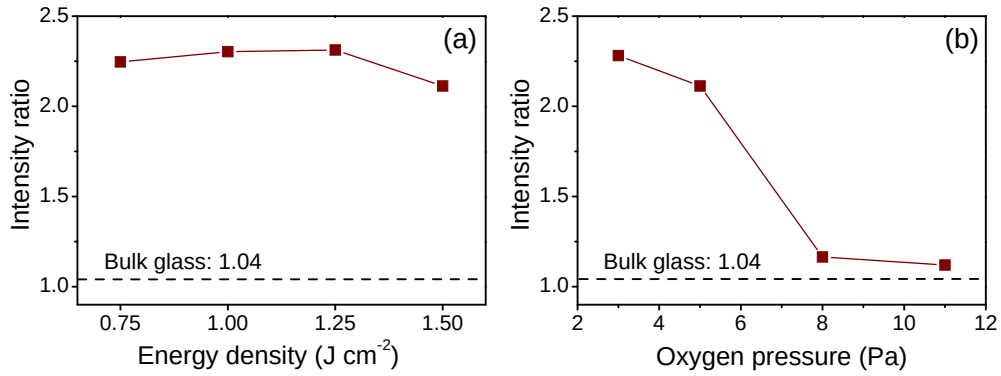

Figure 4.6: Ratio between the intensities of the Raman peaks associated to NBO and the peak at 660 cm^{-1} for (a) E- and (b) P_{O_2}-series film glasses. The dashed lines show the ratio measured for the bulk glass.

with I_R values that double that of the bulk glass. Only the film deposited at the highest E (1.5 J cm^{-2}) shows a slight decrease of I_R. On the contrary, I_R strongly decreases when increasing P_{O_2}, becoming similar to that of the bulk glass at P_{O_2} $\geq$ 8 Pa.

4.2.2 Linear optical properties of film glasses

The compositional and structural modifications observed in the films when changing E and P_{O_2}, namely an oxygen deficiency accompanied by the presence of reduced Te atoms, an excess of NBO in the glass network, and structures far from that of the bulk glass in the case of films deposited at low E or P_{O_2}, must affect the optical response of the films. In order to investigate this fact we have determined the complex refractive index ($\hat{n} = n + i\kappa$) of E- and P_{O_2}-series films by spectroscopic ellipsometry.

The values of n and κ at 1500 nm of E- and P_{O_2}-series films are shown in Figures 4.7 and 4.8 respectively. The film deposited at the lowest E (0.75 J cm^{-2}) has a n value that is a 13% higher than that of the bulk glass, 2.120 (Fig. 4.7a). As E increases, n decreases down to a value similar to that of the bulk at the highest E (1.5 J cm^{-2}). In the case of P_{O_2}-series films (Fig. 4.7b), n also decreases down to values that are a 5% lower than that of the bulk glass when P_{O_2} increases. This trend is similar in the case of the imaginary part of the refractive index: κ decreases when either E (Fig. 4.8a) or P_{O_2} (Fig. 4.8b) increases to reach values below our experimental resolution limit (10^{-4}) for the

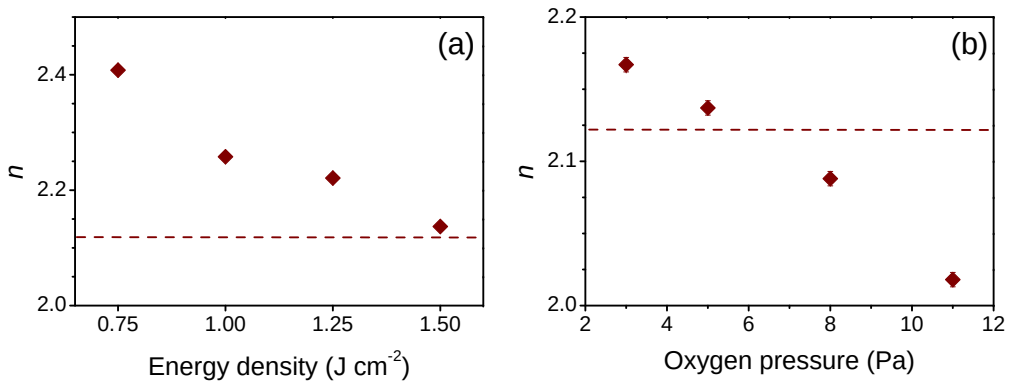

Figure 4.7: Values of the real part of the refractive index of (a) E- and (b) P_{O_2}-series films. The dashed lines correspond to the n value of the bulk glass.

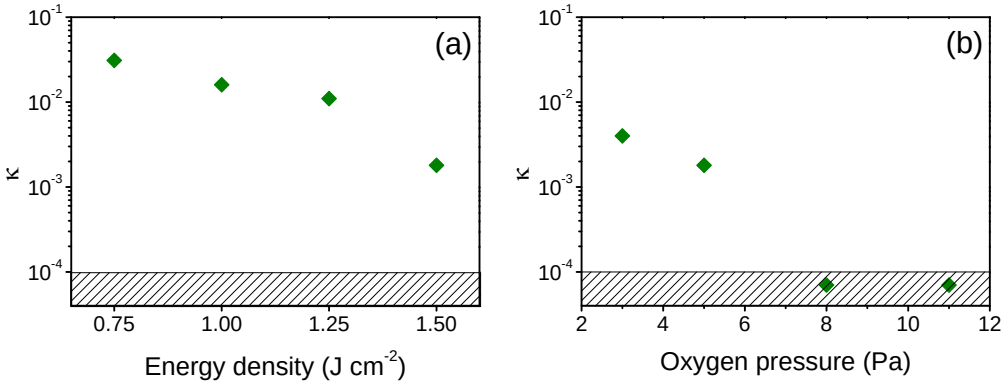

Figure 4.8: Values of the imaginary part of the refractive index of (a) E- and (b) P_{O_2}-series films. The experimental detection limit for κ is 10^{-4} (striped region in the graphs) and thus values below that limit cannot be measured.

films at E = 1.5 J cm^{-2} and $P_{O_2} \geq 8$ Pa.

4.2.3 Influence of the plasma dynamics on the film composition and structure

The experimental results clearly show that small variations of either the laser energy density or the oxygen pressure strongly affect the properties of the films, as they have significative compositional, structural, and optical differences with respect to the bulk glass.

The dependence of the composition of the films with the experimental parameters may suggest that the fundamental one is the laser energy density since those films deposited at low E are oxygen deficient (Fig. 4.2a) and they show a non negligible fraction of reduced Te atoms. As E increases, the film oxygen content increases, leading to an oxygen excess at the highest E while the Te^0 content decreases by a factor of two (Fig. 4.4a). The decrease of the fraction of Te^0 atoms is logically accompanied by a higher amount of oxygen atoms in the film, as it is shown in Fig. 4.2a.

The deposition of oxygen deficient films or the presence of reduced cations is not uncommon in films deposited by PLD. Previous results have shown that high-temperature superconductor oxides are oxygen deficient when deposited at low oxidizing gas pressures or low substrate temperatures.[137, 138] In this case, the incorporation of oxygen from the atmosphere to the deposited film is fundamen-

tal to reach the right stoichiometry. This incorporation can take place through chemical reactions during the plasma expansion or processes taking place at the growing film surface. Since in our case the deposition took place at room temperature, we can neglect surface processes. In order to evaluate the importance of the first type of processes we have considered the model developed by Gupta for the interaction in the plasma of an atom M with a molecule of the background oxidizing gas.[135] According to the model, M atoms can react with the gas, O_2 in the present work, to form the respective metal oxide (MO) during the plasma expansion according to the corresponding bimolecular chemical reaction:

$$M + O_2 \rightarrow MO + O^-$$

This reaction is very likely to occur at low collisional energies if it is exothermic, *i.e.* if the reaction exothermicity ΔD is positive, while endothermic reactions ($\Delta D < 0$) should not occur spontaneously. According to the model, ΔD can be calculated from the exothermicity of the dissociation reactions of the monoxide MO and the O_2 molecule:

$$\begin{aligned} MO &\rightarrow M + O \quad (\Delta D_{MO}) \\ O_2 &\rightarrow O + O \quad (\Delta D_{O_2}) \end{aligned}$$

as $\Delta D = \Delta D_{O_2} - \Delta D_{MO}$.

We have applied the model to calculate the formation exotermicities of TeO, TiO and NbO monoxides in the plasma, according to the data taken from ref. [140]. The calculated ΔD are shown in Table 4.2. The formation reactions of TiO and NbO are exothermic while the formation of TeO is endothermic. Therefore, the formation of the two first oxides during the plasma expansion is more likely than that of TeO. Although the model only takes into account the formation of monoxides, it gives information about the oxidation capability of the atmosphere. This result agrees with the fact that deposited films have only reduced Te atoms.

According to Gupta's model, the oxidation of Te is not likely to occur at thermal energies. However, the increase of E leads to a decrease of the fraction of

	TeO	TiO	NbO
ΔD_0 (eV)	-1.25 ± 0.21	1.81 ± 0.9	2.82 ± 0.3

Table 4.2: Reaction exothermicities (ΔD_0) for the formation of Te, Ti and Nb monoxides in reaction with O_2.

Te^0 atoms. This clearly indicates an increase of the probability of the oxidation reaction, which may be associated to two different mechanisms. First, the increase of E leads to an increase of the average kinetic energy of Te atoms. This can be understood if we consider a shifted Maxwell Boltzmann distribution of velocities that has been found to describe the first stages of the plasma expansion [61, 141]:

$$f(v) \propto v^3 \exp\left[-\frac{m(v-u)^2}{2k_B T}\right] \tag{4.5}$$

where m is the particle mass, k_B is the Boltzmann constant, u is the flow velocity, and T is the plasma temperature. The increase of E leads to an increase of T and thus shifts the velocity distribution towards higher v values,[72] and thus this should increase the fraction of Te atoms in the plasma with energies high enough to exceed the energy barrier of the oxidation reaction. The second mechanism that may contribute to the oxidation of Te is the dissociation of O_2 molecules through photodissociation or collision-induced dissociation processes,[135] whose probability also increases when increasing E. The larger the fraction of dissociated O atoms, the easier the oxidation of Te.

The presence of Te^0 in all the E-series films must be related to the high fraction of NBO observed (Figs. 4.5a and 4.6a), since Te^0 atoms should break the Te-O-Te linkages to form Te-Te bonds. The fact that the lowest I_R, *i.e.* the lowest fraction of NBO, in the E-series films occurs at the highest E (1.5 J cm^{-2}) for which the concentration of Te^0 atoms is also the lowest in the E-series, supports the effect of Te^0 on the glass structure.

Although increasing the laser energy density increases the oxygen content in the films, Te^0 is not completely removed for the highest E considered, and it has not been possible to obtain films with a network structure similar to that of the bulk glass in any of the E-series films. This experimental result is likely related to the fact that, although increasing E increases the average kinetic energy of the plasma species, there are always atoms with low kinetic energy and thus, with not enough energy to exceed the energy barrier of the oxidation reaction. On the contrary, the results obtained for the P_{O_2}-series have shown that increasing the oxygen pressure at a fixed E allows achieving the characteristic structure of tellurite bulk glasses. Therefore, the experimental results obtained in this thesis point out that P_{O_2} is the main experimental parameter. The compositional (Figs. 4.2b and 4.4b) and structural (Fig. 4.5b) analyses of the P_{O_2}-series films suggest two different pressure ranges. In the case of films deposited at $P_{O_2} \leq 5$ Pa, their

oxygen content slightly increases as P_{O_2} increases, while they have a percentage of Te^0 close to 4% and a network structure similar to that of E-series films. However, in the case of films deposited at $P_{O_2} \geq 8$ Pa, their oxygen content slightly decreases as P_{O_2} increases, they have no Te^0 atoms and their network structure is similar to that of the bulk glass.

These two pressure ranges can be understood in terms of the plasma length, L_p. According to what it was discussed above, this distance is the limit between two different plasma expansion regimes since it determines the maximum expansion distance of the plasma plume. Therefore, the processes involved in the film nucleation and growth must be different depending on the relation between L_P and the distance target-substrate, D.

According to the relation 4.1, P_{O_2} determines L_p which defines two different deposition regimes for $D > L_p$ and $D < L_p$ for a given set of experimental conditions, *i.e.* fixed E and D. On the one hand, L_p could be similar or slightly shorter than D for films deposited at $P_{O_2} \geq 8$ Pa and thus, the species would reach the substrate by diffusion. This low energy deposition process is more similar to the traditional thermal melting of bulk glass, thus leading to the formation of network structures similar to that of bulk glass. On the other hand, for films deposited at $P_{O_2} \leq 5$ Pa, L_p is most likely larger than D and thus, the species would reach the substrate with no negligible kinetic energy, and the deposition process would be far from that of bulk glass melting. The presence of Te^0 atoms in this case seems to be in contradiction with the tendency observed in the E-series films (Te^0 decreased when increasing the kinetic energy of the species), thus suggesting the presence of additional mechanisms for the oxidation of Te atoms or the dissociation of O_2 molecules. The presence of a high P_{O_2} allows, according to the shock wave model, the formation of a shock layer at the contact region between the plasma plume and the background gas.[134] In the shock layer, the O_2 density and temperature are much higher than those of the O_2 gas, easing the dissociation of the O_2 molecules,[142] and favoring the oxidation of Te atoms in spite of decreasing the kinetic energy of the plasma species.

To sum up, the experimental results shown demonstrate that the increase of both the laser energy density and the oxygen pressure favors the deposition of films with similar compositions to that of the bulk glass. The increase of the laser energy density favors the oxidation of Te atoms by increasing the kinetic energy of Te atoms and the dissociation of O_2 by collisional and photoinduced processes. However, the main mechanism for the oxidation of Te, which avoids

the presence of Te^0 atoms in the films, seems to be the dissociation of O_2 at high oxygen pressures due to the formation of a high density region during the plasma expansion. The deposition of films with the right composition is fundamental since, according to the experimental results, the structure and optical properties of films are strongly affected by the presence of Te^0 atoms. In the next section, we will relate the linear optical response of films deposited at different E and P_{O_2} with their composition and structure discussed above.

4.2.4 Effects of the film composition and structure on the linear optical properties

The evolution of n and κ with the E and P_{O_2} (Figs. 4.7 and 4.8) must be related to the presence of Te^0 atoms and the large NBO content observed in the films, that were shown in Figs. 4.4 and 4.6. Te^0 atoms increase the refractive index, as it has been previously observed in the case of sputtered TeO_x films, due to the metallic character of the reduced Te,[30] whereas the high polarizability of the NBO atoms leads to an increase of the refractive index when the concentration of NBO increases as well.[59] However, the results shown in Fig. 4.7b indicate that films deposited at $P_{O_2} \geq 8$ Pa have refractive indexes lower than that of bulk glass in spite of their larger NBO content with respect to the bulk glass (Fig. 4.6), which suggests the existence of additional factors that contribute to n. In order to understand these low n values, it is important to have in mind that in the case of optical materials n is related not only to the polarizabiltity of the sample constituents but also to the sample density (ρ) [98]:

$$n = \sqrt{\frac{1 + A\rho}{1 - A\rho}} \qquad A = \frac{4\pi}{3}\frac{\alpha_m N_A}{M} \tag{4.6}$$

where α_m and M are, respectively, the average polarizability and the molecular weight of the compound, and N_A is Avogadro's number. According to that relation, the lower the film ρ, the lower the refractive index. Therefore, the results obtained in the experimental characterization of the films suggest that, depending on the deposition conditions, film glasses may comprise a fraction of Te^0 atoms diluted in a glass matrix that is less dense and has a more disordered vitreous network than bulk glass. In order to effectively correlate the composition and structure of the films with their optical properties, we have modeled the films using the Maxwell Garnett effective medium theory.[143] Effective medium models have been successfully used to simulate the ellipsometric data of amorphous TeO_x

films [144] or amorphous Ge films with different fraction of voids.[145] Maxwell Garnett expressions evaluate the optical response of a medium consisting of a microstructure of one or more constituents, completely surrounded by a different material that acts as host. In the present work, we have considered that film glasses are a mixture of three different constituents. The host is a glass matrix that presents inclusions consisting of particulates of reduced Te and a fraction of voids responsible for the reduced density of the films. We also assume that Te^0 atoms are diluted in the glass matrix, since the experimentally determined fraction of Te^0 is below 10% in all cases. Figure 4.9 shows an scheme of the structure of the film.

According to the Maxwell Garnett effective medium model, the effective dielectric function of the composite material (ϵ) is described in terms of the dielectric function of the host (ϵ_h) and the materials diluted in the host (ϵ_i) [143]:

$$\frac{\epsilon - \epsilon_h}{\epsilon + 2\epsilon_h} = \sum_i f_i \frac{\epsilon_i - \epsilon_h}{\epsilon_i + 2\epsilon_h} \tag{4.7}$$

where f_i is the volume fraction occupied by each constituent.

We have modeled the experimental ellipsometric data (Ψ and Δ) obtained for the different film glasses according to the expression 4.7. The volume fractions of the glass matrix, voids, and tellurium clusters are f_{M}, f_{V}, and f_{Te} respectively. The optical properties of the glass matrix are based on those of the bulk glass. However, since Raman spectra have shown that film glasses have a higher content of highly polarizable NBO than bulk glass and thus, the optical properties of the

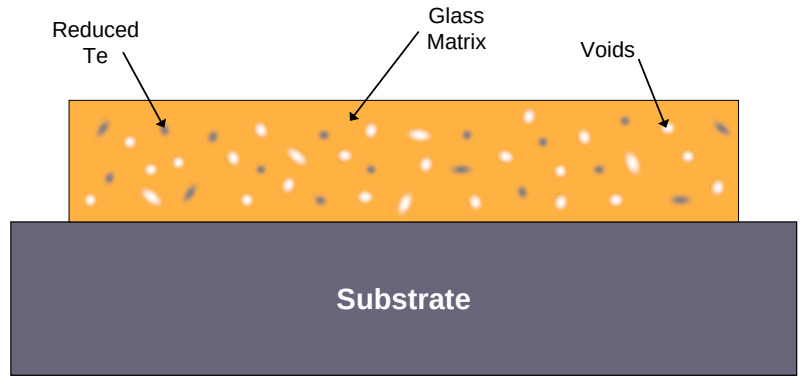

Figure 4.9: Effective medium model of tellurite thin film glasses. It consisted of a tellurite glass matrix with a non negligible fraction of voids and reduced Te atoms.

matrix can differ from those of bulk glass. Therefore, the n of the matrix is described according to a Cauchy dispersion

$$n(\lambda) = A_n + \frac{B_n}{\lambda^2} + \frac{C_n}{\lambda^4} \tag{4.8}$$

with different coefficients than those of bulk glass. The optical properties of voids and tellurium clusters are well known, and they are taken from tabulated data: in the case of voids, $\hat{n}$ is that of vacuum ($n = 1$ and $\kappa = 0$) while in the case of tellurium, the dispersion of $\hat{n}$ of both crystalline [146] and amorphous tellurium [147] has been considered.

Therefore, the fitting parameters are f_{M}, f_{V}, f_{Te}, and also the parameters A_n, B_n and C_n of the glass matrix Cauchy dispersion. Figure 4.10 illustrates the results of the modeling of Ψ and Δ for two representative films, one with (E150P05) and one without reduced Te (E150P08). The parameters obtained are summarized in Table 4.3. The fittings to the experimental data obtained using the optical properties of amorphous Te are much worse than in the case of crystalline Te, suggesting that reduced Te is most likely crystalline and thus, only the data obtained using the optical properties of crystalline Te are included in Table 4.3. The quality of the fittings also improves as the percentage of reduced Te decreases. the fraction of voids is approximately constant in all cases ($f_{\mathrm{V}} \sim 0.10$), while f_{M} and f_{Te} have opposite trends. f_{M} and f_{Te} range respectively from 0.78 and 0.09 for the film deposited at the lower E (0.75 J cm^{-2}) to 0.90 and 0 for films deposited at $P_{O_2} \geq 8$ Pa. In the case of the Cauchy parameters, A_n shows a

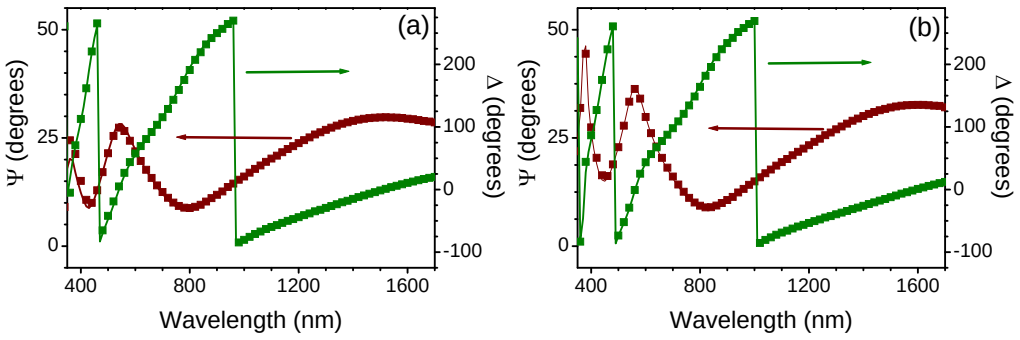

Figure 4.10: (red line, green line) Simulation of the (■,■) experimental ellipsometric data of (a) E150P05 and (b) E150P08 films using the Maxwell Garnett effective medium.

Sample	f_V ± 0.01	f_{Te} ± 0.01	f_M ± 0.01	A_n ± 0.01	$B_n \pm 0.01$ $\times 10^{-2}$ μm^2	$C_n \pm 0.01$ $\times 10^{-3}$ μm^4
bulk glass	-	-	-	2.11	2.14	7.93
E075P05	0.13	0.09	0.78	2.39	1.00	7.93
E100P05	0.11	0.07	0.82	2.23	1.97	0
E125P05	0.11	0.07	0.82	2.21	2.80	0.94
E150P03	0.09	0.05	0.86	2.16	1.01	5.01
E150P05	0.09	0.03	0.88	2.16	2.31	2.32
E150P08	0.09	0	0.91	2.15	1.96	3.34
E150P11	0.10	0	0.90	2.11	1.38	4.23

Table 4.3: Volume fractions and parameters of the Cauchy dispersion of the matrix determined from modeling the optical response of films in the E- and P_{O_2}-series using the Maxwell Garnett effective medium.

clear trend: it increases when E or P_{O_2} decreases, which implies an increase of n. This behavior is in very good agreement with the fact that films deposited at low E or P_{O_2} have a higher amount of NBO, and therefore their network structure is more polarizable, which leads to an increase of the refractive index of the glass matrix. Parameters B_n and C_n do not show a clear trend with E or $P_{O_2}$and their effect in the value of n is much less important than the parameter A_n.

The film density or the amount of reduced Te atoms can be calculated from the volume fraction obtained from the simulation. In the first case, film ρ has been calculated from the volume fractions of the glass matrix and the reduced Te since voids do not contribute to the mass of the film. Therefore, film ρ is equal to the sum of the densities of the bulk glass ($\rho_B = 5.43$ g cm^{-3}) and the crystalline tellurium ($\rho_{Te} = 6.24$ g cm^{-3}) weighted by their respective volume fractions:

$$\rho = \rho_B f_M + \rho_{Te} f_{Te} \tag{4.9}$$

The values of ρ estimated from the model are 4.9 ± 0.2 g cm^{-3} in all cases. This value can be compared with the indirect determination of the film density from the measured surface atomic density, the relative composition of the films, obtained from RBS and NRA data, and the highly accurate film thickness determined through ellipsometry. This calculation leads to estimate ρ values of 4.8 ± 0.2 g cm^{-3} for all films, which are in excellent agreement, within the experimental error, with the values estimated from the effective medium model. Moreover, the ρ values determined from both methods are a 10% lower than that measured for the bulk glass with the traditional Archimedes' method ($\rho = 5.43$ g cm^{-3}).[88]

X_{Te^0}, which is the ratio between amount of reduced Te atoms (N_{Te^0}) and the

total amount of Te atoms ($N_{Te^0} + N_{Te^{4+}}$), can be also estimated from the results of the Maxwell Garnett model. The atomic densities of Te^0 and Te^{4+} atoms are:

$$\frac{N_{Te^0}}{V} = f_{Te}\frac{\rho_{Te}}{m_{Te}}N_A \qquad \frac{N_{Te^{4+}}}{V} = 0.9 f_M \frac{\rho_B}{m_B}N_A \tag{4.10}$$

where m_B (160.92 g mol^{-1}) and m_{Te} (127.6 g mol^{-1}) are the molecular and atomic weight of the bulk glass and Te respectively. Then, X_{Te^0} can be calculated according to:

$$X_{Te^0} = \frac{N_{Te^0}}{N_{Te^0} + N_{Te^{4+}}} = \left(1 + 0.9\frac{m_{Te}}{m_B}\frac{\rho_B}{\rho_{Te}}\frac{f_M}{f_{Te}}\right)^{-1} \tag{4.11}$$

The experimental values of X_{Te^0} measured by XPS and those calculated using the Maxwell Garnett model are compared in Figure 4.11. Both X_{Te^0} values show the same trend. Although the estimated X_{Te^0} values are higher than those experimentally measured in the E-series (15% and 8% respectively at 0.75 J cm^{-2}), the content of reduced Te decreases as E increases in both measurements. In the case of the P_{O_2}-series, the experimental and estimated X_{Te^0} values are equal, within the experimental error, for films deposited at $P_{O_2} \geq 5$ Pa. In particular, the effective medium model predicts the absence of reduced Te in films deposited at $P_{O_2} \geq 8$ Pa. The fact that those films with a lower fraction of reduced Te show a better agreement between experimental and modeled values of X_{Te^0} is related to the initial assumptions of the Maxwell Garnett model, in which

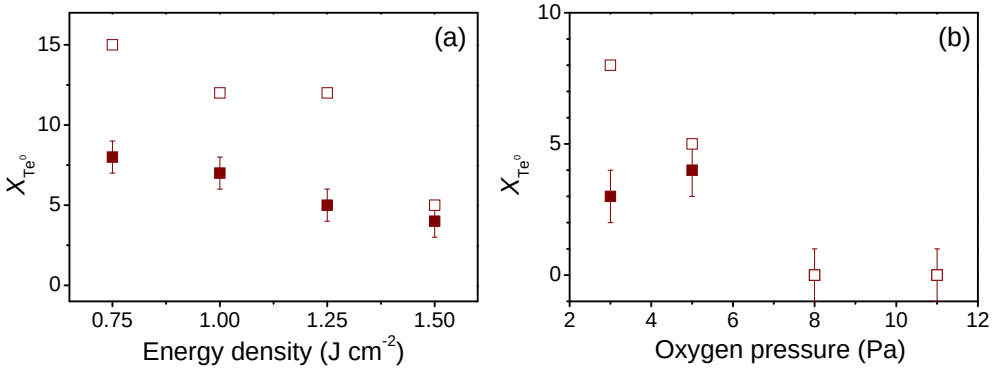

Figure 4.11: Percentage of reduced Te atoms (Te^0) deduced from (■) the experimental XPS data and (□) from the Maxwell Garnet effective medium model applied to (a) E- and (b) P_{O_2}-series films.

the minority phases should be diluted in the matrix. The higher the amount of reduced Te in the E-series films or in these deposited at low P_{O_2}, the less accurate the model is.

Therefore, we can conclude that it is possible to apply the Maxwell Garnett effective medium model to describe the optical response of tellurite thin film glasses deposited by PLD with reduced concentrations of Te^0 atoms. The qualitative agreement between the compositional and structural results derived from the Maxwell Garnett fitting parameters and the experimental measurements suggests that films can be considered to be formed by a mixture of clusters of Te^0 atoms and voids diluted in a glass matrix. These results improve as the Te^0 content decreases, while the values of the fraction of voids experimentally measured and optically deduced are very similar in all cases ($f_V \sim 0.10$).

4.3 Films deposited using the optimum experimental conditions

The results presented in the previous section show that films without reduced Te atoms and having glass networks similar to that of the bulk glass can be produced by increasing both the laser energy density and the oxygen pressure. However, the use of laser energy densities of several J cm^{-2} leads to the presence of molten droplets on the film surface [61] or may cause partial re-sputtering of the deposited material,[66] whereas the use of a too high background gas pressure makes difficult the production of stoichiometric films due to the preferential diffusion of light atoms,[70] decreases the density of films, and reduces the adherence of the film to the substrate.[65] Therefore, the useful range of laser energy densities and oxygen pressures is limited to a narrow interval.

In the case of the tellurite films studied in the present chapter, we consider that the optimum conditions are those in which all the ablated species are oxidized and the energy of the species is low enough to allow the formation of a vitreous network similar to that of the bulk glass but high enough to ease the adherence of the atoms to the substrate. Moreover, since the final objective is the use of these films as elements for the development of photonic devices, the optimum films should be those with the lowest possible absorption while maintaining simultaneously a large value of n, as this improves the light confinement in waveguide devices [1] and it is related to high $\chi^{(3)}$values.[11, 16]

Therefore, according to the analysis of the composition, structure, and optical response of E- and P_{O_2}-series films, we have chosen as optimum experimental conditions those of the film E150P08: E = 1.5 J cm^{-2} and P_{O_2} = 8 Pa. This film has no reduced Te atoms, shows a Raman spectrum similar to that of the bulk glass and has the higher n among the films with κ values below the experimental resolution limit. These deposition conditions have been considered as the starting point for the synthesis of transparent film glasses with a thickness of 1-4 μm from bulk glasses with different compositions. However, since the film properties are so sensitive to the deposition conditions, it has been necessary to carefully adjust the exact deposition parameters depending on each target.

The most important differences in the deposition conditions among the different experimental series arise from variations in the size of the laser spot and the target-substrate distance. The exact laser energy and spot size were adjusted in each series in order to have an energy density of E = 1.5 J cm^{-2} on the surface of the target, but slightly different spot sizes lead to variations in the energy density and thus, in the plasma expansion. Furthermore, there are strongly compositional differences among the bulk glasses considered in the present thesis, with cations with very different atomic masses, shown in Table 4.4. Since the dynamics of the species in the plasma depends on their masses, the plasma expansion will differ among the targets considered. In order to compensate these differences in the plasma dynamics, we have fixed the laser energy density (E = 1.5 J cm^{-2}) and the target-substrate distance (D = 3 cm), and we have slightly varied the oxygen pressure until we have obtained transparent optimum films. Table 4.5 summarizes the deposited films and the nominal composition of the bulk target from which they were deposited.

In the case of thick film glasses belonging to the system TeO_2–TiO_2–Nb_2O_5,

Cation	Atomic mass (amu)
Ti^{4+}	47.9
Nb^{5+}	92.9
La^{3+}	138.9
Te^{4+}	127.6
Ta^{5+}	180.9
W^{6+}	183.8
Pb^{2+}	207.2
Bi^{3+}	209.0

Table 4.4: Atomic masses of the different cations present in the TeO_2-based glasses studied.

Bulk sample	Nominal composition of bulk sample	Film sample
TTN	$90TeO_2 \cdot 5TiO_2 \cdot 5Nb_2O_5$	FTTN
TW15	$85TeO_2 \cdot 15WO_3$	FTW15
TWTi	$80TeO_2 \cdot 15WO_3 \cdot 5TiO_2$	FTWTi
TWNb	$80TeO_2 \cdot 15WO_3 \cdot 5Nb_2O_5$	FTNb
TWTa	$80TeO_2 \cdot 15WO_3 \cdot 5Ta_2O_5$	FTWTa
TWLa	$80TeO_2 \cdot 15WO_3 \cdot 5La_2O_3$	FTWLa
TWBi	$80TeO_2 \cdot 15WO_3 \cdot 5Bi_2O_3$	FTWBi
TWPb	$80TeO_2 \cdot 15WO_3 \cdot 5PbO$	FTWPb
TWP1	$85TeO_2 \cdot 15WO_3$	FTWP1
TWP3	$80TeO_2 \cdot 15WO_3 \cdot 5PbO$	FTWP3
TWP6	$70TeO_2 \cdot 20WO_3 \cdot 10PbO$	FTWP6
TWP8	$60TeO_2 \cdot 30WO_3 \cdot 10PbO$	FTWP8
TWP9	$60TeO_2 \cdot 20WO_3 \cdot 20PbO$	FTWP9
TWP10	$50TeO_2 \cdot 30WO_3 \cdot 20PbO$	FTWP10

Table 4.5: TeO_2-based thin film glasses deposited using the optimum deposition conditions. The starting bulk glasses and their nominal composition are also shown.

the optimum P_{O_2} used was 10 Pa while for the system TeO_2–WO_3–R_xO_y, the optimum P_{O_2} was found to be in the range of 7-10 Pa. Finally, film TeO_2–WO_3–PbO glasses were deposited in a different chamber with a longer target-substrate distance (D = 4 cm) than the one used in the previous systems. Therefore, in order to achieve a plume length similar to that distance, it was necessary to decrease the oxygen pressure according to relation 4.1. In this case, the optimum pressure was found to be 4-5 Pa.

4.3.1 Composition and structure

The composition and the structure of the films shown in Table 4.5 were analyzed using ion beam techniques, XPS, and Raman spectroscopy. Figure 4.12 shows the molar composition of the films belonging to the TWR-series. As in the previous cases, both techniques show a very good agreement. The TeO_2 molar content in the films is in all cases similar, within the experimental error, to that of the bulk glasses. However, some minor variations can be observed in the case of WO_3 and the third oxide (R_xO_y). While the molar content of WO_3, Ta_2O_5, PbO, and Bi_2O_3 is similar or larger in the films than in bulk glasses, the molar content of TiO_2, Nb_2O_5 or La_2O_3 decreases with respect to that of bulk glasses. In all cases, XPS measurements have shown that the oxidation state of the different cations remains unchanged. In the case of the TWPb-series, the results of the

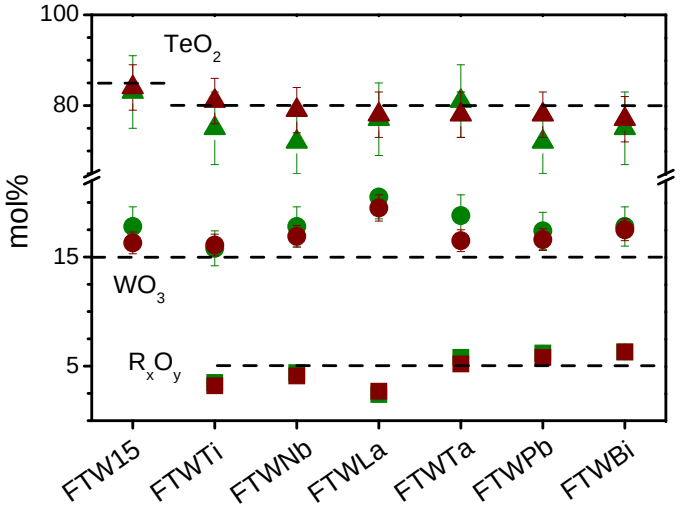

Figure 4.12: Molar composition of TWR-series film glasses measured by (red symbols) ion beam techniques and (green symbols) XPS. Symbols correspond to the molar content of (▲, ▲) TeO_2, (●, ●) WO_3 and (■, ■) the third oxide. Dashed lines indicate the nominal molar composition of the bulk glasses.

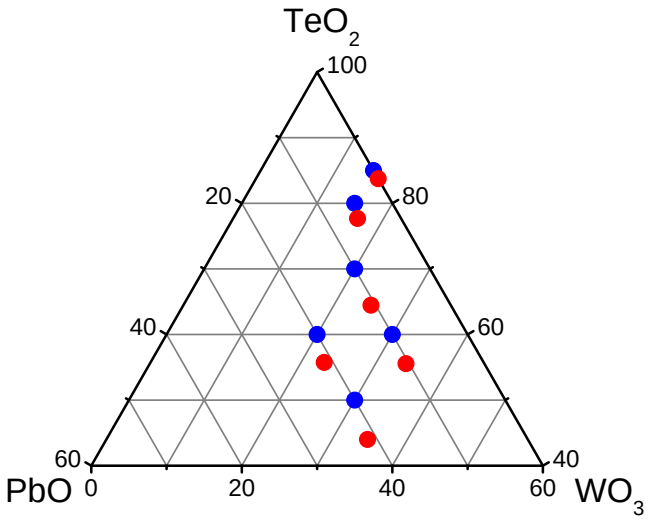

Figure 4.13: (●) Bulk and (●) film molar composition of TWPb-series glasses.

compositional analysis are shown in Figure 4.13. A decrease of the TeO_2 molar content is observed for all films, while the molar contents of WO_3 and PbO increase in all cases, being this increase larger in the case of WO_3. Moreover, the compositional differences with respect to the bulk glasses are more marked in the samples with the lowest TeO_2 molar content.

As it has been already discussed, these differences are related to the different flux angular distribution observed for species of different masses in PLD of multicomponent targets.[61] The presence of a background gas atmosphere of the order of several Pa leads to the scattering of plume species with the gas molecules. This process is expected to preferentially broaden the angular distribution of the low-mass species, since these atoms should suffer a higher change in its trajectory than heavier atoms when they collide with gas atoms.[43] Therefore, films can show an enrichment of heavy atoms in the center of the deposited film. The differences in the relative composition of films and starting bulk glasses shown in Figs. 4.12 and 4.13 can be related to the differences in the mass of the cations (Table 4.4). Films are deficient in those cations that are lighter than W, while films with atoms heavier than W, such as Pb or Bi, show a slight increase of the relative content of these atoms.

Films produced in the optimum conditions show also structures similar to those of the bulk glasses. Figure 4.14a shows the Raman spectra of the film FTW15 and the corresponding $85TeO_2 \cdot 15WO_3$ bulk glass. The general shape of the film spectrum is the same as that of the bulk glass with the same bands

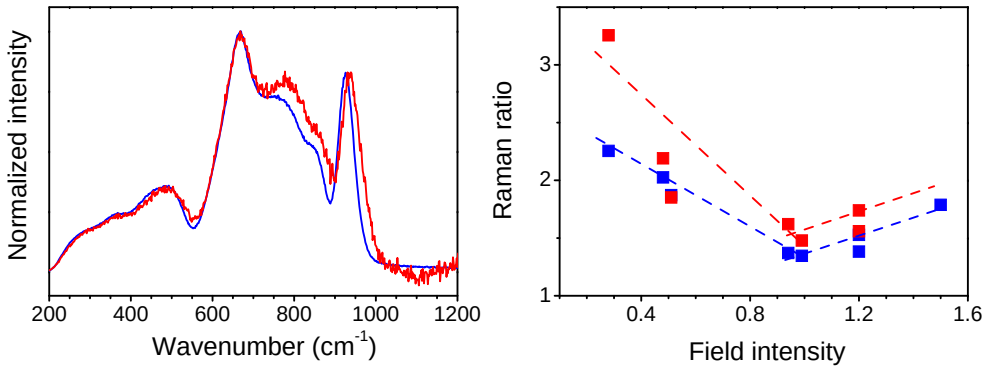

Figure 4.14: (a) Raman spectra of (red line) FTW15 film and (blue line) TW15 bulk glasses. (b) Raman intensity ratio of TWR-series (■) film and (■) bulk glasses. The dashed lines are guides for the eyes.

and thus, it is possible to deconvolute the spectrum using the same 8 peaks as those used for bulk glasses (Fig. 3.10 and Table 3.4). There are two main differences between the two spectra: First, the intensity of the 700 – 800 cm^{-1} band, assigned to vibrations of NBO, is higher in the films than in the bulk glass, thus indicating a higher fraction of NBO in the film glass network. Second, the position of the peak at 925 cm^{-1}, related to the vibration of W=O bonds in [WO_6] octahedral units, is shifted towards higher wavenumbers in the case of the films, which is related to the higher WO_3 relative molar content observed in the films (Fig. 4.12). As it has been discussed in the case of TWPb-series bulk glasses, the shift towards higher wavenumbers of this peak as the WO_3 molar content increases is related to the high field intensity of W^{6+} cations.

Raman spectra of the other film glasses show the same behavior and thus they are not shown here. In order to compare the fraction of NBO in the different TWR-series film and the respective bulk glasses, we have calculated the ratio I_R between the intensity of the Gaussian peaks related to NBO and the main peak at 660 cm^{-1}, according to relation 4.4. The obtained values are shown as a function of the field intensity of the cation R in Figure 4.14b, both for film and bulk glasses. Both show the same trend, with two different regions, one for cations with low field intensities (Pb^{2+}, La^{3+} ad Bi^{3+}) and high I_R values, and the other for large field intensity cations (Ti^{4+}, Ta^{5+}, Nb^{5+}, and W^{6+}) and slightly higher

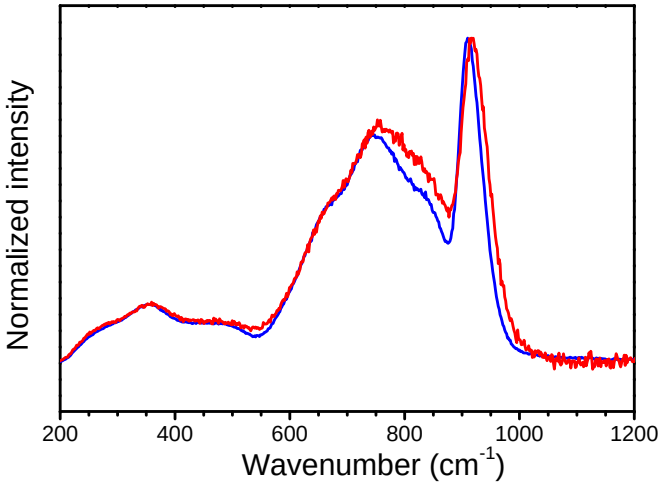

Figure 4.15: Raman spectra of (red line) FTWPb10 film and (blue line) TWPb10 bulk glasses.

I_R values than that of the binary glass. Furthermore, the Raman ratio of films is always higher than that of the starting bulk glasses, which confirms that films have higher concentration of NBO and a more disordered glass network than bulk glasses.

This behavior is also observed in film glasses belonging to the TWPb-series. This illustrated in Figure 4.15, where the Raman spectra of the film having the lowest TeO_2 molar content (TWPb10) and of the corresponding bulk glass are shown. The spectra have the same general shape, but the film spectrum showa a clearly higher intensity of the band related to NBO (700 – 800 cm^{-1}) and a slight shift of the peak at 910 cm^{-1} when compared to that of bulk glass, as it was previously observed in TWR-series glasses (Fig 4.14a).

4.3.2 Linear optical properties

As it has been stated earlier, our optimum deposition conditions are those which allow us to obtain transparent film glasses with a refractive index as high as possible. However, the particular compositional and structural properties of the films from TWR and TWPb-series must also affect their optical response. In the present section, we characterize the linear optical properties of optimum films by means of the linear refractive index, $\hat{n}$, and the position of the UV optical absorption edge.

Figure 4.16 shows the dispersion of n and κ and the transmission spectrum of a 3 μm thick film deposited from a TW15 bulk glass ($85TeO_2 \cdot 15WO_3$). Fig. 4.16b also includes the transmission of the glass substrate on which the film was deposited as a reference. The value of n is always larger than 2, while κ strongly decreases down to values below our experimental resolution limit at $\lambda \gtrsim 450$ nm. The film transmission spectra are characterized by oscillations due to the interference between the transmitted and reflected beams at the interfaces air-film, film-substrate, and substrate-air. The transmission oscillates from ~ 0.77 to that of the substrate (~ 0.91), which is the maximum reachable transmission. These values correspond to a high transparency since the maximum transmission of a film glass with such a high index (2.075 at 1500 nm) is 0.82 at that wavelength according to Fresnel reflection coefficients.[73] This value is similar to the average transmission discarding the oscillations due to interferences, and thus it indicates that films are highly transparent in the near-IR. Film transmission spectrum has also a sharp absorption edge, which is only related to the tellurite glass absorption

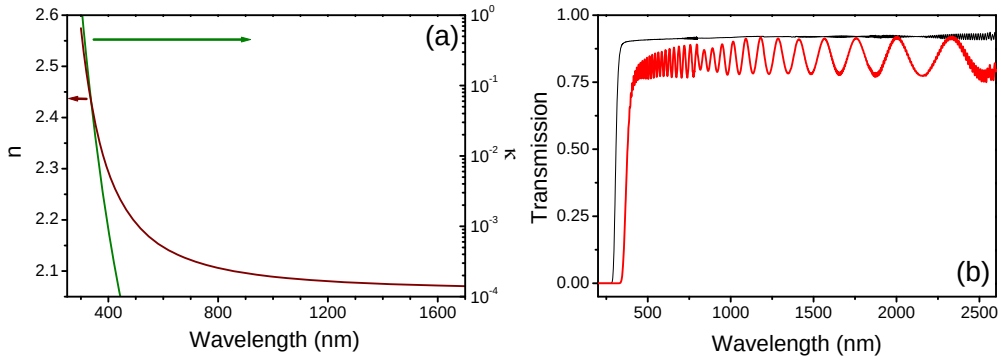

Figure 4.16: (a) Refractive index ($\hat{n} = n + i\kappa$) and (b) transmission of a FTW15 film. The transmission of the borosilicate glass used as substrate it is also shown in (b).

edge as the absorption edge of the substrate is blue-shifted.

All optimum films have similar optical properties: high refractive indexes well fitted using a Cauchy dispersion and high transparency, characterized by low κ values and high transmission at wavelengths larger than that of the UV absorption edge. Therefore, in the next sections we focus the study of the linear optical response of films on the comparison of the real part of their refractive indexes, and the characterization of their UV absorption edges by means of the optical gap.

Linear refractive index

Table 4.6 summarizes the refractive index at 1500 nm of TWR- and TWPb-series films. κ values determined from ellipsometry are always below our resolution limit ($< 10^{-4}$) at that wavelength. In all cases, the refractive index is smaller than that of the bulk glass, which indicates that films have lower densities than bulk glasses as discussed above. In order to support that affirmation, the density of TWR-series films has been determined from the compositional analysis by ion beam techniques and compared to the one deduced using the Maxwell Garnett effective medium model. In this case, the effective medium only comprises the glass matrix with the optical properties of bulk glasses and a fraction of voids approximately equal to 0.10, since XPS measurements of those films have shown no changes on the oxidation state of cations.

Figure 4.17 shows the ratio between the film and bulk density, the first ob-

Sample	n ±0.005 at $\lambda = 1500$ nm	
	Bulk glass	Film glass
TTN	2.120	2.010
TW15	2.120	2.075
TWTi	2.120	2.020
TWNb	2.125	2.005
TWTa	2.110	2.070
TWLa	2.090	1.985
TWBi	2.140	2.075
TWPb	2.120	2.050
TWPb1	2.120	2.075
TWPb3	2.120	2.050
TWPb6	2.130	2.090
TWPb8	2.140	2.080
TWPb9	2.150	2.090
TWPb10	2.150	2.100

Table 4.6: Refractive index of TWR- and TWPb-series bulk and film glasses measured at 1500 nm.

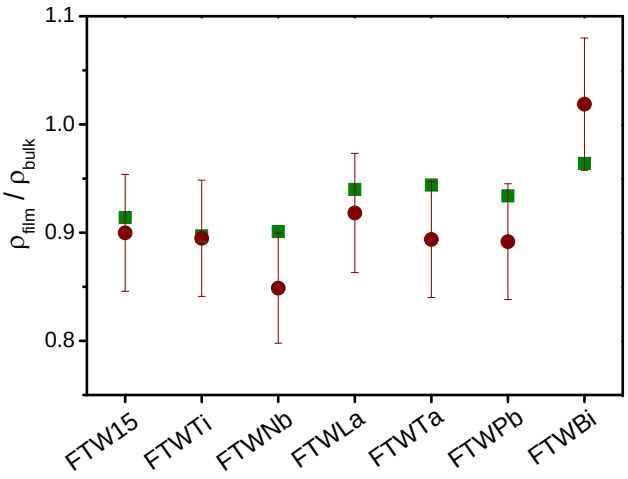

Figure 4.17: Density of film glass in TWR-series determined from (●) compositional analysis and (■) estimated from their optical properties through the Maxwell Garnett effective medium model.

tained from either compositional or optical measurements and the latter measured by the Archimedes' method. As in the previous cases, there is a very good agreement between the experimental and the modeled values of ρ. The ρ of films is 90% that of the bulk glasses except in the case of the film FTWBi, in which bulk and film density are similar. This difference with respect to the others films is related to the composition of the film shown in Fig. 4.12. Films have an increment in the concentration of heavy atoms with respect to the bulk glass, which is more marked in the case of FTWBi due to the large mass of Bi atoms. Therefore, the molecular weight, and thus the film density of FTWBi, is higher than that of other films. The volume fraction of voids deduced from the effective medium model is 10% in all films, which is similar to the values shown previously for E- and P_{O_2}-series films.

Optical transmission

As it has been shown in Fig. 4.16, film glasses show high transmission values in the range from 500 nm to 2500 nm and thus, they have no intrinsic absorption at wavelengths longer than that of their UV absorption edge. As discussed in Chapter 2, the position of this edge has been characterized by the optical gap (E_g), deduced from the Tauc formula.

In the case of film glasses, it has not been possible to determine the optical cutoff or the Urbach energy like in bulk glasses due to the interference patterns in the transmission spectra of the films. In the wavelength range at which the optical cutoff occurs, the oscillations in the transmission value are still very marked, and thus they may lead to wrong values of the optical density. Moreover, the Urbach region corresponds to those photon energies at which the absorption coefficient is below 10^4 cm^{-1}, and this corresponds to regions in which the interference pattern does not permit to have a good fitting to the Urbach formula. To illustrate that point, Figure 4.18a shows the oscillating $\ln(\alpha)$ values for $\alpha < 10^4$ in the case of a FTWPb film glass. On the contrary, the region of higher absorption coefficients ($\alpha \gtrsim 10^4$ cm^{-1}) can be easily fitted to the Tauc formula, which allows determining the value of E_g, as it is shown in Figure 4.18b.

Table 4.7 shows the value of the E_g of the deposited film glasses and the values of the optical cutoff of the respective bulk glasses. Although E_g and the optical cutoff are measurements not directly comparable, both describe the position of the UV absorption edge, and thus, they should show similar trends, as it is

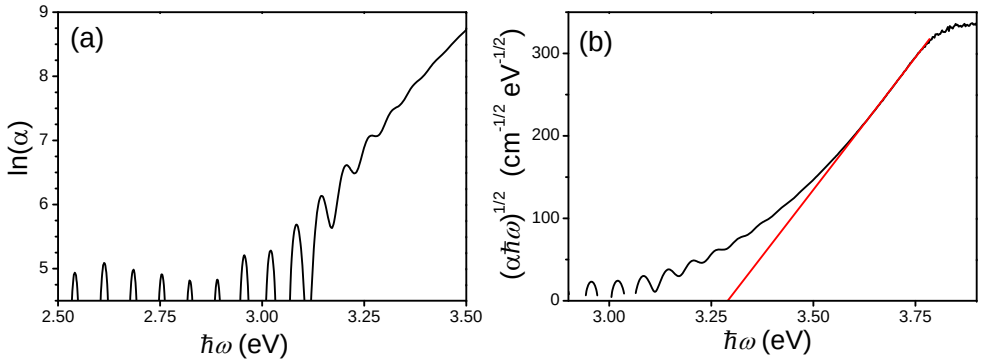

Figure 4.18: (a) Urbach and (b) Tauc plots for a FTWPb film glass. In the latter case, the experimental values have been fitted to the Tauc relation.

indeed observed: all E_g values are in the range from 3.30 eV to 3.49 eV and film glasses deposited from bulk glasses with large optical cutoff have large E_g values. However, it is not possible to determine a straightforward relation between the value of E_g and the WO_3 molar content, as it was possible in the case of the optical cutoff in bulk glasses. This is due to differences in the glass network structure of films and bulk glasses. The larger fraction of NBO in the films is related to a more disordered network and leads to lower values of E_g than in the case of bulk glasses, since NBO are weakly bonded to cations, and thus, photons with

Bulk glass	Optical cutoff ±0.01 eV	Film glass	E_g ±0.02 eV
TTN	2.95	FTTN	3.49
TW15	2.79	FTW15	3.30
TWTi	2.80	FTWTi	3.32
TWNb	2.82	FTWNb	3.41
TWTa	2.85	FTWTa	3.44
TWLa	2.88	FTWLa	3.45
TWBi	2.85	FTWBi	3.42
TWPb	2.84	FTWPb	3.34
TWPb1	2.79	FTWPb1	3.30
TWPb3	2.84	FTWPb3	3.34
TWPb6	2.80	FTWPb6	3.36
TWPb8	2.75	FTWPb8	3.30
TWPb9	2.81	FTWPb9	3.41
TWPb10	2.74	FTWPb10	3.37

Table 4.7: Optical properties of TWPb-series.

lower energy are able to excite the electron in the bond.[59, 87] Therefore, the position of the absorption edge is related to both the glass composition and the fraction of NBO. Since the structural differences between bulk and film samples arises from the deposition process, it is not possible to control the exact fraction of NBO in the films glasses. Thus, different samples may have different fractions of NBO, and the contribution to the optical gap of the NBO changes from sample to sample.

4.4 Summary and conclusions

In the present chapter, we have demonstrated the possibility of producing TeO_2-based films by pulsed laser deposition with good optical properties. However, their composition, structure, and linear optical properties are strongly affected by the experimental deposition conditions. In particular we have studied the effect of two experimental parameters: the laser energy density and the oxygen pressure.

The kinetic energy of the ablated species in the plasma plume increases when increasing the laser energy density. The kinetic energy has not only a fundamental effect on the plasma dynamics but also allows chemical reactions between the plasma species and the molecules of the background gas to occur. This is specially important in the case of Te, as its oxidation in a O_2 atmosphere is an endothermic reaction and thus, it is only likely to occur at high energies. In the case of the deposited films, this implies the presence of Te atoms in a reduced oxidation state (Te^0) at low laser energy densities, while the increase of the laser energy density reduces the fraction of Te^0 atoms.

The laser energy density is not the only parameter related to the presence of Te^0 atoms, since high energies are not enough to avoid the presence of Te^0 atoms. It is also necessary to increase the pressure of the background O_2 gas. Although a high pressure decreases the kinetic energy of the species, and this should increase the fraction of Te^0 atoms, it favors the formation of a high gas density region at the boundary of the plasma that eases the dissociation of the O_2 molecules and thus, favors the oxidation of Te. Only films deposited at high laser energy densities and high O_2 pressure have no Te^0 atoms. Moreover, these films also show glass network structures similar to those of bulk glasses, but with larger fractions of nonbridging oxygens.

The optical response of the films is determined by their composition and

structure. Films have reduced densities when compared to bulk glasses, which implies lower refractive indexes. However, the presence of Te^0 atoms and a high fraction of nonbridging oxygens, which have a high polarizability, increases their refractive indexes. The effect on the optical properties of these three factors (low density, Te^0 atoms, and nonbridging oxygens) has been determined using a Maxwell Garnett effective medium model. The measured optical properties show a good agreement with these determined by the model in films with low contents of Te^0 atoms, while the agreement worsens progressively as the Te^0 content increases.

This study has allowed us to define a narrow range of laser energy densities and oxygen pressures, centered at E = 1.5 J cm^{-2} and $P_{O_2} \simeq 8$ Pa, in which optimum films can be deposited. Then different glass compositions belonging to the systems TeO_2–TiO_2–Nb_2O_5, TeO_2–WO_3–R_xO_y, and TeO_2–WO_3–PbO were selected for the production of thin films using the optimum conditions. The composition of the optimum films is characterized by the absence of reduced cations and by a slight enrichment of the heaviest cations. This compositional difference with respect to that of bulk glasses has been related to the dynamics of the heavy cations in the plasma, since species of different masses have different flux angular distributions. The structure of the optimum film glasses is also found to be similar to that of bulk glasses, and it only differs in the higher fraction of nonbridging oxygens in films.

Regarding the optical properties, optimum films are transparent in a wide range of wavelengths and have refractive indexes lower than those of bulk glasses, due to their lower density. The optical gap of films has been determined and shows a similar trend to that of the optical cutoff in bulk glasses. However, in the case of films, E_g is not only related to the film glass composition, but also to the large fraction of nonbridging oxygens, whose concentration changes from sample to sample. In the next chapter, we will study and discuss the nonlinear optical response of film and bulk glasses.

Chapter 5

Nonlinear optical properties of multicomponent glasses

This chapter focuses on the study of the nonlinear optical response of tellurite and germanate bulk and film glasses containing a large amount of transition metal (TM) and heavy metal (HM) oxides. For this purpose, we have measured the modulus of the diagonal component of the third order optical susceptibility tensor ($\left|\chi^{(3)}_{xxxx}\right|$) of the samples by Degenerate Four Wave Mixing (DFWM).

In the first place, the resonant or nonresonant origin of the nonlinear response of tellurite glasses is studied as a function of the excitation wavelength. In the nonresonant case, the differences observed between the nonlinear optical response of bulk and film glasses are analyzed and discussed in terms of the results shown in the previous chapters regarding the composition, structure, and linear optical properties of glasses.

The knowledge acquired in the case of TeO_2-based glasses is then applied to a different glass system: Nb_2O_5–PbO–GeO_2. In this case, film glasses show strong differences in their linear and nonlinear optical properties when compared to those of bulk glasses, that are greater than in the case of tellurite glasses. In this part of the chapter, we summarize first the most relevant previous results for this system regarding the composition and linear optical properties, show the structural analysis of bulk and film glasses, and finally apply the same methodology than in the case of tellurite glasses to understand the origin of their nonlinear response.

5.1 Nonlinear optical properties of TeO_2-based glasses

The results shown in the previous chapter have proven the possibility of synthesizing transparent tellurite thin film glasses by pulsed laser deposition if the experimental conditions are adequate. These films have a composition similar to that of bulk glasses and a glass network having a higher fraction of nonbridging oxygens (NBO). Moreover, film glasses are less dense than bulk glasses and thus, their linear refractive indexes are lower than those of bulk glasses.

The composition and structure of films must affect not only their linear optical response, as shown in Chapter 4, but also the nonlinear one. Therefore, representative 3 – 4 μm thick transparent film glasses were deposited on transparent substrates using the optimum deposition conditions to measure the modulus of the diagonal component of their third order optical susceptibility, $\left|\chi^{(3)}_{xxxx}\right|$.

Initially, we study the dispersion of the $\chi^{(3)}$ values[1] of a $90TeO_2 \cdot 5TiO_2 \cdot 5Nb_2O_5$ bulk glass and of a film deposited from it, in order to determine the spectral range in which the nonlinear optical response has an exclusive nonresonant origin. Second, the nonresonant $\chi^{(3)}$ values of TeO_2-based bulk and film glasses belonging to the TeO_2–WO_3–R_xO_y and TeO_2–WO_3–PbO systems are measured and discussed. These bulk glasses show enhanced nonlinear optical response with respect to the TeO_2–TiO_2–Nb_2O_5 glasses due to the presence of highly polarizable cations. In the case of films, the comparison between the $\chi^{(3)}$ values of film and bulk glasses allows quantifying the contribution of the NBO to the nonlinear optical response.

5.1.1 $\chi^{(3)}$ values of TeO_2–TiO_2–Nb_2O_5 glasses

The nonlinear response of the $90TeO_2 \cdot 5TiO_2 \cdot 5Nb_2O_5$ bulk glass (TTN) and the film glass deposited from it (FTTN) has been characterized at different wavelengths. The study of the dispersion of $\chi^{(3)}$ allows us to determine at which wavelengths the nonlinear optical response of TeO_2-based glasses is exclusively due to nonresonant processes. Nonresonant nonlinearities involve only distortions of the electron clouds, while resonant nonlinearities are produced by real electronic transitions. Therefore, nonresonant nonlinearities do not imply light attenuation, which implies the absence of power dissipation by absorption and fast response times, these making nonresonant nonlinear materials highly promising for the

[1] As it was shown in Chapter 2, for simplicity we will refer to $\left|\chi^{(3)}_{xxxx}\right|$ as $\chi^{(3)}$.

development of nonlinear optical devices.[11, 16, 18]

Values of $\chi^{(3)}$ of TTN and FTTN glasses have been measured at four wavelengths: 600, 800, 1200, and 1500 nm (Figure 5.1). At $\lambda = 1500$ nm, $\chi^{(3)}$ of the bulk glass is 3×10^{-13} esu, which is one order of magnitude larger than that of silica (1.8×10^{-14} esu), while in the case of the film $\chi^{(3)}$ is one order of magnitude larger (3×10^{-12} esu) than that of the bulk glass. $\chi^{(3)}$ remains approximately constant in both cases for wavelengths in the range from 1500 nm to 1200 nm to increase at smaller wavelengths ($\chi^{(3)}= 7 \times 10^{-13}$ esu and $\chi^{(3)}= 7 \times 10^{-12}$ esu at 600 nm for the bulk and film glasses respectively). The $\chi^{(3)}$ values of bulk glasses are smaller than those reported in the literature for ternary TeO_2–TiO_2–Nb_2O_5 glasses measured by third harmonic generation ($7 - 10 \times 10^{-13}$).[148]

The enhancement of the third order optical susceptibility at short wavelengths may be related to the contribution of resonant processes. $\chi^{(3)}$ is a complex magnitude in which the real part, $\mathrm{Re}(\chi^{(3)})$, is related to the nonlinear refractive index while the imaginary part, $\mathrm{Im}(\chi^{(3)})$, is related to the nonlinear absorption,[149] analogously to the relation between the complex refractive index, $\hat{n}$, with the refractive index, n, and the linear absorption coefficient, α.[12] Resonant processes contribute to the total absorption of the sample. Thus, a beam with intensity I

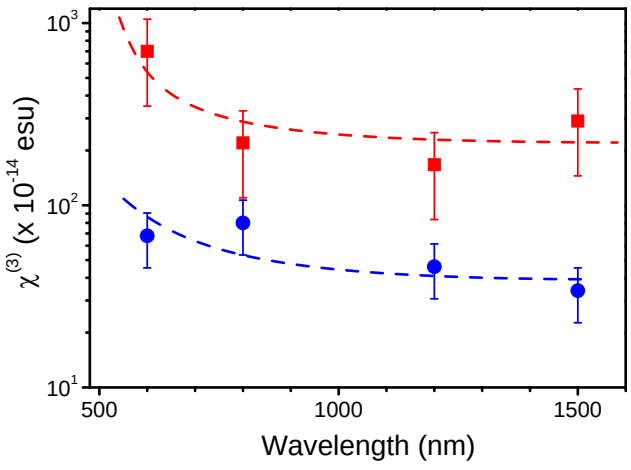

Figure 5.1: Dispersion of $\chi^{(3)}$ of (●) TTN bulk glass and (■) FTTN film glass. The dashed lines are a guide for the eyes.

propagating inside the sample will show an intensity evolution [12]:

$$\frac{dI}{dx} = -\left(\alpha I + \beta I^2\right) \tag{5.1}$$

where β is the nonlinear absorption coefficient, related to two-photon absorption (TPA) processes.[14, 16, 15] TPA involves a transition from the ground state of a system to a higher-lying state by the simultaneous absorption of two photons.[12] In the case of tellurite glasses, which show no absorption at wavelengths longer than that of the UV absorption edge, TPA should be non negligible for photon energies higher than half the energy gap ($2\hbar\omega \gtrsim E_g$) while at lower photon energies, *i.e.* larger wavelengths, nonresonant processes are exclusively responsible of the measured $\chi^{(3)}$ values.

The experimental technique used to determine $\chi^{(3)}$, DFMW, allows measuring the modulus of $\chi^{(3)}$ and thus, it is not possible to distinguish between the nonresonant (real) and resonant (imaginary) contributions to the measured $\chi^{(3)}$ values. The optical cutoff of TTN glass is 2.95 eV while the optical gap of FTTN is 3.49 eV, according to the data shown in Table 4.7. This implies that, TPA should be significant at wavelengths shorter than approximately 850 and 710 nm for the bulk and film glass respectively. Thus, the experimental $\chi^{(3)}$ values shown in Fig. 5.1 for wavelengths shorter than these values have a contribution associated to multiphotonic processes while the values measured at 1200 and 1500 nm are most likely nonresonant. Therefore, the negligible contribution of resonant processes at these wavelengths leads to lower experimental $\chi^{(3)}$ values than those measured at shorter wavelengths, as experimentally observed.

Apart from the evolution of $\chi^{(3)}$ with the wavelength, the most relevant experimental fact observed in the data shown in Fig. 5.1 is that the $\chi^{(3)}$ values of FTTN glass are one order of magnitude higher than those of TTN glass ($\chi^{(3)}{}_{\mathrm{FTTN}} \sim 10^{-12}$ esu while $\chi^{(3)}{}_{\mathrm{TTN}} \sim 10^{-13}$ esu). The linear optical response of TTN and FTTN glasses has also shown differences, as it was discussed in the previous chapter. However, in that case the values of n of the bulk glasses were always higher than those of film glasses, which was understood in terms of the lower density of films respect to bulk glasses. To illustrate this point, Figure 5.2 shows the dispersion of both the linear refractive index and the nonlinear optical susceptibility.

According to all the semi-empirical models developed to estimate the nonlinear optical response from the linear optical properties, such as the simple Miller's

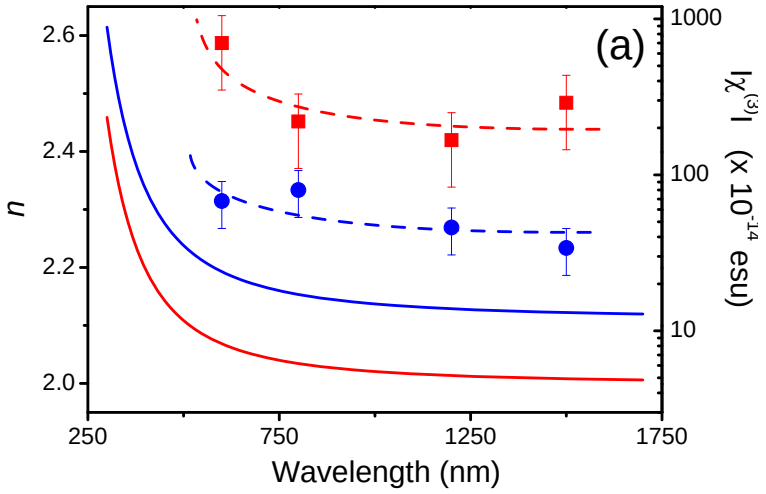

Figure 5.2: Dispersion of n and $\chi^{(3)}$ of (blue line, ●) TTN bulk glass and (red line, ■) FTTN film glass. The dashed lines are guides for the eyes.

rule ($\chi^{(3)} \propto n^4$),[16] the values of $\chi^{(3)}$ would scale with the values of the refractive index, that is the higher the refractive index the larger the value of $\chi^{(3)}$. However, the values measured for the FTTN glass seem to contradict this pseudoempirical rule.

This behavior cannot be explained by compositional differences with respect to the bulk glass since the compositional analysis has shown that cations have similar concentration and oxidation state in the film than in the bulk glasses. In fact, the exact origin of the nonlinearity of tellurite glasses is still object of active research. The high hyperpolarizability of TeO_2 has been attributed to the empty $5d$ orbitals [101] or to the electron lone pair at the Te atom,[102] while recent *ab initio* calculations have also related the hyperpolarizability of TeO_2 glass to electron delocalization in $(TeO_2)_n$ chain-like structures, which suggests that the enhancement of the nonlinear response may be related to structural factors.[103]

These possible structural factors responsible for the increase of the nonlinear optical response should be reflected in the glass network structure, that we have studied by Raman spectroscopy. Figure 5.3 compares the Raman spectra of TTN and FTTN glasses. The general shape is similar in both cases, but the band at 700 – 800 cm^{-1}, related to NBO, shows a higher relative intensity in the case of FTTN than in that of TTN, while the peak at 470 cm^{-1}, related to Te-O-Te linkages, is less intense in the case of the film. These differences are similar to

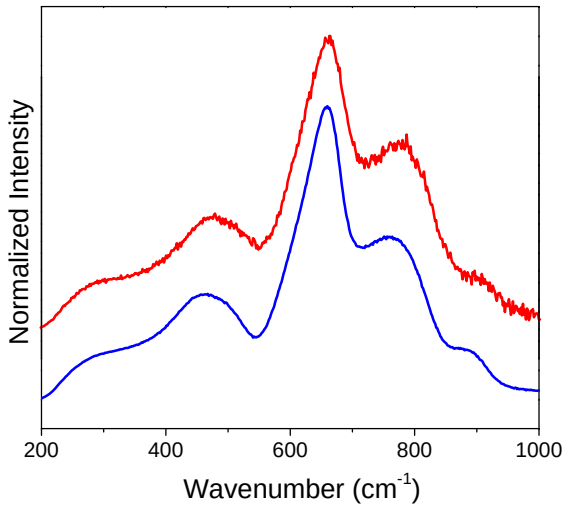

Figure 5.3: Raman spectra of (blue line) TTN and (red line) FTTN glasses.

those reported between liquid TeO_2 and TeO_2 glass,[150] although they are less obvious in our case. As it has been discussed in Chapter 4, these results suggests that the film glass network is more disordered than that of bulk glass and it involves short TeO_2 chains with a high concentration of terminal Te-O bonds, acting as NBO.

These structural characteristics may have opposite effects on the nonlinear response: according to ref. [103], the slightly shorter length of TeO_2 chains in the films should reduce their $\chi^{(3)}$, while the increase of the concentration of terminal Te-O bonds contributes to a larger concentration of highly polarizable NBO and thus, to an increase of $\chi^{(3)}$, as it has been shown in the case of SiO_2- and B_2O_3-based glasses.[100, 151] Thus, in order to determine the dominant mechanism in the case of the film glass, we have thermally annealed the film glass samples, since thermal annealing should allow the glass network structure to relax and become more similar to that of bulk glass. For that purpose a FTTN glass was divided into two different samples: FTTN1 and FTTN2. The first was an as-grown FTTN glass, while the second was annealed in air at T = 350 °C for 90 minutes. Table 5.1 shows the $\chi^{(3)}$ values of both film samples and of the TTN bulk glass. $\chi^{(3)}$ of the annealed sample is one order of magnitude smaller when compared to that of the as-grown sample, and similar, within the experimental error, to that of the bulk glass. This result clearly supports the structural origin of the enhancement of the film glass nonlinear response.

Sample	Characteristics	$\chi^{(3)}$ at 1500 nm $\times 10^{-14}$ esu
FTTN1	As-grown	300 ± 150
FTTN2	Annealed at 350 °C, 90 min.	30 ± 20
TTN	Bulk glass	34 ± 11

Table 5.1: Values of $\chi^{(3)}$ measured at 1500 nm of a FTTN film glass before (FTTN1) and after (FTTN2) a thermal treatment. The $\chi^{(3)}$ value of the original $90TeO_2 \cdot 5TiO_2 \cdot 5Nb_2O_5$ bulk glass is also shown.

The structure of the annealed FTTN2 sample has been also characterized by Raman spectroscopy and compared to that of FTTN1 and TTN glasses (Figure 5.4a). The Raman spectrum of FTTN2 is intermediate between those of FTTN1 and TTN glasses. The relative intensity of the NBO band at 700 – 800 cm^{-1} is smaller than in the case of FTTN1, but is still higher than in the TTN glass. Another difference can be observed in the Te-O-Te peak at 470 cm^{-1}. This peak has a higher intensity in the case of FTTN1 when compared to FTTN2, and it is centered at the same position in the FTTN2 and TTN samples, while it is slightly shifted towards higher wavenumbers in the as-grown FTTN1 film glass.

In order to have precise information of the structure of film glasses, their

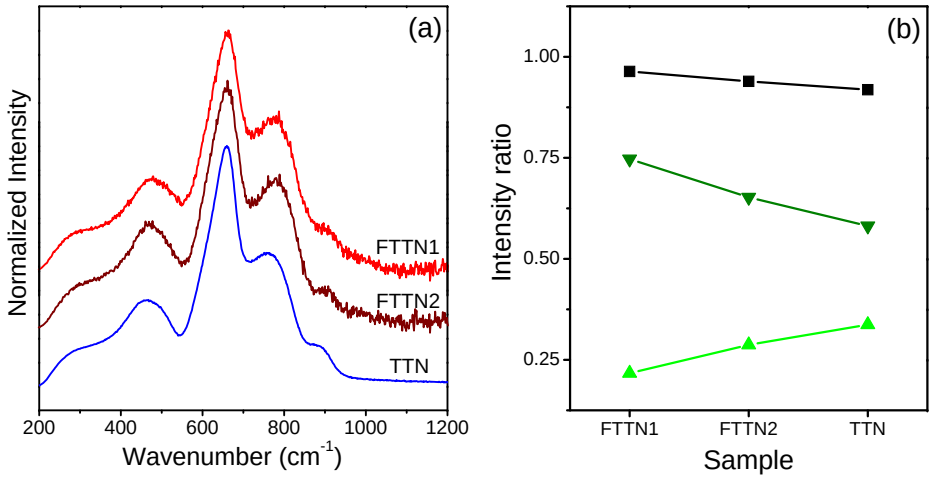

Figure 5.4: (a) Raman spectra of an as-grown FTTN1 film glass, an annealed FTTN2 film glass, and a TTN bulk glass. (b) Ratio between the intensities of the deconvoluted peaks related to NBO (I_E and I_F) and the main peak at 660 cm^{-1} (I_D): (■) $\frac{I_E+I_F}{I_D}$, (▲) $\frac{I_E}{I_D}$, and (▼) $\frac{I_F}{I_D}$.

Raman spectra have been deconvoluted and compared to the deconvolution of the bulk glass spectrum (Table 3.2). Figure 5.4b shows the ratio between the sum of the intensities of the two deconvoluted peaks E and F, related to NBO, and the main peak at 660 cm^{-1} (peak D). This ratio, previously used in Chapters 3 and 4, gives an estimation of the fraction of NBO in the glass network. As expected from the above discussion, the ratio slightly decreases when the sample is annealed, approaching the value of the bulk glass.

Since this small change does not reflect well the differences seen in the Raman spectra of the three glasses (Fig. 5.4a), we have also analyzed independently the intensity ratio of peaks E and F. According to the deconvolution made in Chapter 3, peak E at 720 and peak F at 780 cm^{-1} take into account the vibration of the bond Te-O, with the oxygen atom being a NBO. The difference between them is the interaction of the NBO with other surrounding Te atoms, which is stronger in the case of peak E. The ratios $\frac{I_E}{I_D}$ and $\frac{I_F}{I_D}$ show opposite trends, the first increases while the second decreases when the sample is annealed, although the ratios are closer to that of the bulk glass in the case of the annealed film.

This result clearly shows an structural transformation when the film is annealed. Initially, as-grown film has a large fraction of NBO with little interaction with surrounding Te atoms. The results suggest that the glass network rearranges during thermal treatment. This brings closer the Te atoms to NBO, increases the fraction of NBO with strong interaction with the surrounding Te atoms and leads to a glass network closer to that of bulk glasses obtained by traditional melting methods. Therefore, the structural changes induced during the deposition of film FTTN1 should be responsible of the enhanced nonlinear optical response. We then propose that NBO with little interaction with surrounding Te atoms are less polarized and thus, they have higher polarizability than NBO with strong interaction with Te atoms, increasing the nonlinear response of the film glass.

5.1.2 $\chi^{(3)}$ values of TWR- and TWPb-series glasses

In the previous section we have discussed the effect on the nonlinear optical response of the structural changes induced in the film glass during the deposition process for the case of TTN glasses. Now, we study the third order optical susceptibility of tellurite glasses with different compositions in the systems TeO_2–WO_3–R_xO_y and TeO_2–WO_3–PbO in order to further support the interpretation given in the previous section.

In this case, we limit the measurements of $\chi^{(3)}$ to wavelengths in which the nonlinear response is due to nonresonant processes. In particular, we are interested in the values of $\chi^{(3)}$ at 1500 nm since this wavelength is very close to the third window of optical telecommunications. However, it has not been possible to measure $\chi^{(3)}$ at this wavelength in all cases due to experimental problems associated with the low light intensity available at 1500 nm in the experimental setup used for DFWM. Thus, we have also considered 1300 nm, since there is no dispersion of $\chi^{(3)}$ values for wavelengths longer than 1000 nm, as we have shown in Fig. 5.1. We then expect that the measured values at 1500 and 1300 nm are very similar. Table 5.2 shows the values of $\chi^{(3)}$ for TWR- and TWPb-series bulk and film glasses. In the first case, the measurements could be made at 1500 nm, while in the second case the samples were measured at 1300 nm. Moreover, due to the complexity of measuring $\chi^{(3)}$ of thin film glasses, only film glasses with representative compositions were measured.

Figure 5.5 shows the $\chi^{(3)}$ values of representative TWR-series bulk and film glasses as a function of the real part of the linear refractive index of bulk glasses. All the bulk glasses have similar $\chi^{(3)}$ values ($\sim 1 \times 10^{-12}$ esu) with the exception of the sample with the lowest refractive index, TWLa, which has also a slightly lower $\chi^{(3)}$ value (6×10^{-13} esu). The $\chi^{(3)}$ values of film glasses are the same,

Bulk glass	$\chi^{(3)}$ $\times 10^{-14}$ esu	Film glass	$\chi^{(3)}$ $\times 10^{-14}$ esu
TW15	120 ± 40	FTW15	120 ± 60
TWTi	90 ± 30	FTWTi	-
TWNb	70 ± 30	FTWNb	120 ± 60
TWTa	110 ± 40	FTWTa	180 ± 90
TWLa	60 ± 20	FTWLa	60 ± 30
TWBi	130 ± 40	FTWBi	120 ± 60
TWPb	130 ± 40	FTWPb	220 ± 110
TWPb1	110 ± 40	FTWPb1	110 ± 60
TWPb2	60 ± 20	-	-
TWPb3	80 ± 30	FTWPb3	180 ± 90
TWPb4	80 ± 30	-	-
TWPb5	60 ± 20	-	-
TWPb6	60 ± 20	FTWPb6	110 ± 60
TWPb7	100 ± 30	-	-
TWPb8	90 ± 30	FTWPb8	210 ± 100
TWPb9	100 ± 30	FTWPb9	270 ± 140
TWPb10	80 ± 30	FTWPb10	390 ± 190

Table 5.2: Third order optical susceptibility measured at 1500 nm for TeO_2–WO_3–R_xO_y and at 1300 nm for TeO_2–WO_3–PbO bulk and film glasses.

within the experimental error, as those of the respective bulk glasses. In the case of TWPb-series, Figure 5.6 shows the $\chi^{(3)}$ values of representative bulk and film glasses as a function of their TeO_2 molar content. In spite of the large compositional differences, bulk glasses have also similar $\chi^{(3)}$ values ($\sim 8 \times 10^{-13}$ esu), while film glasses, which have lower TeO_2 molar contents than those of bulk glasses, as it was shown in Fig. 4.13, have slightly larger $\chi^{(3)}$ values. The $\chi^{(3)}$ values of bulk glasses are in good agreement with those summarized by Dimitrov *et al.* [21] for binary TeO_2–TiO_2, TeO_2–Nb_2O_5, TeO_2–Ta_2O_5, and TeO_2–PbO glasses measured by third harmonic generation.

The $\chi^{(3)}$ values of bulk glasses summarized in Table 5.2 are approximately three times larger than that of the $90TeO_2 \cdot 5TiO_2 \cdot 5Nb_2O_5$ bulk glass (3×10^{-13}). This increase is most likely related to compositional differences, namely the presence of highly polarizable W^{6+} cations. Lines [18, 101] studied the nonlinear response of TM oxides, concluding that virtual transitions from the valence band to the empty cationic *d* orbital are responsible for the large third order optical susceptibilities shown by TM oxides. This effect is larger as we progress along the TM series and thus, he pointed out WO_3 as one of the most promising oxides for obtaining glasses with large nonlinearities. The experimental results shown in the present chapter confirm that hypothesis. However, further variations of $\chi^{(3)}$ with the composition within the two experimental series cannot be established due to the large experimental uncertainty ($\sim 30\%$) in the measurements. Moreover, heavy metal (HM) oxides like PbO or Bi_2O_3, which lead to high refractive indexes due to their large polarizability (Chapter 3), must also contribute to the largest nonlinearities measured (1.3×10^{-12} esu).

Regarding the nonlinear response of film glasses, TWR- and TWPb-series film glasses show $\chi^{(3)}$ values that are of the same order of magnitude than that of FTTN film glass ($\sim 10^{-12}$ esu). However, while in the latter case the as-grown film glass showed an enhancement of $\chi^{(3)}$ of one order of magnitude with respect to the bulk glass, now film glasses have $\chi^{(3)}$ values that are similar or only slightly larger than those of bulk glasses.

We have attributed the large enhancement of $\chi^{(3)}$ in FTTN glass to its larger NBO fraction when compared to the bulk glass. Since TWR- and TWPb-series films show the same structural peculiarities than FTTN films, it should be expected a similar enhancement of $\chi^{(3)}$ that is not experimentally observed. In order to explain this apparent contradiction, we need to have in mind the different nonlinear mechanisms present in glasses. In conventional glasses, such as

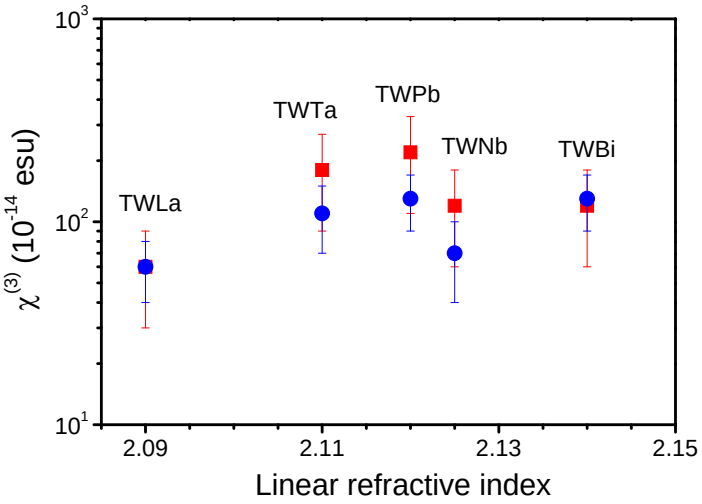

Figure 5.5: Third order optical susceptibility measured at 1500 nm for representative (●) bulk and (■) film glasses belonging to the system TeO_2–WO_3–R_xO_y as a function of the real part of the linear refractive index of bulk glasses.

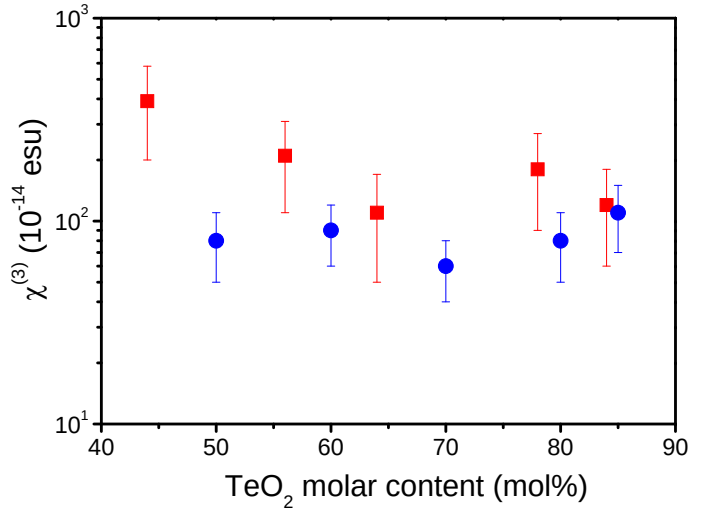

Figure 5.6: Third order optical susceptibility measured at 1300 nm for representative (●) bulk and (■) film glasses belonging to the system TeO_2–WO_3–PbO as a function of the TeO_2 molar content.

SiO_2-based glasses, the origin of the nonlinear optical response is associated to the hyperpolarizability of the oxygen bonds.[13, 100] For example, Nasu *et al.* [152] estimated that the hyperpolarizability of NBO in SiO_2-based bulk glasses is 1.5 times larger than that of bridging oxygens. However, in the case of high refractive index glasses such as tellurite glasses or those containing TM or HM oxides, the dominant contribution is that related to the large hyperpolarizability of cations.[13, 16, 18, 100] Thus, in principle we can considerer two different contributions to the nonresonant $\chi^{(3)}$:

$$\chi^{(3)} \sim \chi^{(3)}_{cat} + \chi^{(3)}_{str} \tag{5.2}$$

where $\chi^{(3)}_{cat}$ and $\chi^{(3)}_{str}$ are related to contributions associated to the hyperpolarizability of cations and to structural factors respectively. In the case of conventional glasses the second factor would be dominant, while in high refractive index glasses the first one would be the most important.

From the compositional analysis (Figs. 4.12 and 4.13) we have concluded that the film composition is very similar in bulk and film glasses, and no changes of the oxidation state were observed. Therefore, $\chi^{(3)}_{cat}$ should be equal in film and bulk glasses, and the possible differences in $\chi^{(3)}$ should only arise from $\chi^{(3)}_{str}$.

In the case of the TeO_2–TiO_2–Nb_2O_5 glasses considered before, the value of $\chi^{(3)}$ measured for the bulk glass was $\sim 3 \times 10^{-13}$ esu, while that of the film glass was $\sim 3 \times 10^{-12}$ esu. The observed increase has been related to structural factors, *i.e.* an enhancement of the $\chi^{(3)}_{str}$ contribution. The reason why structural factors are relevant in this case is the synthesis method used to deposit the film glasses. Films have been synthesized in experimental conditions far from that of traditional melting synthesis. PLD allow us to produce films with large fractions of NBO without introducing significant compositional changes, while in bulk glasses it is necessary to introduce a significant amount of network modifiers in order to achieve similar NBO fractions. From these results we can concluded that $\chi^{(3)}_{str}$ associated to the large NBO fraction in FTTN glasses could be as large as $\sim 10^{-12}$ esu.

In the case of TeO_2–WO_3–R_xO_y and TeO_2–WO_3–PbO glasses, the situation is slightly different. According to our previous reasoning, the increase of $\chi^{(3)}$ associated to the NBO fraction should contribute to the nonlinear response with a value of $\chi^{(3)}_{str} \sim 10^{-12}$. However, since bulk glasses have a large content of TM and HM oxides, the contribution to $\chi^{(3)}$ related to the composition, $\chi^{(3)}_{cat}$, is

$\sim 10^{-12}$ esu, one order of magnitude larger than the value measured for TTN bulk glass. Therefore, in the TWR- and TWPb-series film glasses both structural and compositional contributions to $\chi^{(3)}$ are of the same order of magnitude ($\sim 10^{-12}$ esu), which correspond to the values measured both for bulk and film glasses.

To sum up, the nonlinear optical response of tellurite glasses is mainly determined by the large hyperpolarizability of Te^{4+}, TM, and HM cations, although in the case of film glasses, additional structural factors, namely a large fraction of NBO, allow enhancing the values of $\chi^{(3)}$ up to one order of magnitude in certain cases (TTN). The acquired know-how in the characterization of the structure and composition, and the relation between them and the optical properties of tellurite glasses, allow us to understand the optical response of other glass systems. In particular, the next section is focussed on the interpretation of the linear and nonlinear optical response of Nb_2O_5–PbO–GeO_2 bulk and film glasses.

5.2 Nonlinear optical properties of Nb_2O_5–PbO–GeO_2 glasses

In previous works, the Laser Processing Group [49, 50, 153] has produced thin film glasses belonging to the system Nb_2O_5–PbO–GeO_2. The most important result of these works was the deposition of transparent thin film glasses with very large Nb_2O_5 and PbO molar contents that are either opaque crystalline or opal vitreous when synthesized by traditional melting techniques. The glass forming region in the Nb_2O_5–PbO–GeO_2 system is limited to compositions with at least 25 mol% of PbO and 25 mol% of GeO_2 (Figure 5.7). Moreover, the composition of transparent glasses is even more limited, and they could only be produced for molar contents of GeO_2 larger than 50 mol%. In the case of thin films, transparent film glasses were produced in a much broader compositional range, which was related to the high instantaneous deposition rates involved in the PLD process, discussed in previous chapters, as they favor the formation of metastable material phases.[49]

The atomic composition of bulk and film samples was analyzed using ion beam techniques, while the linear optical response was characterized by the refractive index and the optical gap. Regarding the film composition, the cationic content of films deposited in the optimum conditions was found to be similar to that of bulk targets but films deposited in the optimum conditions were always oxygen

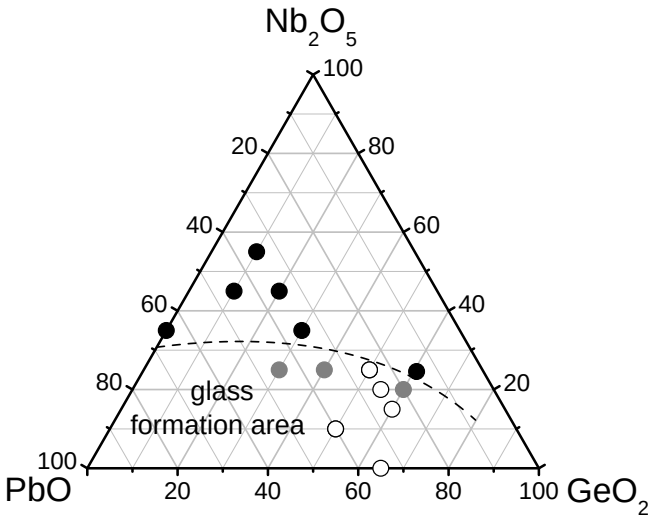

Figure 5.7: Molar Composition in mol% of the Nb_2O_5–PbO–GeO_2 bulk samples considered in the present section: (●) opaque crystalline, (●) opal and (○) transparent glasses. The dashed line indicates the approximate bulk glass forming region.

deficient (10 – 15%).[49, 50] The possibility of producing transparent films glasses in such a large compositional range was demonstrated to have a fundamental effect on the optical properties. Figure 5.8 shows the refractive index and optical gap as a function of the sum of the relative atomic contents of Nb and Pb, calculated according to:

$$[\mathrm{X}] = \frac{N_{\mathrm{X}}}{N_{\mathrm{Nb}} + N_{\mathrm{Pb}} + N_{\mathrm{Ge}}} \tag{5.3}$$

with X = Nb or Pb, and N_{X} the number of atoms per unit of area of the element X measured by ion beam techniques (RBS and NRA). The values of n measured at 630 nm (Fig. 5.8a) increase linearly with [Nb]+[Pb] up to values of 2.35 for a film without GeO_2. As a comparison, the composition range in which transparent bulk targets were produced is indicated in the figure. It is clearly seen that the use of nontransparent targets combined with PLD make accessible the synthesis of films with higher refractive indexes. Fig. 5.8b shows the evolution of E_g as a function of the [Nb]+[Pb] content. In this case, E_g does not change significantly as [Nb] increases (with [Pb] constant), while it decreases linearly as [Pb] increases (with [Nb] constant).

These results clearly demonstrate the strong effect of the deposition process and the final film composition on the optical properties of Nb_2O_5–PbO–GeO_2

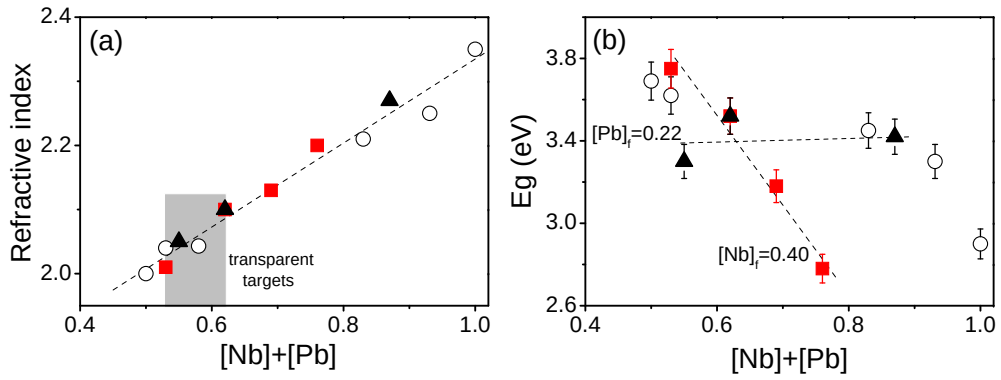

Figure 5.8: (a) Linear refractive index and (b) optical gap of films belonging to the system Nb_2O_5–PbO–GeO_2 as a function of the sum of the relative atomic contents of Nb and Pb. Results corresponding to a series of films with (▲) [Pb] = 0.22 or (■) [Nb] = 0.40 are highlighted. The dashed lines are linear fits of the dependence of (a) n and (b) Eg on [Nb]+[Pb] for the series of films with constant [Pb] or [Nb]. The composition range in which transparent bulk targets are produced is indicated in (a). Figure adapted from ref. [49].

film glasses. Moreover, the results regarding the optical properties of tellurite film glasses, discussed through this thesis, have shown the fundamental role that composition and structure play in the optical response. In the present section, the third order optical susceptibility of Nb_2O_5–PbO–GeO_2 glasses is systematically studied, and its structural and compositional origin discussed.

5.2.1 $\chi^{(3)}$ values of NPG-series samples

Among all the film and bulk glasses shown in Fig. 5.7 and 5.8, we have selected four compositions (NPG-series), with increasing Nb_2O_5 molar contents in the range from 15 mol% to 55 mol% to study the evolution of $\chi^{(3)}$. Nb^{5+}, like W^{6+}, is an empty d orbital TM cation with a short Nb-O bond distance in the Nb_2O_5 molecule.[101] Thus, it is expected that the increase of the Nb_2O_5 molar content leads to obtain larger nonlinear refractive indexes.[154] Table 5.3 shows the NPG-series bulk and film samples, the nominal molar composition of the bulk samples, and the experimentally measured relative atomic content of each sample. NPG1 and NPG2 are transparent bulk glasses, while NPG3 and NPG4 are opaque crystalline bulk samples.

The third order optical susceptibility has been characterized at a wavelength

Sample	Nominal molar composition	Relative atomic composition [Nb]	[Pb]	[Ge]	[O]
NPG1	$15Nb_2O_5 \cdot 25PbO \cdot 60GeO_2$	0.26	0.22	0.52	1.91
FNPG1	-	0.24	0.29	0.47	1.68
NPG2	$25Nb_2O_5 \cdot 25PbO \cdot 50GeO_2$	0.40	0.20	0.40	2.00
FNPG2	-	0.39	0.23	0.38	1.80
NPG3	$35Nb_2O_5 \cdot 35PbO \cdot 30GeO_2$	0.52	0.26	0.22	2.00
FNPG3	-	0.54	0.29	0.17	1.72
NPG4	$55Nb_2O_5 \cdot 35PbO \cdot 10GeO_2$	0.71	0.23	0.06	2.13
FNPG4	-	0.71	0.23	0.07	1.72

Table 5.3: Molar composition and relative atomic content of NPG-series bulk and film samples.

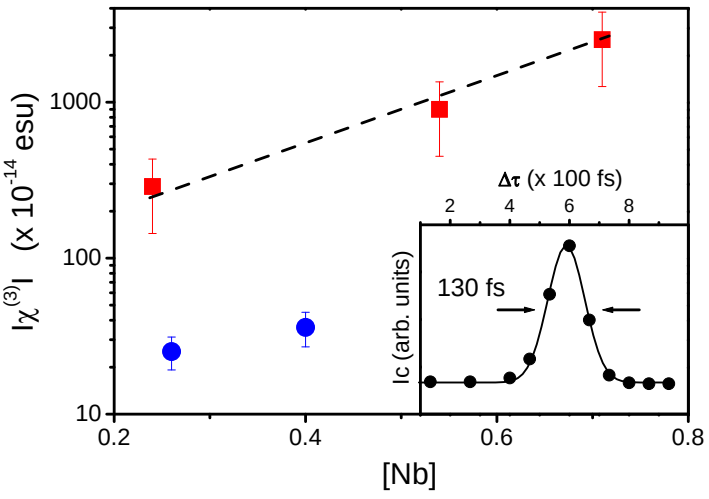

Figure 5.9: Values of $\chi^{(3)}$ measured at 800 nm as a function of the relative atomic content of Nb for (■) film and (●) transparent bulk glasses. The dashed line is a guide for the eyes. The inset shows the build up time of the conjugated signal measured by DFWM in a $15Nb_2O_5 \cdot 25PbO \cdot 60GeO_2$ bulk glass.

of 800 nm. Figure 5.9 shows the $\chi^{(3)}$ values of the transparent samples included in Table 5.3 as a function of the relative atomic content of Nb. $\chi^{(3)}$ increases as [Nb] increases both in the bulk and film glasses, thus confirming the fundamental role that Nb atoms play in the nonlinear response of the glass. In the case of bulk samples, only $\chi^{(3)}$ of transparent glasses could be measured, and the values obtained are up to 20 times larger than $\chi^{(3)}$ of SiO_2. In the case of film glasses, $\chi^{(3)}$ is one order of magnitude larger than that of the corresponding transparent bulk glasses, while films with large Nb atomic contents deposited from nontransparent samples have $\chi^{(3)}$ values as large as 2.5×10^{-11}. Table 5.4 summarizes the measured values of n and $\chi^{(3)}$ at 800 nm.

According to the values of the optical gap shown in Fig. 5.8b, the limit condition for two photon absorption to occur, given by $2\hbar\omega \gtrsim E_g$ is not satisfied here since the photon energy at 800 nm is $\hbar\omega = 1.55$ eV and E_g is $\geq$ than 3.4 eV for the film glasses considered. Therefore, measured $\chi^{(3)}$ values must have an exclusively nonresonant origin. This has been confirmed by measuring the build-up time of the nonlinear response. The extremely fast ($\sim$ 130 fs) buildup time observed in our case, as illustrated in the inset of Fig. 5.9, allows us to discard nonlinear absorptive contributions to $\chi^{(3)}$.

Since the increase of $\chi^{(3)}$ of film glasses with respect to that of bulk glasses is not related to resonant processes, it must have its origin in the compositional or structural modifications induced in the films during their deposition. As in the case of tellurite glasses, we have completed the previous compositional analysis of films samples by using XPS and performed a deep structural characterization of both vitreous and crystalline samples by Raman spectroscopy, in order to explain both the linear and nonlinear optical properties of NPG-series films.

Sample	n	$\chi^{(3)}$ $\times 10^{-14}$ esu
NPG1	1.97	25 ± 6
FNPG1	2.02	290 ± 150
NPG2	2.05	36 ± 9
FNPG2	2.07	-
NPG3	-	-
FNPG3	2.14	900 ± 450
NPG4	-	-
FNPG4	2.24	2500 ± 1300

Table 5.4: Linear refractive index and third optical order susceptibility measured at 800 nm of NPG-series film and bulk samples.

5.2.2 Composition of NPG-series samples

According to the data shown in Tables 5.3 and 5.4, films have similar cationic contents and are oxygen deficient (10 – 15%) when compared to bulk samples, while they show larger n and $\chi^{(3)}$ values. This behavior is opposite to what is observed in the case of TeO_2-based film glasses deposited using the optimum conditions (Chapter 4). In the present case, the oxygen deficiency of the films and their high refractive indexes may indicate the presence of cations in a reduced oxidation state, as observed for tellurite film glasses deposited outside the optimum conditions.

The oxidation state of cations in film and bulk samples has been determined by XPS. Figure 5.10a shows the Nb $3d$ core-level spectrum of the NPG1 bulk glass. The peaks at 206.9 and 209.6 eV correspond to the Nb^{5+} $3d_{5/2}$ and $3d_{3/2}$ levels, respectively. Instead, the spectra obtained for films glasses show broader peaks, as illustrated by the spectra of FNPG1 (Fig. 5.10b) and FNPG3 (Fig. 5.10c) film glasses. The spectrum of FNPG1 shows only a broad peak, that is compatible with the presence of additional bands associated to the presence of Nb^{4+} peaking at 205.7 ($3d_{5/2}$) and 208.5 eV ($3d_{3/2}$). The spectrum for FNPG3 films has two peaks, that are broader and shifted to lower energies than in the case of the NPG1 bulk glass, indicating that Nb^{4+} bands are the most intense. Nb^{4+} bands are observed in all films, the only difference being the relative intensity of the Nb^{5+} and Nb^{4+} contributions. The fraction of Nb^{4+} is above 50% in all cases, and it increases with the heavy metal fraction. Nb^{4+} is forming NbO_2, which explains the oxygen deficiency.

Finally, a possible reduction of Pb or Ge has been discarded by analyzing the most intense Pb $4f_{7/2}$ and Ge $2p_{3/2}$ levels. Only Pb^{2+} and Ge^{+4} were found both in bulk or film glasses, with binding energies of 137.5 and 1219.3 eV, respectively.

5.2.3 Structure of NPG-series samples

The results obtained in the case of tellurite film glasses have shown that structural factors, such as the film density or the fraction of NBO, determine the optical response. In the case of the Nb_2O_5–PbO–GeO_2 glass system, the production of transparent glass films outside the compositional glass forming region suggests that the structure of film and bulk samples has to be strongly different. In this section, these structures have been characterized by Raman spectroscopy. First, we characterize the basic structural units composing the network of bulk vitreous

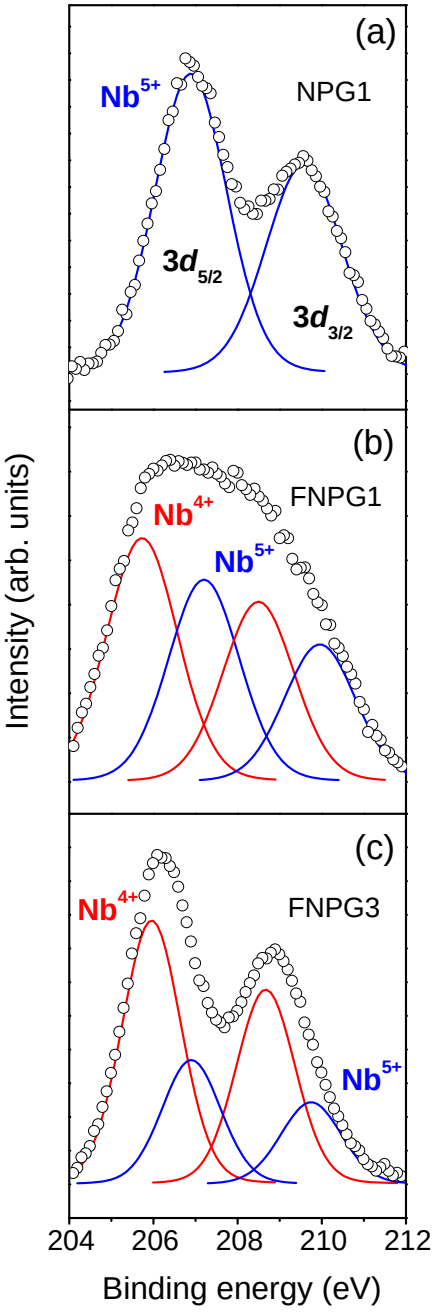

Figure 5.10: Nb $3d$ core-level spectra of NPG1, FNPG1, and FNPG3 samples. Red and blue lines correspond to simulated Nb^{5+} and Nb^{4+} bands, respectively.

and crystalline samples, and then the film glass network is compared to that of bulk samples.

Figure 5.11 shows the Raman spectra of the NPG-series bulk samples. The deconvolution of the spectra or the band assignment to the characteristic vibrations of the different structural units is more complicated than in the case of tellurite glasses, due to the large compositional differences among the samples studied and the different phases in which the bulk samples are produced (transparent glasses, opal glasses, or crystals). In particular, the presence of GeO_2 and Nb_2O_5 is knonw to lead to vibrational bands in the range 400 – 900 cm^{-1},[155, 156, 157] while bands associated with PbO appear at low frequencies ($\lesssim$ 350 cm^{-1}).[155, 157] These low frequency vibrational modes associated with PbO have been already seen and discussed for TeO_2–WO_3–PbO glasses in Chapter 3.

In order to distinguish between the vibrational modes of GeO_2 and Nb_2O_5, and thus determine their effect on the glass network structure, two additional binary samples with compositions $35PbO \cdot 65GeO_2$ (NPG5) and $35Nb_2O_5 \cdot 65PbO$ (NPG6) have been synthesized. Obviously, all the bands at high frequencies in the samples NPG5 and NPG6 must be related only to vibrations of structural units of GeO_2 or Nb_2O_5, respectively. The Raman spectra of these samples are also included in Fig. 5.11.

The sample NPG5, which has the largest GeO_2 molar content (65 mol%), is a glass and its Raman spectrum is characterized by two main bands: a very broad band at 350 – 550 cm^{-1} and a narrow band centered at 810 cm^{-1}. The basic structural unit of GeO_2-based glasses is the [GeO_4] tetrahedron.[157] The low frequency band is related to a glass network composed of bridging Ge-O-Ge linkages,[155] while the high wavenumber band is assigned to stretching vibrations of Ge-O bonds in [GeO_4] tetrahedra. The latter band is, in fact, a combination of the vibration modes of [GeO_4] units with a different number of NBO.[157] The frequency of the vibration mode decreases as the number of NBO surrounding the Ge increases, and thus, the addition of network modifiers, which increases the number of NBO, shifts the peak towards lower wavenumbers.

In the spectrum of the ternary glass NPG1, with a similar GeO_2 molar content to that of NPG5 (60 and 65 mol%, respectively), the peak at high wavenumbers is broader than in the case of NPG5, and it is shifted toward lower frequencies (780 cm^{-1}), whereas the intensity of the band at low frequencies (470 cm^{-1}) strongly diminishes. These differences can be understood by the addition of Nb_2O_5. The decrease of the intensity of the low wavenumber band is associated with the

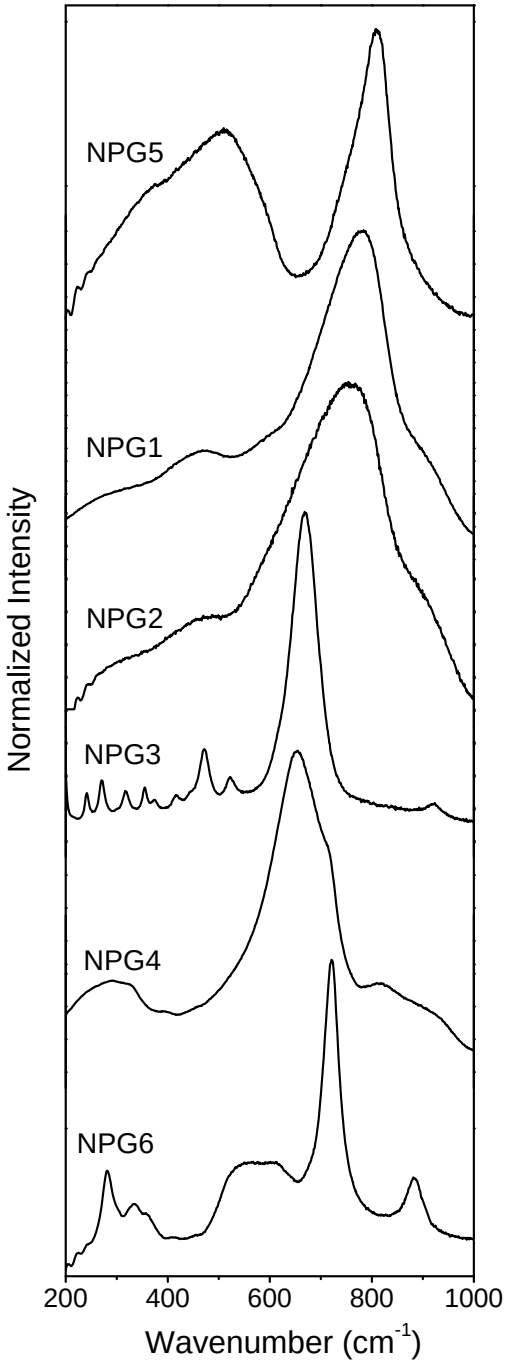

Figure 5.11: Raman spectra of Nb_2O_5–PbO–GeO_2 bulk samples, ordered according to their GeO_2 molar content (from NPG5, with 65 mol%, to NPG6 with 0 mol%).

cleavage of Ge-O-Ge linkages, which increases the number of NBO and shifts the high wavenumber peak towards lower frequencies.[158] Moreover, the addition of Nb_2O_5 leads to the appearance of two shoulders at 575 and 850 cm^{-1} in the main peak. The first is assigned to vibrations of slightly distorted [NbO_6] octahedral structural units without NBO,[154, 156, 159] while the second is assigned to highly distorted [NbO_6] octahedra with NBO.[117, 119, 156, 160] The latter is also present in the case of TeO_2–TiO_2–Nb_2O_5 glasses (Fig. 3.8 and Table 3.2)

As the GeO_2 molar content decreases (glass NPG2), the position of the peak related to [GeO_4] units continues shifting towards lower wavenumbers and broadening, indicating an even larger fraction of NBO. The shoulder at 575 cm^{-1}, related to [NbO_6] octahedral structural units, becames more intense. The assignment of this shoulder is confirmed by the spectrum of the crystalized NPG3 and the opal NPG4 samples. The spectrum of NPG3 is characterized by a sharp peak at 670 cm^{-1} that we assigned to the vibrations of slightly distorted [NbO_6] octahedra. The spectrum of NPG4, which has a very low GeO_2 molar content (10 mol%), shows the same main peak, but broader in this case due to a shoulder at high wavenumbers.

Finally, the effect of Nb_2O_5 on the glass network has been confirmed with the help of the spectrum of the opal sample NPG6 that contains only Nb_2O_5 and PbO. This spectrum has several bands at high wavenumbers related to Nb_2O_5: a wide weak band at 500 – 650 cm^{-1} and two peaks, one intense at 720 cm^{-1} and another weak at 880 cm^{-1}. The band at 500 – 650 cm^{-1} and the weak band at 880 cm^{-1} have been previously discussed in the spectra of NPG1 glass and they are present in all the samples containing Nb_2O_5. The low frequency band is related to a three-dimensional network formed by slightly distorted [NbO_6] octahedra, whereas the high frequency band is assigned to vibrations of isolated [NbO_6] octahedral structural units.[154, 156, 159] Finally, the sharp peak at 720 cm^{-1} is associated with Nb-O vibrations in lead niobate crystals.[161, 162] This peak is also present in the NPG4 spectrum as a shoulder at 700 – 750 cm^{-1} of the main peak. The band assignment is summarized in Table 5.5.

Since all the film samples are vitreous, they must show important structural differences when compared to bulk samples that have to be reflected in their Raman spectra. Figure 5.12 shows the Raman spectra of bulk and film glasses in the range 300 – 900 cm^{-1}. All the film spectra are typical of vitreous samples, without the sharp peaks observed in the case of crystalline samples such as NPG3. In all cases the dominant feature is a wide intense band at 700 – 900 cm^{-1}, and

Sample	Band position (cm^{-1})	Assignment
NPG5	325 – 400 (S)	Vibrational modes of Pb-O bonds
	430 – 550	Ge-O-Ge bridging linkages
	700 – 850	Stretching vibration of Ge-O bonds in $[GeO_4]$ tetrahedra
NPG1	200 – 400 (S)	Vibrational modes of Pb-O bonds
	400 – 520	Ge-O-Ge bridging linkages
	550 – 625 (S)	Slightly distorted $[NbO_6]$ octahedra
	750 – 850	Stretching vibration of Ge-O bonds in $[GeO_4]$ tetrahedra
	850 – 950 (S)	Highly distorted $[NbO_6]$ octahedra
NPG2	200 – 400 (S)	Vibrational modes of Pb-O bonds
	400 – 500	Ge-O-Ge bridging linkages
	550 – 650 (S)	Slightly distorted $[NbO_6]$ octahedra
	650 – 850	Stretching vibration of Ge-O bonds in $[GeO_4]$ tetrahedra
	850 – 950 (S)	Highly distorted $[NbO_6]$ octahedra
NPG3	200 – 400	Vibrational modes of Pb-O bonds
	620 – 700	Slightly distorted $[NbO_6]$ octahedra
	880 – 950	Highly distorted $[NbO_6]$ octahedra
NPG4	250 – 350	Vibrational modes of Pb-O bonds
	600 – 700	Slightly distorted $[NbO_6]$ octahedra
	700 – 750 (S)	Nb-O vibrations in lead niobate crystals
	850 – 950	Highly distorted $[NbO_6]$ octahedra
NPG6	250 – 350	Vibrational modes of Pb-O bonds
	500 – 650	Slightly distorted $[NbO_6]$ octahedra
	690 – 750	Nb-O vibrations in lead niobate crystals
	840 – 920	Highly distorted $[NbO_6]$ octahedra

Table 5.5: Band assignment in the Raman spectra of bulk Nb_2O_5–PbO–GeO_2 samples shown in Fig. 5.11. Bands that are shoulders of intense bands are indicated by (S).

the differences with respect to bulk samples are more marked as the GeO_2 molar content decreases.

Films FNPG1 and FNPG2, deposited from bulk glasses with a large GeO_2 molar content ($\gtrsim$ 50 mol%), show similar spectra to that of the bulk glasses, although the main band is shifted towards higher wavenumbers in films when compared to bulk samples. The main contribution to that band is the vibration of Ge-O bonds in $[GeO_4]$ tetrahedra, while the band shift is due to contributions of Nb_2O_5, namely the band assigned to vibrations of Nb-O bonds in highly distorted $[NbO_6]$ octahedra, at 850 – 950 cm^{-1} in the case of bulk glasses.

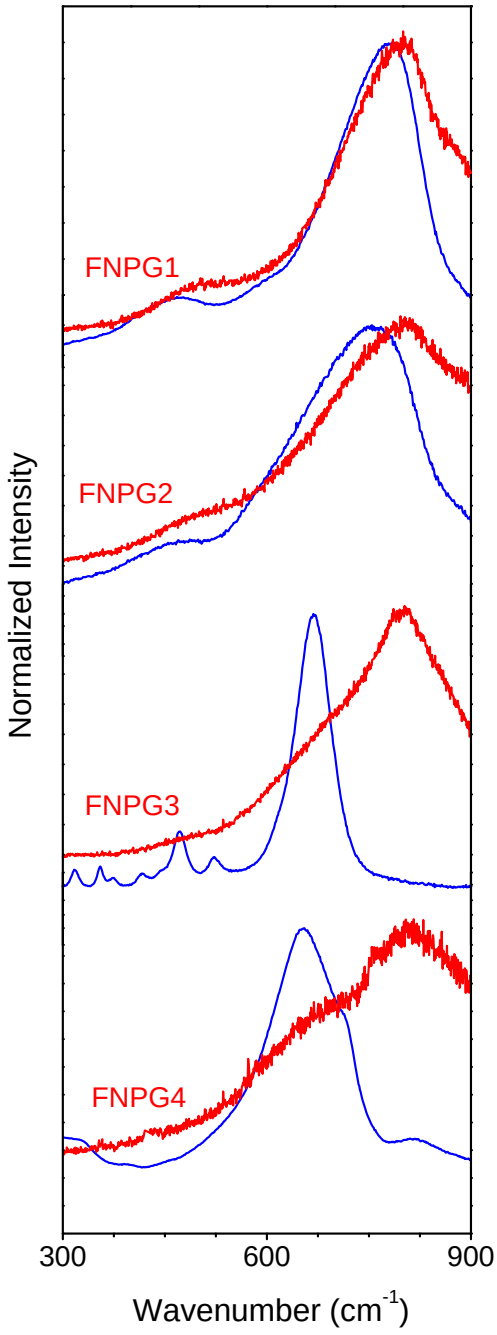

Figure 5.12: Raman spectra of NPG-series (blue line) film and (red line) bulk glasses.

The important role that Nb_2O_5 plays in the film glass network is confirmed by the spectra of films FNPG3 and FNPG4. These samples have a very low GeO_2 molar content and thus, the main band can be only assigned to vibrations of Nb_2O_5 units. The band shows shoulders at low and high frequency assigned to, respectively, slightly and highly distorted [NbO_6] octahedra. However, the exact origin of the band is not clear since none of the assigned bands in the spectra of bulk samples correspond to a frequency of 800 cm^{-1}. This band has been previously observed in glasses containing large Nb_2O_5 molar contents, and it has been assigned to two different structural units. On the one hand, Flambard *et al.* [163] have assigned it to Nb-O vibrations in chains of [NbO_6] octahedra, which are only formed for large Nb_2O_5 molar contents. On the other hand, Kolobkova [158] has pointed at the vibration of Nb-O bonds in [NbO_4] tetrahedral structural units Nb as the origin for a band at 800 cm^{-1}. However, niobium oxide compounds containing [NbO_4] tetrahedra are extremely rare.[156]. This band should be also present in the FNPG1 and FNPG2 film glasses, broadening the band related to [GeO_4] tetrahedra.

In conclusion, the glass network of films is characterized by the formation of a three-dimensional network based on [GeO_4] tetrahedra and either [NbO_4] tetrahedra or chains of [NbO_6] octahedra. Therefore, Nb_2O_5 and NbO_2, which has also an octahedral coordination, act as network formers. The formation of Nb-O-Ge and Nb-O-Nb linkages allows the deposition of vitreous films, even in those cases in which the bulk sample is crystalline.

5.2.4 Compositional and structural origin of the nonlinear optical response

The structural analysis of NPG-series film and bulk samples has shown the existence of strong differences between them. These differences must be responsible for the linear and nonlinear optical properties of film glasses, namely the high transparency in a wide range of compositions, the high linear refractive indexes, and the large third order optical susceptibility.

The transparency of the films with the Nb_2O_5 molar content is directly related to the ability of PLD to produce of phases out of the thermodynamical equilibrium as demonstrated by the synthesis of film glasses from either opal or crystalline bulk targets. The formation of a glass network in all films avoids the crystallization and makes films transparent.

Regarding the large linear and nonlinear optical response of films, the evolution of $\chi^{(3)}$ with the Nb atomic content indicates that the high polarizability and hyperpolarizability of Nb atom is responsible for the enhanced optical properties. In the case of bulk glasses containing Nb_2O_5, bridging Nb-O-Nb linkages have been associated with the enhancement of the hyperpolarizability.[164] For example, this contribution leads to values of the order of 10^{-13} esu as it is seen in borophosphate glasses with Nb_2O_5 molar content around 40 mol%,[165] and it can explain the slightly larger $\chi^{(3)}$ value of the transparent NPG2 bulk glass when compared to NPG1 glass. In the case of the films, this contribution is not enough to explain the large $\chi^{(3)}$ values obtained (10^{-12} – 10^{-11} esu).

In the case of TeO_2-based film glasses, the large fraction of NBO was proposed to be responsible for increasing $\chi^{(3)}$ up to values of the order of 10^{-12} esu. Raman spectra of NPG-series films have also a high concentration of highly distorted [NbO_6] octahedra containing NBO, but in this case the large fraction of NBO explains neither the evolution of $\chi^{(3)}$ with the Nb atomic content nor the differences between FNGP1 ($\chi^{(3)} \sim 10^{-12}$) and FNPG4 ($\chi^{(3)} \sim 10^{-11}$).

NPG-series films have a strong compositional difference with respect to bulk samples, since around half of the Nb atoms are in a reduced oxidation state, Nb^{4+}, forming NbO_2. Nb-O bond length in NbO_2 (1.7 Å) is smaller than in the case of Nb_2O_5 (2.0 Å).[166] Short bond lengths are found to increase the nonlinear response, since they favor the contribution of empty d orbitals to $\chi^{(3)}$ in TM oxides.[101] Additionally, Nb^{4+} has a lone electron in the $4d$ orbital, which is highly polarizable and thus, lead to larger nonlinear optical susceptibilities.[167] The amount of reduced Nb^{4+} obviously increases as the Nb atomic content increases, and thus, the higher the Nb atomic content the larger the value of $\chi^{(3)}$, as it is experimentally observed.

5.3 Summary and conclusions

In this chapter we have studied the nonlinear optical response of film glasses belonging to different glass systems containing a high amount of TM and HM oxides, through the measurement of the third order optical susceptibility by degenerate four wave mixing. Depending on the composition, the obtained $\chi^{(3)}$ values of film glasses are one or two orders of magnitude larger than those of bulk glasses. However, the exact origin of the enhancement of the nonlinear response depends on the glass system.

In the case of TeO_2-based glasses, we have first determined the wavelength range in which $\chi^{(3)}$ is only due to nonresonant processes by measuring $\chi^{(3)}$ at four different wavelengths. At wavelengths shorter than 800 nm, multiphoton absorption processes are responsible for the high measured $\chi^{(3)}$ values, while at wavelengths larger than 1000 nm, $\chi^{(3)}$ has an exclusive nonresonant origin.

The nonresonant $\chi^{(3)}$ values of film glasses are of the order of 10^{-12} esu in all cases, while $\chi^{(3)}$ of bulk glasses ranges from 3×10^{-13} esu up to 1.3×10^{-12} esu. The large $\chi^{(3)}$ values of films are proposed to be related to the contribution of the large NBO fraction in the films compared to that of bulk glasses, since NBO are know to have large polarizabilities and hyperpolarizabilities. This structural contribution, $\chi^{(3)}_{str}$, has been estimated to be of the order of 10^{-12} esu.

In the case of Nb_2O_5–PbO–GeO_2 glasses, the differences between the nonlinear properties of bulk and film glasses are even greater, since $\chi^{(3)}$ of bulk samples are of the order of 10^{-13} esu, while the $\chi^{(3)}$ of film glasses increases as the Nb atomic content increases, up to values of the order of 10^{-11} esu. These differences are related to the strong structural and compositional differences of films when compared to bulk samples. In the case of films, Nb^{5+} and Nb^{4+} act as network formers, forming Nb-O-Nb and Nb-O-Ge linkages. This allows the formation of a glass network even at compositions well outside the bulk glass forming region and thus, allowing the synthesis of transparent vitreous films. However, structural factors are not the main cause of the large $\chi^{(3)}$ values, in spite of the formation of highly hyperpolarizable Nb-O-Nb linkages or the large fraction of NBO. The main contribution to $\chi^{(3)}$ is the presence of a high fraction of Nb^{4+} cations in the films. Nb^{4+} is characterized by the presence of a highly polarizable lone electron in the *d* orbital, and it also forms a short Nb-O bond, which further increases the contribution of the *d* orbital to the nonlinear response.

Chapter 6

Conclusions

The synthesis by Pulsed Laser Deposition (PLD) of TeO_2-based film glasses for optical applications has been studied in the present thesis. First, the optimum experimental conditions for the film deposition have been determined. Second, the characterization of the optical properties of the films proves that the optimum films are transparent and show refractive indexes higher than 2 and enhanced third order optical susceptibilities ($\chi^{(3)} \sim 10^{-12}$). Finally, the analysis of the structure of the bulk and film glass networks has allowed us to understand the relation between the composition and structure of tellurite glasses and their optical response. In the next paragraphs, the main conclusions regarding the structure (i, ii) and optical response (iii, iv, v, vi) of TeO_2-based glasses and the structure and nonlinear response of Nb_2O_5–PbO–GeO_2 glasses (vii) are presented in detail.

Structure of tellurite glasses

i. The structure of the glass network of TeO_2–TiO_2–Nb_2O_5, TeO_2–WO_3–R_xO_y (R = Ti^{4+}, Ta^{5+}, Nb^{5+}, Pb^{2+}, Bi^{3+}, and La^{3+}), and TeO_2–WO_3–PbO glasses has been characterized by Raman spectroscopy. The different vibrational modes that comprise the Raman spectra have been assigned to the structural units of the different oxides. The most relevant units are those related to the main network former, the TeO_2. They can be classified into two groups: first, units that contribute to the formation of the glass network such as [TeO_4] trigonal bipyramids and second, units containing nonbridging oxygens (NBO) such as [$TeO_{3+\delta}$] polyhedra and [TeO_3] trigonal

pyramids.

The other oxides have been classified according to their role in the glass network: those oxides containing cations R that ease the formation of bridging Te-O-R linkages are considered network formers (WO_3, TiO_2, Ta_2O_5, and Nb_2O_5), while the oxides that lead to an increase of the fraction of NBO are considered network modifiers (PbO, Bi_2O_3, and La_2O_3).

It has been demonstrated that the presence of cations acting as network formers, such as W^{6+}, leads to the formation of strong bonds and stable networks.

ii. The synthesis of film glasses by PLD has been demonstrated and the effect on the composition and structure of two important experimental deposition parameters, such as the laser energy density (E) and the oxygen gas pressure (P_{O_2}), has been analyzed. Films deposited at low E and P_{O_2} show strong compositional and structural differences when compared to the original bulk glass, namely the presence of Te atoms in a reduced oxidation state (Te^0) and a large fraction of NBO.

Optimum films without reduced cations can be only deposited in a narrow range of energies and pressures centered at E = 1.5 J cm^{-2} and $P_{O_2} \simeq 8$ Pa. These films posess glass networks similar to those of bulk glasses but with a larger fraction of NBO. They also show a slight enhancement of the molar content of the oxides containing heavy cations.

The evolution of the composition and structure with the experimental conditions has been discussed in terms of the properties of the laser induced plasma and the plasma dynamics in an oxidizing environment. Several different mechanisms have been identified for the oxidation of Te atoms. The increase of the laser energy density favors the oxidation of Te atoms by increasing the kinetic energy of Te atoms and the dissociation of O_2 by collisional and photoinduced processes. However, the main mechanism is the dissociation of O_2 at high oxygen pressures due to the formation of a high density shock layer during the plasma expansion.

Optical properties of tellurite glasses

iii. The linear optical properties of film and bulk glasses have been characterized through spectroscopic ellipsometry and transmission measurements.

The complex linear refractive index and the optical cutoff of the UV absorption edge, are mainly determined by the glass composition. However, in the case of film glasses additional structural factors play a significant role.

The optical response of films deposited out of the optimum conditions is determined by the presence of Te^0 atoms, the large fraction of NBO, and the lower density of the films when compared to bulk glasses. On the contrary, films deposited using the optimum conditions are transparent and have linear refractive indexes lower than that of bulk glasses due to their reduced density, but still higher than 2.

iv. In order to understand the effect of the compositional and structural factors on the optical response of films, we have developed an effective medium model whose optical properties are based on the Maxwell Garnett model. The model allows predicting the film density and the fraction of Te^0 atoms. The results obtained are in good agreement with those deduced from the compositional analysis, thus confirming the fundamental role that the composition and the structure of films play on their optical response.

v. The nonlinear optical response of optimum films has been characterized through their third order optical susceptibility ($\chi^{(3)}$), measured using the degenerate four wave mixing technique. We have developed a new procedure to deconvolute the conjugated signal of the film (thickness ~ 3 μm) from the substrate (~ 100 μm) based on the definition of an effective substrate thickness and the choice of the appropriate experimental configuration. This procedure allows us to measure $\chi^{(3)}$ values of films of only 10 times larger than that of SiO_2-based glasses ($\sim 10^{-14}$ esu).

vi. The wavelength range in which $\chi^{(3)}$ is only due to nonresonant processes has been determined in the case of TeO_2-based glasses. At wavelengths longer than 1000 nm, $\chi^{(3)}$ has an exclusive nonresonant origin, while at wavelengths shorter than 800 nm, multiphoton absorption processes are responsible for the observed increase of $\chi^{(3)}$. The nonresonant $\chi^{(3)}$ values of bulk glasses are of the order of 10^{-13} esu for the TeO_2–TiO_2–Nb_2O_5 system, and 10^{-12} esu for the TeO_2–WO_3–R_xO_y and TeO_2–WO_3–PbO systems. However, film glasses show nonresonant $\chi^{(3)}$ values of the order of 10^{-12} esu in all cases.

The nonlinear optical response of tellurite bulk glasses is mainly determined

by the large hyperpolarizability of Te^{4+}, transition and heavy metal cations. In the case of TeO_2–TiO_2–Nb_2O_5 thin film glasses, since their composition is very similar to that of bulk glasses, the observed enhancement of $\chi^{(3)}$ is related to the large fraction of NBO, which are characterized by a large polarizability and hyperpolarizability, observed in the film. This structural contribution is estimated to be of the order of 10^{-12} esu.

Nb_2O_5–PbO–GeO_2 glasses

Finally, the knowledge gained from the structural characterization of TeO_2-based glasses by Raman spectroscopy, and the relation between the optical response and the composition and structure, has been the basis for the interpretation of previous experimental results in film glasses belonging to the Nb_2O_5–PbO–GeO_2 system. The main conclusion obtained from this study is:

vii. The $\chi^{(3)}$ values of bulk samples are of the order of 10^{-13} esu, while the $\chi^{(3)}$ of film glasses increases as the Nb atomic content increases, up to values of the order of 10^{-11} esu. In this case, film glasses have network structures very different from those of bulk samples, based on structural units of niobium oxides. Such a glass network cannot be achieved by the traditional melting methods, and allows the formation of transparent film glasses with compositions out of the bulk glass forming region. Additionally, a significant fraction of the Nb atoms are in a reduced oxidation state, Nb^{4+}, forming NbO_2. The presence of that oxide increases the nonlinear response of films up to values of the order of 10^{-12} – 10^{-11} esu due to the lone electron in the d band of Nb^{4+} and the short length of Nb-O bonds.

Spanish summary

Objetivo de la tesis

El principal objetivo de esta tesis es la síntesis, mediante la técnica de Depósito por Láser Pulsado (PLD), de vidrios de teluritos en lámina delgada con propiedades ópticas optimizadas para su posible aplicación en dispositivos fotónicos. La consecución del objetivo anteriormente expuesto requiere optimizar el proceso de depósito, estudiar la estructura de la red vítrea y caracterizar las propiedades ópticas lineales y no lineales tanto de vidrios de teluritos masivos como en lámina delgada. Dado que la respuesta óptica en los vidrios está fuertemente relacionada con su composición y estructura, es asimismo necesario entender la influencia de estos dos parámetros en dicha respuesta, para poder así determinar las condiciones en las que se obtienen láminas delgadas con las mejores propiedades ópticas no lineales.

Metodología y estructura de la tesis

El Grupo de Procesado por Láser (LPG) del Instituto de Óptica (IO - CSIC) tiene una dilatada experiencia en los aspectos tanto fundamentales como aplicados del PLD y, en particular, en su uso para el depósito de materiales ópticos. De hecho, el grupo ha aplicado con éxito esta técnica en la producción de láminas delgadas de diferentes sistemas vítreos. Este conocimiento previo sirve como punto de partida para la presente tesis

El primer paso de este trabajo ha sido la síntesis de vidrios de teluritos masivos y su caracterización mediante espectroscopía Raman para determinar las unidades estructurales fundamentales y el papel que juegan los diferentes óxidos en la estructura del vidrio. Este estudio constituye la base para la descripción de las propiedades estructurales de láminas de vidrios de teluritos depositadas me-

diante PLD y su relación con la respuesta óptica lineal y no lineal. Se han seleccionado tres diferentes sistemas vítreos diferentes, que incluyen en su composición óxidos de metales de transición (TM) y de metales pesados (HM): TeO_2–TiO_2–Nb_2O_5, TeO_2–WO_3–R_xO_y (donde R_xO_y = TiO_2, Nb_2O_5, Ta_2O_5, WO_3, La_2O_3, Bi_2O_3 o PbO), y TeO_2–WO_3–PbO.

Los parámetros experimentales del PLD determinan la composición y las propiedades ópticas de las láminas depositadas. Por tanto, se ha desarrollado inicialmente un estudio sistemático de la relación entre los parámetros de depósito y la composición, estructura y propiedades ópticas de vidrios de teluritos en lámina delgada. Los resultados obtenidos se han analizado en términos de la dinámica de expansión del plasma y de los procesos de depósito de material en lámina delgada mediante PLD, permitiendo así determinar las condiciones óptimas de depósito.

A continuación se han depositado láminas en una amplia gama de composiciones utilizando las condiciones óptimas determinadas anteriormente. Se han estudiado las propiedades ópticas lineales y no lineales de las láminas y se han comparado con las de los vidrios masivos. Las diferencias observadas en la respuesta óptica se han discutido en términos de la composición y las modificaciones estructurales inducidas en las láminas durante el proceso de depósito.

Por último, el conocimiento adquirido en la caracterización estructural y el análisis composicional de los vidrios de teluritos ha servido para entender y explicar la respuesta óptica lineal y no lineal de vidrios en lámina delgada pertenecientes al sistema Nb_2O_5–PbO–GeO_2.

El trabajo desarrollado en la presente tesis se ha estructurado en seis capítulos. A continuación se resumen los principales resultados presentados en cada uno de ellos.

Capítulo 1: Introducción

El capítulo 1 es una introducción general a la temática de la tesis, en la que se explican las motivaciones, objetivos y metodología del trabajo realizado.

Capítulo 2: Técnicas experimentales

Este capítulo está dedicado a la descripción de las técnicas experimentales utilizadas en la síntesis y caracterización de vidrios de teluritos, tanto en configuración masiva, preparados mediante el mezclado y fundido de óxidos en polvo,

como en lámina delgada, obtenidos mediante la técnica de depósito por láser pulsado.

Para la caracterización composicional se han empleado dferentes técnicas de análisis mediante haces de iones (RBS, NRA y PIXE), así como la espectroscopía XPS. Esta última ha permitido, además, estudiar el estado químico de los átomos presentes. Por otro lado, las unidades estructurales que conforman la red vítrea de las muestras han sido determinadas mediante espectroscopía Raman. Finalmente, se han analizado las propiedades ópticas de vidrios masivos y en lámina delgada. En particular, la respuesta óptica lineal de las muestras se ha caracterizado a través de su transmisión y de su índice de refracción complejo, medido mediante elipsometría espectroscópica, mientras que la respuesta óptica no lineal lo ha sido mediante la determinación de la susceptibilidad óptica de tercer orden ($\chi^{(3)}$), usando la técnica de Mezclado Degenerado de Cuatro Ondas (DFWM).

Capítulo 3: Vidrios masivos de teluritos

Este capítulo se centra en la caracterización de la estructura y la respuesta óptica lineal de vidrios masivos. En primer lugar, se decribe el estado vítreo de manera general, centrándose a continuación en la estructura y respuesta óptica de vidrios de óxidos.

En el caso de los vidrios de teluritos, su estructura ha sido explicada previamente en términos de las unidades estructurales del TeO_2 cristalino. A partir de estos resultados, se ha analizado la red vítrea de los vidrios de teluritos considerados en el presente trabajo mediante espectroscopía Raman. Las unidades estructurales básicas de los vidrios de teluritos se describen con ayuda del espectro Raman de un vidrio TeO_2–TiO_2–Nb_2O_5 con un alto contenido en TeO_2 (90 mol%). Este análisis sirve como base para el estudio de la estructura de vidrios más complejos pertenecientes a los sistemas TeO_2–WO_3–R_xO_y y TeO_2–WO_3–PbO.

La red vítrea está formada por unidades estructurales caracterizadas por diferentes índices de coordinación del átomo de Te, como son las bipirámides trigonales (tbp) [TeO_4], los poliedros [$TeO_{3+\delta}$] y las pirámides trigonales (tp) [TeO_3]. En el caso de los vidrios pertenecientes al sistema TeO_2–WO_3–R_xO_y, se ha demostrado como la adición de diferentes óxidos TM (TiO_2, Nb_2O_5, Ta_2O_5, WO_3 y Nb_2O_5) o HM (Bi_2O_3 y PbO) rompe los enlaces Te-O-Te que conforman la red y da lugar a dos comportamientos diferentes según el óxido añadido. En el caso

de que el óxido contenga un catión R con una intesidad de campo mayor que la del Te^{4+} se forman enlaces Te-O-R y el óxido actúa como formador de red. Por otro lado, si la intensidad de campo de R es menor que la del Te^{4+}, las unidades $[TeO_4]$ se transmforman en unidades $[TeO_3]$, caracterizadas por contener oxígenos no puente (NBO) que no están enlazando dos cationes y, por tanto, rompen la continuidad de la red vítrea. El óxido actúa en este caso como modificador de red.

Estas modificaciones son más evidentes en el caso de los vidrios pertenecientes al sistema TeO_2–WO_3–PbO, los cuales se prepararon con contenidos molares de TeO_2, WO_3 y PbO muy diferentes. El WO_3 y el PbO tienen papeles opuestos en la red vítrea. En el caso del WO_3, el catión W^{6+} tiene una gran intensidad de campo y por tanto actúa como formador de red. En aquellos vidrios con un contenido molar de WO_3 elevado, los enlaces Te-O-Te se rompen para formar enlaces Te-O-W. Por el contrario, el Pb^{2+} tiene una intensidad de campo pequeña y, por tanto, el PbO actúa como modificador de red. Aquellos vidrios con un gran contenido molar de PbO se caracterizan por elevadas fracciones de NBO, según muestran los espectros Raman.

Los resultados anteriores han sido confirmados por el análisis de la estabilidad térmica de los vidrios TeO_2–WO_3–PbO. La temperatura de transición vítrea depende linearmente del contenido molar de los diferentes óxidos, aumentando con el contenido molar del WO_3 debido a la formacíón de enlaces W-O fuertes. Además, la estabilidad térmica, definida como la diferencia entre la temperatura de cristalización y la temperatura de transición vítrea, es mayor para aquellos vidrios con un contenido molar de WO_3 en el intervalo 10 – 30 mol%. Por tanto, desde el punto de vista de la estabilidad térmica, los vidrios de telurito a los que se les añade WO_3 son prometedores para la fabricación de dispositivos, gracias a la gran estabilidad de su red vítrea.

Los cambios composicionales y estructurales anteriormente descritos tienen un efecto fundamental en las propiedades ópticas de los vidrios. Las composiciones preparadas tienen índices de refracción elevados ($n > 2$ a 1500 nm) y no presentan absorciones intrínsecas en su región de transparencia. La posición del borde de absorción en el UV depende de la composición del vidrio tanto en la serie de vidrios TeO_2–WO_3–R_xO_y como en la TeO_2–WO_3–PbO. En particular, los vidrios binarios TeO_2–WO_3 y los ternarios con un elevado contenido molar de WO_3 tienen su borde de absorpción desplazado hacia el rojo con respecto a las demás composiciones. Este comportamiento se ha relacionado con la elevada

conductividad eléctrica registrada en la literatura para vidrios de TeO_2 y WO_3. La adición de otros óxidos reduce dicha conductividad y, por tanto, el borde de absorpción se desplaza hacia longitudes de onda menores. Adicionalmente, el coeficiente de absorción se ha analizado en el borde de absorción en el UV mediante la relación de Urbach. La energía de Urbach, qué está relacionada con la densidad de estados localizados en el "gap" de energía, es similar en todos los casos ($E_U = 0.10 - 0.11$ eV), excepto en el vidrio binario $80TeO_2 \cdot 20PbO$ ($E_U =$ 0.155 eV), que es el vidrio con una red vítrea más desordenada de acuerdo con el analisis estructural. Finalmente, todos los vidrios poseen índices de refracción similares ($n = 2.09$ – 2.15 a 1500 nm). Los mayores valores los presentan aquellos vidrios que contienen cationes de metales pesados, como Bi^{3+} o Pb^{2+}, debido a su elevada polarizabilidad.

Capítulo 4: Vidrios de teluritos en lámina delgada

Este capítulo está dedicado a determinar las condiciones óptimas para la obtención de vidrios de teluritos en lámina delgada mediante la técnica de depósito por láser pulsado. Dado que la composición, estructura y propiedades ópticas de las láminas producidas están fuertemente determinadas por las condiciones de depósito, se ha estudiado el efecto de dos parametros experimentales fundamentales: la densidad de energía del láser (E) sobre el vidrio usado como blanco y la presión de oxígeno (P_{O_2}) en el interior de la cámara de depósito.

Para realizar este estudio se han depositado láminas a diferentes energías y presiones de oxígeno a partir de un vidrio masivo transparente con composición $90TeO_2 \cdot 5TiO_2 \cdot 5Nb_2O_5$. Aquellas láminas depositas usando valores de E o P_{O_2} pequeños presentan fuertes diferencias composicionales y estructutrales cuando se comparan con el vidrio masivo, como son la presencia de átomos de Te en un estado de oxidación reducido (Te^0) y una fracción muy elevada de NBO. Estas diferencias disminuyen según aumenta E o P_{O_2}. Estos resultados y su efecto sobre la respuesta óptica son analizados en términos de la dinámica de expansión del plasma, dado que la energía cinética y la distribución espacial de los diferentes átomos están fuertemenete relacionados con las propiedades de las láminas resultantes.

En el caso de la densidad de energía, al incrementar E aumenta la energía cinética de las especies en el plasma generado por el pulso láser. La energía cinética no solo tiene un efecto fundamental en la dinámica del plasma sino que

también permite la existencia de reacciones químicas entre las distintas especies y los átomos o moléculas del gas presente en la cámara. Este hecho es especialmente importante en el caso del Te, ya que la oxidación del Te en una atmósfera de O_2 sólo es probable que ocurra a elevadas energías, al ser dicha reacción endotérmica.

La densidad de energía no es, sin embargo, el único parámetro relacionado con la presencia de Te reducido, dado que incluso las láminas depositadas a las mayores E presentan átomos de Te^0. Para eliminar completamente el Te reducido de las láminas es necesario aumentar la presión de O_2. Aunque un aumento de P_{O_2} en la cámara debe implicar una menor energía cinética, lo que es desfavorable para la oxidación del Te, una mayor presión implica también la formación de una región del gas en la frontera con el plasma en la cual la densidad de moléculas de O_2 es más elevada. En esta región, la disociación de las moléculas de O_2 es mucho más probable y por tanto la reacción de oxidación del Te se ve favorecida. Tan sólo aquellas láminas depositadas a elevadas E y P_{O_2} no presentan átomos de Te reducido. Además, estas láminas presentan también redes vítreas similares a la del vidrio masivo pero con fracciones de NBO mayores.

La respuesta óptica de las láminas está determinada por su composición y estructura. Las láminas tienen una densidad menor que la del vidrio masivo, lo que implica índices de refracción menores. Sin embargo, la presencia de átomos de Te^0 y una mayor fracción de NBO, caracterizados por una polarizabilidad elevada, aumentan el índice de refracción. El efecto de estos tres factores (densidad reducida, átomos de Te^0 y NBO) en las propiedades ópticas se ha analizado utilizando un modelo de Maxwell Garnett de medio efectivo. Las propiedades ópticas deducidas a partir del modelo son coincidentes con las medidas experimentales en aquellas láminas con un contenido pequeño de Te^0, mientras que para contenidos mayores, las predicciones del modelo son peores.

Este estudio nos ha permitido definir un intervalo reducido de E y P_{O_2} en el que se pueden obtener láminas con estructura y propiedades ópticas óptimas. Dicho intervalo está centrado en $E = 1.5$ J cm^{-2} and $P_{O_2} \simeq 8$ Pa. Se han depositado usando estas condiciones vidrios en lámina delgada a partir de diferentes composiciones seleccionadas pertenecientes a los sistemas TeO_2–TiO_2–Nb_2O_5, TeO_2–WO_3–R_xO_y y TeO_2–WO_3–PbO. La composición de estas láminas óptimas está caracterizada por la ausencia de cationes reducidos y por un ligero enriquecimiento de la concentración de los átomos más pesados. Estas diferencias composicionales respecto al vidrio masivo están relacionadas con la dinámica de los cationes más pesados en el plasma. La estructura de las láminas óptimas es

también similar a la de los vidrios masivos y sólo difiere en la mayor fracción de NBO.

En cuanto a las propiedades ópticas, las láminas óptimas son transparentes en un amplio intervalo de longitudes de onda y tienen índices de refracción menores que los vidrios masivos, debido a una menor densidad. El "gap" óptico de las láminas tiene un comportamiento similar al de los vidrios masivos. Sin embargo, en el caso de las láminas, el "gap" no sólo está relacionado con la composición del vidrio sino también con la elevada fracción de NBO, cuya concentración es diferente entre diferentes muestras.

Capítulo 5: Propiedades ópticas no lineales de vidrios multicomponentes

En este capítulo se estudia la respuesta óptica no lineal de vidrios masivos y en lámina delgada pertenecientes a diferentes sistemas vítreos y que contienen en todos los caso un alto porcentaje de óxidos de TM o de HM. Para ello se ha medido el módulo de la componente diagonal del tensor de susceptibilidad óptica de tercer orden ($\chi^{(3)}$) de las muestras mediante la técnica DFWM.

En el caso de vidrios de teluritos, se ha determinado en primer lugar el intervalo de longitudes de onda en el cual $\chi^{(3)}$ es exclusivamente debido a procesos no resonantes, para lo cual se ha medido $\chi^{(3)}$ a diferentes longitudes de onda. Para longitudes de onda inferiores a 800 nm, los procesos de absorción multifotónica son responsables de los altos valores de $\chi^{(3)}$ obtenidos, mientras que a longitudes de onda mayores de 1000 nm, $\chi^{(3)}$ tiene un origen exclusivamente no resonante.

Los valores no resonantes de $\chi^{(3)}$ de los vidrios de teluritos en lámina delgada son del orden de 10^{-12} esu en todos los casos, mientras que en el caso de los vidrios masivos, $\chi^{(3)}$ tiene valores desde 3×10^{-13} esu hasta 1.3×10^{-12} esu dependiendo de la composición. Los valores elevados de $\chi^{(3)}$ en las láminas se han relacionado con una contribución de tipo estructural, asociada a la gran fracción de NBO característica de las láminas y que da lugar a valores de $\chi^{(3)}$ del orden de 10^{-12} esu.

En la segunda parte del capítulo se ha aplicado el conocimiento adquirido en los vidrios de teluritos a un sistema vítreo diferente: Nb_2O_5–PbO–GeO_2. En estos vidrios, las diferencias entre la respuesta no lineal de vidrios masivos y vidrios en lámina delgada son mayores, dado que los vidrios masivos presentan valores de $\chi^{(3)}$ del orden de 10^{-13} esu, mientras que en caso de las láminas delgadas $\chi^{(3)}$

aumenta con el contenido atómico de Nb, hasta valores del orden de 10^{-11} esu. Estas diferencias están relacionadas con las marcadas diferencias composicionales y estructurales entre muestras masivas y vidrios en lámina delgada. En el caso de las láminas, estas presentan un elevado porcentaje de átomos de Nb en un estado de oxidación reducido (Nb^{4+}). Tanto el Nb^{5+} como el Nb^{4+} actúan como formadores de red, formando enlaces Nb-O-Nb y Nb-O-Ge. Esto favorece la formación de una red vítrea, incluso para composiciones que en el caso masivo están bastante alejadas del area composicional de formación de vidrio. Sin embargo, los factores estructurales no son los principales responsables de los elevados valores de $\chi^{(3)}$, a pesar de la formación de enlaces Nb-O-Nb muy polarizables o de la elevada fracción de NBO típica de las láminas delgadas. La principal contribución a $\chi^{(3)}$ es la presencia de cationes Nb^{4+} en las láminas, dado que el Nb^{4+} posee un único electrón en el orbital d que es muy polarizable, y además forma enlaces Nb-O más cortos que el Nb^{5+}, lo que incrementa aún más la contribución del orbital d a la respuesta no lineal.

Capítulo 6: Conclusiones

En este capítulo se resumen las principales conclusiones obtenidas en la tesis, las cuales son desarrolladas ampliamente en la siguiente sección.

Conclusiones

En la presente tesis se ha estudiado la síntesis de vidrios de teluritos en lámina delgada mediante depósito por láser pulsado para aplicaciones ópticas. Para ello se han determinado en primer lugar las condiciones óptimas de depósito. A continuación se han caracterizado las propiedades ópticas de las láminas, demostrando que es posible depositar láminas transparentes con índices de refracción mayores que 2 y elevadas susceptibilades ópticas de tercer orden ($\chi^{(3)} \sim 10^{-12}$), mayores incluso que las de los correspondientes vidrios masivos. Finalmente, el análisis de la estructura de los vidrios masivos y en lámina delgada ha permitido entender la relación entre composición, estructura y respuesta óptica. A continuación se resumen las principales conclusiones alcanzadas acerca de la estructura (i, ii) y respuesta óptica (iii, iv, v, vi) de vidrios de teluritos y de vidrios pertenecientes al sistema Nb_2O_5–PbO–GeO_2 (vii).

Estructura de vidrios de teluritos

i. La estructura de la red vítrea de vidrios pertenecientes a los sistemas TeO_2–TiO_2–Nb_2O_5, TeO_2–WO_3–R_xO_y (R = Ti^{4+}, Ta^{5+}, Nb^{5+}, Pb^{2+}, Bi^{3+}, y La^{3+}), y TeO_2–WO_3–PbO se ha caracterizado mediante espectroscopía Raman. Los diferentes modos vibracionales que forman el espectro Raman se han asignado a las unidades estructurales de los diferentes óxidos que forman el vidrio. Las unidades más importantes son aquéllas relacionadas con el principal formador de red, el TeO_2, que pueden clasificarse en 2 grupos: en primer lugar, unidades que contribuyen a la formación de la red vítrea como las bipirámides trigonales [TeO_4] y en segundo lugar, unidades que continen oxígenos no puente (NBO) como los poliedros [$TeO_{3+\delta}$] y las pirámides trigonales [TeO_3].

   El resto de óxidos han sido clasificados de acuerdo a su papel en la red vítrea: Aquellos óxidos que contienen cationes R que forman enlaces Te-O-R son considerados formadores de red (WO_3, TiO_2, Ta_2O_5 y Nb_2O_5), mientras que los óxidos que incrementan la fracción de NBO se consideran modificadores de red (PbO, Bi_2O_3 y La_2O_3). Se ha demostrado como la presencia de cationes actuando como formadores de red, como el W^{6+}, conlleva la formación de enlaces fuertes y redes más estables.

ii. Se ha demostrado la síntesis de vidrios en lámina delgada mediante PLD y se ha analizado el efecto que tienen en la composición y en la estructura dos parámetros experimentales fundamentales, como son la densidad de energía del láser (E) y la presión de oxígeno (P_{O_2}). Aquellas láminas depositadas a bajas E y P_{O_2} muestran marcadas diferencias composicionales y estructurales con respecto al vidrio masivo, como son la presencia de Te reducido (Te^0) y una elevada fracción de NBO. Es posible la obtención de láminas óptimas en un pequeño intervalo de condiciones experimentales, centrado en $E = 1.5$ J cm^{-2} y $P_{O_2} \simeq 8$ Pa. Las láminas óptimas tienen composiciones y redes vítreas similares a la del vidrio masivo pero con un ligero incremento del contenido en cationes pesados y una fracción de NBO mayor.

   La evolución de la composición y de la estructura con las condiciones experimentales se ha analizado en términos de las propiedades del plasma inducido por el pulso láser y su dinámica en un ambiente oxidante. Se han identificado varios mecanismos como responsables de la oxidación de los átomos de Te. El aumento de la densidad de energía favorece la oxidación

del Te al aumentar la enercía cinética de los átomos de Te en el plasma y la probabilidad de disociación de las moléculas de oxígeno en el gas. Sin embargo el mecanismo dominante es la disociación del O_2 a presiones elevadas debido a la formación en la frontera entre el gas y el plasma en expansión de una región con un gran densidad de moléculas de O_2.

Propiedades ópticas de vidrios de teluritos

iii. Se han caracterizado las propiedades ópticas lineales de los vidrios masivos y en lámina delgada mediante elipsometría espectroscópica y medidas de transmisión. El índice de refracción complejo y la posición del borde de absorción en el UV están determinados fundamentalmente por la composición del vidrio. Sin embargo, en el caso de los vidrios en lámina delgada hay factores estructurales adicionales que afectan a la respuesta óptica.

    En el caso de láminas depositadas fuera de las condiciones óptimas, la respuesta óptica está determinada por la presencia de átomos de Te^0, la elevada fracción de NBO y una densidad menor que la del vidrio masivo. Por el contrario, las láminas depositadas usando condiciones óptimas son transparentes y tienen índices de refracción mayores que 2, aunque inferiores a los del vidrio masivo debido a la menor densidad de las láminas.

iv. Para entender el efecto que la composición y la estructura tienen en la respuesta óptica de las láminas, se ha desarrollado un modelo de medio efectivo basado en el modelo de Maxwell Garnet, y que permite estimar la densidad de las láminas y la fracción de atomos de Te^0. Los resultados obtenidos están en concordancia con aquéllos deducidos a partir de las medidas composicionales, confirmando el papel fundamental que la composición y la estructura tienen en la respuesta óptica.

v. La respuesta óptica no lineal de los vidrios, tanto masivos como en lámina delgada, se ha caracterizado mediante la medida de su susceptibilidad óptica de tercer orden ($\chi^{(3)}$) utilizando la técnica de mezclado degenerado de cuatro ondas. Se ha desarrollado un nuevo procedimiento de medida para optimizar la deconvolución de la señal conjugada de la lámina (de espesor ~ 3 μm) respecto a la señal del substrato sobre el que está depositada la lámina (de espesor ~ 100 μm), basado en la definición de un espesor efectivo del substrato y en la elección adecuada de la configuración del experimento.

Este procedimiento nos permite medir valores de $\chi^{(3)}$ en láminas delgadas tan sólo 10 veces mayores que los de los vidrios de silicatos ($\sim 10^{-14}$ esu).

vi. Se ha determinado el intervalo de longitudes de onda en las cuales $\chi^{(3)}$ tiene únicamente un origen no resonante en el caso de vidrios de teluritos. Para longitudes de onda mayores de 1000 nm, $\chi^{(3)}$ tiene un origen exclusivamente no resonante, mientras que para longitudes de onda más cortas a 800 nm, los procesos de absorción multifotónica son responsables del incremento de $\chi^{(3)}$. Los valores no resonantes de $\chi^{(3)}$ en el caso de vidrios masivos son del orden de 10^{-13} esu para el sistema TeO_2–TiO_2–Nb_2O_5 y del orden de 10^{-12} para los sistemas TeO_2–WO_3–R_xO_y y TeO_2–WO_3–PbO. Sin embargo, los vidrios en lámina delgada muestran valores no resonantes de $\chi^{(3)}$ del orden de 10^{-12} esu en todos los casos.

   La respuesta óptica no lineal en vidrios de teluritos está principalmente determinada por la gran hiperpolarizabilidad del Te^{4+}, de los cationes de metales de transición y de los cationes de metales pesados. En el caso de las láminas pertenecientes al sistema TeO_2–TiO_2–Nb_2O_5, dado que su composición es muy similar a la del vidrio masivo, el incremento observado se ha asociado a la elevada fracción de NBO, caracterizados por su gran polarizabilidad e hiperpolarizabilidad. Esta contribución estructural se ha estimado del orden de 10^{-12} esu.

Vidrios Nb_2O_5–PbO–GeO_2

Finalmente, el conocimiento adquirido en la caracterización estructural de los vidrios de teluritos y en la relación entre composicón, estructura y respuesta óptica ha permitido interpretar resultados experimentales previos en vidrios en lámina delgada pertenecientes al sistema Nb_2O_5–PbO–GeO_2. Las principales conlusiones obtenidas son:

vii. Los valores de $\chi^{(3)}$ en los vidrios masivos son del orden de 10^{-13} esu, mientras que en los vidrios en lámina delgada $\chi^{(3)}$ aumenta con el contenido atómico de Nb, hasta valores del orden de 10^{-11} esu. En el caso de las láminas, la estructura de la red vítrea, basada en unidades estructurales de óxidos de Nb, es muy diferente respecto a la de las muestras masivas. Una red vítrea así no es posible obtenerla con los métodos convencionales de preparación de vidrios masivos y, por tanto, el PLD permite la formación

de vidrios transparentes en lámina delgada con composiciones fuera del intervalo de formación de vidrios masivos. Además, las láminas presentan un alto porcentaje de átomos de Nb en un estado reducido (Nb^{4+}), formando NbO_2. La presencia de este óxido incrementa la respuesta no lineal de las láminas hasta valores del orden de 10^{-12} – 10^{-11} esu debido a la presencia de un único electrón en el orbital *d* del Nb^{4+} y a la menor distancia del enlace Nb-O en el NbO_2 con respecto al Nb_2O_5.

Bibliography

[1] Lifante, G. *Integrated photonics: fundamentals.* John Wiley, (2003).

[2] Clesca, B. *Photonics Science News* **1**(4), 11–26.

[3] Desurvire, E., Bayart, D., Desthieux, B., and Bigo, S. *Erbium doped fiber amplifiers: Device and System Developments.* John Wiley & Sons, New York, (2002).

[4] Thomas, G. A., Ackerman, D. A., Prucnal, P. R., and Cooper, S. L. *Physics Today* **53**(9), 30–36 (2000).

[5] Stix, G. *Investigación y Ciencia* **294**, 4–9 (2001).

[6] Daukantas, P. *Optics & Photonics News* **19**(6), 34–39 (2008).

[7] Cotter, D., Manning, R. J., Blow, K. J., Ellis, A. D., Kelly, A. E., Nesset, D., Phillips, I. D., Poustie, A. J., and Rogers, D. C. *Science* **286**(5444), 1523–1528 (1999).

[8] Guenot, P. *MRS Bulletin* **28**(5), 360–364 (2003).

[9] Hibino, Y. *MRS Bulletin* **28**(5), 365–371 (2003).

[10] Pleumeekers, J. L., Evans, P. W., Chen, W., Schneider, R. P., and Nagarajan, R. *Optics & Photonics News* **20**(3), 20–25 (2009).

[11] Yamane, M. and Asahara, Y. *Glasses For Photonics.* Cambridge University Press, Cambridge, (2000).

[12] Sutherland, R. L. *Handbook of Nonlinear Optics.* Dekker, New York, (1996).

[13] Borrelli, N. F. and Hall, D. W. In *Optical properties of glass,* Uhlmann, D. R. and Kreidl, N. J., editors. American Ceramic Society, Westerville (1991).

[14] Tanaka, K. *Journal of Materials Science: Materials in Electronics* **16**(10), 633–643 (2005).

[15] Jha, A., Liu, X., Kar, A. K., and Bookey, H. T. *Current Opinion in Solid State and Materials Science* **5**(6), 475–479 (2001).

[16] Vogel, E. M., Weber, M. J., and Krol, D. M. *Physics and Chemistry of Glasses* **32**(6), 231–254 (1991).

[17] Bloembergen, N. *Journal of Nonlinear Optical Physics & Materials* **5**(1), 1–7 (1996).

[18] Lines, M. E. *Journal of Applied Physics* **69**(10), 6876–6884 (1991).

[19] Marker, A. J. and Neuroth, N. In *The Properties of Optical Glass,* Bach, H. and Neuroth, N., editors. Springer-Verlag, Berlin (1995).

[20] El-Mallawany, R. A. H. *Tellurite Glasses Handbook. Physical Properties and Data.* CRC Press, Boca Raton, (2002).

[21] Dimitrov, V. and Komatsu, T. *Journal of Non-Crystalline Solids* **249**(2-3), 160–179 (1999).

[22] Jha, A., Shen, S., and Naftaly, M. *Physical Review B* **62**(10), 6215–6227 (2000).

[23] Shen, S. X., Jha, A., Liu, X. B., Naftaly, M., Bindra, K., Bookey, H. J., and Kar, A. K. *Journal of the American Ceramic Society* **85**(6), 1391–1395 (2002).

[24] Wang, J. S., Machewirth, D. P., Wu, F., Snitzer, E., and Vogel, E. M. *Optics Letters* **19**(18), 1448–1449 (1994).

[25] Mori, A., Ohishi, Y., and Sudo, S. *Electronics Letters* **33**(10), 863–864 (1997).

[26] Mori, A. *Journal of the Ceramic Society of Japan* **116**(1358), 1040–1051 (2008).

[27] Bookey, H. T., Lousteau, J., Jha, A., Gayraud, N., Thomson, R. R., Psaila, N. D., Li, H., MacPherson, W. N., Barton, J. S., and Kar, A. K. *Optics Express* **15**(26), 17554–17561 (2007).

[28] http://www.nel−world.com/products/photonics/opt_m_tellurite.html.

[29] Ohta, T., Takenaga, M., Akahira, N., and Yamashita, T. *Journal of Applied Physics* **53**(12), 8497–8500 (1982).

[30] Di Giulio, M., Rella, R., Siciliano, P., and Cucurachi, S. *Vacuum* **43**(4), 305–308 (1992).

[31] Al-Ani, S. K. J. and Hogarth, C. A. *International Journal of Electronics* **58**(1), 123–131 (1985).

[32] Weng, L. and Hodgson, S. N. B. *Optical Materials* **19**(3), 313–317 (2002).

[33] Martino, M., Caricato, A. P., Fernandez, M., Leggieri, G., Jha, A., Ferrari, M., and Mattarelli, M. *Thin Solid Films* **433**(1-2), 39–44 (2003).

[34] Intyushin, E. B. and Novikov, V. A. *Thin Solid Films* **516**(12), 4194–4200 (2008).

[35] Nayak, R., Gupta, V., Dawar, A., and Sreenivas, K. *Thin Solid Films* **445**(1), 118–126 (2003).

[36] Caricato, A. P., Fernandez, M., Ferrari, M., Leggieri, G., Martino, M., Mattarelli, M., Montagna, M., Resta, V., Zampredi, L., Almeida, R. M., Concalves, M. C., Fortes, L., and Santos, L. F. *Materials Science and Engineering B-Solid State Materials for Advanced Technology* **105**(1-3), 65–69 (2003).

[37] D'Amore, F., Di Giulio, M., Pietralunga, S. M., Zappettini, A., Nasi, L., Rigato, V., and Martinelli, M. *Journal of Applied Physics* **94**(3), 1654–1661 (2003).

[38] Pierre, A., Duboudin, F., Tanguy, B., and Portier, J. *Journal of Non-Crystalline Solids* **147-148**, 569–573 (1992).

[39] Hodgson, S. N. B. and Weng, L. *Journal of Non-Crystalline Solids* **276**(1-3), 195–200 (2000).

[40] Weng, L. and Hodgson, S. *Journal of Non-Crystalline Solids* **297**(1), 18–25 (2002).

[41] Coste, S., Lecomte, A., Thomas, P., Merle-Mejean, T., and Champarnaud-Mesjard, J. C. *Journal of Sol-Gel Science and Technology* **41**(1), 79–86 (2007).

[42] Al-Kuhaili, M. F., Durrani, S. M. A., Khawaja, E. E., and Shirokoff, J. *Journal of Physics D-Applied Physics* **35**(9), 910–915 (2002).

[43] Chrisey, D. B. and Kubler, G. K. *Pulsed Laser Deposition of Thin Films.* John Wiley & Sons, New York, (1994).

[44] Afonso, C. N., Gonzalo, J., Serna, R., and Solis, J. In *Laser ablation and its applications,* Phipps, C., editor. Springer Verlag (2006).

[45] Vogel, E. M., Chase, E. W., Jackel, J. L., and Wilkens, B. J. *Applied Optics* **28**(4), 649–651 (1989).

[46] Ford, A. C., Tepper, T., and Ross, C. A. *Thin Solid Films* **437**(1-2), 211–216 (2003).

[47] Youden, K. E., Grevatt, T., Eason, R. W., Rutt, H. N., Deol, R. S., and Wylangowski, G. *Applied Physics Letters* **63**(12), 1601–1603 (1993).

[48] Afonso, C. N., Ballesteros, J. M., Gonzalo, J., Righini, G. C., and Pelli, S. *Applied Surface Science* **96-98**, 760–763 (1996).

[49] Gonzalo, J., Sanz, O., Perea, A., Fernandez-Navarro, J. M., Afonso, C. N., and Lopez, J. G. *Applied Physics A - Materials Science & Processing* **76**(6), 943–946 (2003).

[50] Sanz, O., Gonzalo, J., Perea, A., Fernandez-Navarro, J. M., Afonso, C. N., and Lopez, J. G. *Applied Physics A - Materials Science & Processing* **79**(8), 1907–1911 (2004).

[51] Munoz-Martin, D., Gonzalo, J., Fernandez-Navarro, J. M., Siegel, J., and Afonso, C. N. *Applied Surface Science* **254**(4), 1111–1114 (2007).

[52] Serna, R., de Castro, M. J., Chaos, J. A., Suarez-Garcia, A., Afonso, C. N., Fernandez, M., and Vickridge, I. *Journal of Applied Physics* **90**(10), 5120–5125 (2001).

[53] Gonzalo, J., Chaos, J. A., Suarez-Garcia, A., Afonso, C. N., and Pruneri, V. *Applied Physics Letters* **81**(14), 2532–2534 (2002).

[54] Suarez-Garcia, A., del Coso, R., Serna, R., Solis, J., and Afonso, C. N. *Applied Physics Letters* **83**(9), 1842–1844 (2003).

[55] del Coso, R., Requejo-Isidro, J., Solis, J., Gonzalo, J., and Afonso, C. N. *Journal of Applied Physics* **95**(5), 2755–2762 (2004).

[56] Suarez-Garcia, A., Serna, R., de Castro, M. J., Afonso, C. N., and Vickridge, I. *Applied Physics Letters* **84**(12), 2151–2153 (2004).

[57] Dikovska, A. O. G., Atanasov, P. A., de Castro, M. J., Perea, A., Gonzalo, J., Afonso, C. N., and Lopez, J. G. *Thin Solid Films* **500**(1-2), 336–340 (2006).

[58] Serna, R., Ballesteros, J. M., de Castro, M. J., Solis, J., and Afonso, C. N. *Journal of Applied Physics* **84**(4), 2352–2354 (1998).

[59] Fernández-Navarro, J. M. *El vidrio.* CSIC, Madrid, (2003).

[60] Saenger, K. L. *Processing of Advanced Materials* **2**, 1–24 (1993).

[61] Saenger, K. L. *Processing of Advanced Materials* **3**, 63–82 (1993).

[62] Cheung, J. T. In *Pulsed Laser Deposition of Thin Films,* Chrisey, D. B. and Kubler, G. K., editors. John Wiley & Sons, New York (1994).

[63] Willmott, P. R. and Huber, J. R. *Reviews of Modern Physics* **72**(1), 315–328 (2000).

[64] Hubler, G. K. In *Pulsed Laser Deposition of Thin Films,* Chrisey, D. B. and Kubler, G. K., editors. John Wiley & Sons, New York (1994).

[65] Afonso, C. N. and Gonzalo, J. In *Láminas Delgadas y Recubrimientos: Preparación, Propiedades y Aplicaciones,* Albella, J., editor. CSIC (2003).

[66] Fahler, S., Sturm, K., and Krebs, H. U. *Applied Physics Letters* **75**(24), 3766–3768 (1999).

[67] Gonzalo, J., Siegel, J., Perea, A., Puerto, D., Resta, V., Galvan-Sosa, M., and Afonso, C. N. *Physical Review B* **76**(3), 035435.

[68] Eason, R. *Pulsed Laser Deposition of Thin Films. Applications-Led Growth of Functional Materials.* John Wiley & Sons, Hoboken, New Jersey, (2006).

[69] Norton, D. P. In *Pulsed Laser Deposition of Thin Films. Applications-Led Growth of Functional Materials,* Eason, R., editor. John Wiley & Sons, Hoboken, New Jersey (2006).

[70] Schou, J. *Applied Surface Science* **255**(10), 5191–5198 (2009).

[71] Kelly, R. E. and Miotello, A. In *Pulsed Laser Deposition of Thin Films,* Chrisey, D. B. and Kubler, G. K., editors. John Wiley & Sons, New York (1994).

[72] Singh, R. K. and Narayan, J. *Physical Review B* **41**(13), 8843–8859 (1990).

[73] Born, M. and Wolf, E. *Principles of Optics.* Pergamon Press, Oxford, 6th (corrected) edition, (1993).

[74] http://www.rzg.mpg.de/∼mam/.

[75] http://pixe.physics.uoguelph.ca/gupix/main/.

[76] Watts, J. F. and Wolstenholme, J. *An introduction to Surface Analysis by XPS andAES.* John Wiley & Sons, (2003).

[77] Shirley, D. A. *Physical Review B* **5**(12), 4709–4714 (1972).

[78] Smith, E. and Dent, G. *Modern Raman Spectroscopy - A Practical Approach.* John Wiley & Sons, (2005).

[79] Bañares, M. A. and Valenzuela, R. X. In *Técnicas de Análisis y Caracterización de Materiales,* Faraldos, M. and Goberna, C., editors. CSIC, Madrid (2002).

[80] Bermejo, D. *Introducción a la Espectroscopía Raman.* The General Secretariat of the Organization of American States, Washington, D.C., (1988).

[81] Galeener, F. L. and Sen, P. N. *Physical Review B* **17**(4), 1928–1933 (1978).

[82] Sokolov, V. O., Plotnichenko, V. G., Koltashev, V. V., and Dianov, E. M. *Journal of Non-Crystalline Solids* **352**(52-54), 5618–5632 (2006).

[83] Boyd, R. W. *Nonlinear Optics.* Academic press, San Diego, (1992).

[84] del Coso, R. and Solis, J. *Journal of the Optical Society of America B* **21**(3), 640–644 (2004).

[85] Azzam, R. M. A. and Bashara, N. M. *Ellipsometry and Polarized Light.* Elsevier, Amsterdam, (2003).

[86] Tompkins, H. G. *A User's Guide to Ellipsometry.* Academic Press, San Diego, (1993).

[87] Neuroth, N. In *The Properties of Optical Glass,* Bach, H. and Neuroth, N., editors. Springer-Verlag, Berlin (1995).

[88] Villegas, M. A. and Fernandez-Navarro, J. M. *Journal of the European Ceramic Society* **27**(7), 2715–2723 (2007).

[89] Saito, K. and Ikushima, A. J. *Physical Review B* **62**(13), 8584–8587 (2000).

[90] Urbach, F. *Physical Review* **92**(5), 1324 (1953).

[91] Davis, E. A. and Mott, N. F. *Philosophical Magazine* **22**(179), 903–922 (1970).

[92] Mott, N. F. and Davis, E. A. *Electronic Processes in Non-Crystalline Materials.* Clarendon Press, Oxford, (1979).

[93] Rawson, H. *Properties and Applications of Glass.* Elsevier, Amsterdam, (1980).

[94] Zachariasen, W. H. *Journal of the American Chemical Society* **54**(10), 3841–3851 (1932).

[95] Wang, C. C. *Physical Review B* **2**(6), 2045–2048 (1970).

[96] Boling, N. L., Glass, Alexander, J., and Owyoung, A. *IEEE Journal of Quantum Electronics* **14**(8), 601–608 (1978).

[97] Lines, M. E. *Physical Review B* **41**(6), 3383–3390 (1990).

[98] Dimitrov, V. and Sakka, S. *Journal of Applied Physics* **79**(3), 1736–1740 (1996).

[99] Dimitrov, V. and Sakka, S. *Journal of Applied Physics* **79**(3), 1741–1745 (1996).

[100] Adair, R., Chase, L. L., and Payne, S. A. *Journal of the Optical Society of America B* **4**(6), 875–881 (1987).

[101] Lines, M. E. *Physical Review B* **43**(14), 11978–11990 (1991).

[102] Fargin, E., Berthereau, A., Cardinal, T., Le Flem, G., Ducasse, L., Canioni, L., Segonds, P., Sarger, L., and Ducasse, A. *Journal of Non-Crystalline Solids* **203**, 96–101 (1996).

[103] Mirgorodsky, A. P., Soulis, M., Thomas, P., Merle-Mejean, T., and Smirnov, M. *Physical Review B* **73**(13), 134206 (2006).

[104] Heckroodt, R. O. and Res, M. A. *Physics and Chemistry of Glasses* **17**(6), 217–219 (1976).

[105] Blanchandin, S., Marchet, P., Thomas, P., Champarnaud-Mesjard, J. C., Frit, B., and Chagraoui, A. *Journal of Materials Science* **34**(17), 4285–4292 (1999).

[106] Mirgorodsky, A. P., Merle-Mjean, T., Champarnaud, J. C., Thomas, P., and Frit, B. *Journal of Physics and Chemistry of Solids* **61**(4), 501–509 (2000).

[107] Linqvist, O. *Acta Chemica Scandinavica* **22**(3), 977–982 (1968).

[108] Sekiya, T., Mochida, N., Ohtsuka, A., and Tonokawa, M. *Journal of Non-Crystalline Solids* **144**(2-3), 128–144 (1992).

[109] Sekiya, T., Mochida, N., Ohtsuka, A., and Tonokawa, M. *Journal of the Ceramic Society of Japan* **97**(12), 1435–1440 (1989).

[110] Jeansannetas, B., Blanchandin, S., Thomas, P., Marchet, P., Champarnaud-Mesjard, J. C., Merle-Mjean, T., Frit, B., Nazabal, V., Fargin, E., Le Flem, G., Martin, M. O., Bousquet, B., Canioni, L., Le Boiteux, S., Segonds, P., and Sarger, L. *Journal of Solid State Chemistry* **146**(2), 329–335 (1999).

[111] Sekiya, T., Mochida, N., and Ohtsuka, A. *Journal of Non-Crystalline Solids* **168**(1-2), 106–114 (1994).

[112] Sekiya, T., Mochida, N., Ohtsuka, A., and Soejima, A. *Journal of Non-Crystalline Solids* **151**(3), 222–228 (1992).

[113] Sekiya, T., Mochida, N., and Ogawa, S. *Journal of Non-Crystalline Solids* **185**(1-2), 135–144 (1995).

[114] Sekiya, T., Mochida, N., and Soejima, A. *Journal of Non-Crystalline Solids* **191**(1-2), 115–123 (1995).

[115] Kalampounias, A. G., Papatheodorou, G. N., and Yannopoulos, S. N. *Journal of Physics and Chemistry of Solids* **67**(4), 725–731 (2006).

[116] Sekiya, T., Mochida, N., and Ogawa, S. *Journal of Non-Crystalline Solids* **176**(2-3), 105–115 (1994).

[117] Murugan, G. S. and Yasutake, O. *Journal of Applied Physics* **96**(5), 2437–2442 (2004).

[118] Murugan, G. S. and Ohishi, Y. *Journal of Non-Crystalline Solids* **351**(5), 364–371 (2005).

[119] Komatsu, T., Tawarayama, H., Mohri, H., and Matusita, K. *Journal of Non-Crystalline Solids* **135**(2-3), 105–113 (1991).

[120] Wells, A. F. *Structural Inorganic Chemistry.* Clarendon Press, Oxford, (1975).

[121] Lide, D. R. *CRC Handbook of Chemistry and Physics.* CRC Press, Boca Raton, (2008).

[122] Himei, Y., Osaka, A., Nanba, T., and Miura, Y. *Journal of Non-Crystalline Solids* **177**, 164–169 (1994).

[123] Rivero, C., Stegeman, R., Richardson, K., Stegeman, G., Turri, G., Bass, M., Thomas, P., Udovic, M., Cardinal, T., Fargin, E., Couzi, M., Jain, H., and Miller, A. *Journal of Applied Physics* **101**(2), 023526 (2007).

[124] Khatir, S., Romain, F., Portier, J., Rossignol, S., Tanguy, B., Videau, J. J., and Turrell, S. *Journal of Molecular Structure* **298**, 13–16 (1993).

[125] Lezal, D., Horak, J., Navratil, J., Karamazov, S., and Sklenar, A. *Physics and Chemistry of Glasses* **42**(4-5), 324–327 (2001).

[126] Kim, S. H., Yoko, T., and Sakka, S. *Journal of the American Ceramic Society* **76**(10), 2486–2490 (1993).

[127] Al-Ani, S. K. J., Hogarth, C. A., and Elmalawany, R. A. *Journal of Materials Science* **20**(2), 661–667 (1985).

[128] Hogarth, C. A. and Assadzadeh-Kashani, E. *Journal of Materials Science* **18**(4), 1255–1263 (1983).

[129] Duffy, J. A. *Journal of Solid State Chemistry* **62**(2), 145–157 (1986).

[130] Green, S. M., Piqué, A., Harshavardhan, K. S., and Bernstein, J. S. In *Pulsed Laser Deposition of Thin Films,* Chrisey, D. B. and Kubler, G. K., editors. John Wiley & Sons, New York (1994).

[131] Metev, S. In *Pulsed Laser Deposition of Thin Films,* Chrisey, D. B. and Kubler, G. K., editors. John Wiley & Sons, New York (1994).

[132] Geohegan, D. B. *Applied Physics Letters* **60**(22), 2732–2734 (1992).

[133] http://www.andor.com/.

[134] Dyer, P. E., Issa, A., and Key, P. H. *Applied Physics Letters* **57**(2), 186–188 (1990).

[135] Gupta, A. *Journal of Applied Physics* **73**(11), 7877–7886 (1993).

[136] Gonzalo, J., San Roman, R. G., Perriere, J., Afonso, C. N., and Casero, R. P. *Applied Physics A - Materials Science & Processing* **66**(5), 487–491 (1998).

[137] Gupta, A. and Hussey, B. W. *Applied Physics Letters* **58**(11), 1211–1213 (1991).

[138] Singh, R. K. and Kumar, D. *Materials Science & Engineering R - Reports* **22**(4), 113–185 (1998).

[139] Afonso, C. N., Gonzalo, J., Vega, F., Dieguez, E., Wong, J. C. C., Ortega, C., Siejka, J., and Amsel, G. *Applied Physics Letters* **66**(12), 1452–1454 (1995).

[140] Pedley, J. B. and Marshall, E. M. *Journal of Physical and Chemical Reference Data* **12**(4), 967–1031 (1983).

[141] Geohegan, D. B. In *Pulsed Laser Deposition of Thin Films,* Chrisey, D. B. and Kubler, G. K., editors. John Wiley & Sons, New York (1994).

[142] Camposeo, A., Cervelli, F., Fuso, F., Allegrini, M., and Arimondo, E. *Applied Physics Letters* **78**(16), 2402–2404 (2001).

[143] Aspnes, D. E. *Thin Solid Films* **89**(3), 249–262 (1982).

[144] Seki, H. *Applied Physics Letters* **43**(11), 1000–1002 (1983).

[145] de Sande, J. C. G., Afonso, C. N., Escudero, J. L., Serna, R., Catalina, F., and Bernabeu, E. *Applied Optics* **31**(28), 6133–6138 (1992).

[146] Palik, E. D. *Handbook of Optical Constants of Solids.* Academic Press, (1991).

[147] Stuke, J. *Journal of Non-Crystalline Solids* **4**, 1–26 (1970).

[148] Nasu, H., Uchigaki, T., Kamiya, K., Kanbara, H., and Kubodera, K. *Japanese Journal of Applied Physics* **31**(12A), 3899–3900 (1992).

[149] Borrelli, N. F., Aitken, B. G., and Newhouse, M. A. *Journal of Non-Crystalline Solids* **185**(1-2), 109–122 (1995).

[150] Noguera, O., Merle-Mejean, T., Mirgorodsky, A. P., Smirnov, M. B., Thomas, P., and Champarnaud-Mesjard, J. C. *Journal of Non-Crystalline Solids* **330**(1-3), 50–60 (2003).

[151] El-Diasty, F., Abdel-Baki, M., and Abdel-Wahab, F. A. *Optical Materials* **31**(2), 161–166 (2008).

[152] Nasu, H., Sugimoto, O., Matsuoka, J., and Kamiya, K. *Journal of Non-Crystalline Solids* **182**(3), 321–327 (1995).

[153] Sanz, O. *Síntesis y propiedades ópticas de vidrios de óxidos de metales pesados en lámina delgada obtenidos mediante depósito por láser pulsado.* PhD thesis, Universidad Autonoma de Madrid, (2005).

[154] Cardinal, T., Fargin, E., Le Flem, G., Couzi, M., Canioni, L., Segonds, P., Sarger, L., Ducasse, A., and Adamietz, F. *European Journal of Solid State and Inorganic Chemistry* **33**(7), 597–605 (1996).

[155] Canale, J. E., Condrate, R. A., Nassau, K., and Cornilsen, B. C. *Journal of the Canadian Ceramic Society* **55**, 50–56 (1986).

[156] Jehng, J. M. and Wachs, I. E. *Chemistry of Materials* **3**(1), 100–107 (1991).

[157] Ribeiro, S. J. L., Dexpert-Ghys, J., Piriou, B., and Mastelaro, V. R. *Journal of Non-Crystalline Solids* **159**(3), 213–221 (1993).

[158] Kolobkova, E. V. *Soviet Journal of Glass Physics and Chemistry* **13**(3), 352–358 (1988).

[159] Santos, L. F., Wondraczek, L., Deubener, J., and Almeida, R. M. *Journal of Non-Crystalline Solids* **353**(18-21), 1875–1881 (2007).

[160] Fukumi, K., Kokubo, T., Kamiya, K., and Sakka, S. *Journal of Non-Crystalline Solids* **84**(1-3), 100–104 (1986).

[161] Repelin, Y., Husson, E., and Brusset, H. *Spectrochimica Acta Part A* **35**(8), 937–948 (1979).

[162] Repelin, Y., Husson, E., Dao, N. Q., and Brusset, H. *Spectrochimica Acta Part A* **36**(3), 253–258 (1980).

[163] Flambard, A., Videau, J. J., Delevoye, L., Cardinal, T., Labrugre, C., Rivero, C. A., Couzi, M., and Montagne, L. *Journal of Non-Crystalline Solids* **354**(30), 3540–3547 (2008).

[164] Santran, S., Canioni, L., Sarger, L., Cardinal, T., and Fargin, E. *Journal of the Optical Society of America B* **21**(12), 2180–2190 (2004).

[165] Cardinal, T., Fargin, E., Le Flem, G., and Leboiteux, S. *Journal of Non-Crystalline Solids* **222**, 228–234 (1997).

[166] Graner, G., Hirota, E., Iijima, T., Kuchitsu, K., Ramsay, D., Vogt, J., and Vogt, N. In *Structure Data of Free Polyatomic Molecules,* Kuchitsu, K., editor, volume VII. Springer (1998).

[167] Vogel, E., Kosinski, S., Krol, D., Jackel, J., Friberg, S., Oliver, M., and Powers, J. *Journal of Non-Crystalline Solids* **107**(2-3), 244–250 (1989).

List of publications and communications

Publications directly related to the present work

- *Enhanced nonlinear optical properties of oxygen deficient lead-niobium-germanate film glasses*
  J. Gonzalo, H. Fernandez, J. Solis, **D. Munoz-Martin**, J. M. Fernandez-Navarro, C. N. Afonso, and J. L. G. Fierro
  Applied Physics Letters **90**(25), 251907 (2007).

- *Nonlinear optical response of multicomponent tellurite thin film glasses*
  D. Munoz-Martin, H. Fernandez, J. M. Fernandez-Navarro, J. Gonzalo, J. Solis, J. L. G. Fierro, C. Domingo, and J. V. Garcia-Ramos
  Journal of Applied Physics **104**(11), 113510 (2008).

- *Characterisation of glasses in the TeO_2–WO_3–PbO system*
  D. Munoz-Martin, M. A. Villegas, J. Gonzalo, and J. M. Fernandez-Navarro
  Journal of the European Ceramic Society **29**, 2903–2913 (2009).

- *Compositional, structural and optical properties of tellurite thin film glasses deposited by PLD*
  D. Munoz-Martin, J. M. Fernandez-Navarro, J. Gonzalo, S. Shen, A. Jha, J. L. G. Fierro, and C. Domingo
  In preparation

- *Structural origin of the nonlinear optical properties of lead-niobium-germanate thin film glasses*
  D. Munoz-Martin, J. Gonzalo, J. M. Fernandez-Navarro, C. Domingo, J. V. Garcia-Ramos, J. Solis, and C. N. Afonso
  In preparation

Other publications

- *Influence of surface effects on the performance of lead-niobium-germanate optical waveguides*
  D. Munoz-Martin, J. Gonzalo, J. M. Fernandez-Navarro, J. Siegel, and C. N. Afonso
  Applied Surface Science **254**(4), 1111–1114 (2007).

- *Spectroscopic properties of the 1.4 μm emission of Tm^{3+} ions in TeO_2–WO_3–PbO glasses*
  R. Balda, L. M. Lacha, J. Fernandez, M. A. Arriandiaga, J. M. Fernandez-Navarro, and **D. Munoz-Martin**
  Optics express **16**(16) 11836–11486 (2008).

- *Broadband emission of Tm^{3+}-Er^{3+} codoped TeO_2–WO_3–PbO glasses*
  R. Balda, J. Fernandez, M. Al-Saled, M. A. Arriandiaga, J. M. Fernandez-Navarro, and **D. Munoz-Martin**
  Proceedings of SPIE **7212**, 721205 (2009).

Communications to congresses presented by myself

- *Structure and optical properties of tellurite thin film glasses grown by Pulsed Laser Deposition*
  D. Munoz-Martin, J. M. Fernandez-Navarro, J. Gonzalo, J. Margueritat, J. Garcia-Lopez, C. Domingo, and J. V. Garcia-Ramos
  Oral presentation in the E-MRS 2007 Spring Meeting, Strasbourg (France), June 2007.

- *Surface effects on the performance of lead-niobium-germanate optical waveguides*
  D. Munoz-Martin, J. Gonzalo, J. M. Fernandez-Navarro, J. Siegel, J. Cortes, and C. N. Afonso
  Poster in the E-MRS 2007 Spring Meeting, Strasbourg (France), June 2007.

- *Nonlinear optical properties of Pulsed Laser Deposited TeO_2-based thin film glasses*
  D. Munoz-Martin, H. Fernandez, J. M. Fernandez-Navarro, J. Gonzalo, J. Solis, J. Garcia-Lopez, I. Ortega, and J. L. G. Fierro
  Poster in the 9^{th} International Conference on Laser Ablation (COLA'07), Tenerife (Spain), September 2007.

- *Preparation and characterization of glasses in the TeO_2–WO_3–PbO system*
  D. Munoz-Martin, M. A. Villegas, J. Gonzalo, and J. M. Fernandez-Navarro
  Poster in the 6^{th} Conference on inorganic Materials, Dresden (Germany), September 2008.

- *Optical properties of multicomponent TeO_2-based thin film glasses*
  D. Munoz-Martin, H. Fernandez, J. M. Fernandez-Navarro, J. Gonzalo, J. Solis, J. L. G. Fierro, C. Domingo, and J. V. Garcia-Ramos
  Poster in the 6^{th} Conference on inorganic Materials, Dresden (Germany), September 2008.

Communications to congresses presented by others

- *Third order nonlinear optical properties of heavy metal oxide film glasses*
  D. Munoz-Martin, H. Fernandez, J. Gonzalo, and J. Solis
  Poster in the EOS Annual Meeting 2006. Nonlinear Optics: From Sources to guided waves, Paris (France), October 2006.
  Published on Proceedings of the EOS Topical Meeting on Nonlinear Optics: From sources to guided waves, 199 (2006)

- *Structure and nonlinear optical properties of tellurite thin film glasses*
  D. Munoz-Martin, H. Fernandez, J. Margueritat, J. Solis, J. Gonzalo, and J. Garcia-Lopez
  Oral presentation in the SPIE Europe - Optics and Optoelectronics, Prague (Czech Republic), April 2007.

- *Nonlinear optical properties of heavy metal oxide film glasses produced by pulsed laser deposition*
  D. Munoz-Martin, J. Gonzalo, H. Fernandez, J. Solis, and J. M. Fernandez-Navarro
  Poster in the 8$^{\text{th}}$ International Symposium on Laser Precision Microfabrication (LPM2007), Vienna (Austria), April 2007.

- *Vidrios de teluritos para aplicaciones fotónicas*
  D. Munoz-Martin, J. M. Fernandez-Navarro, J. Gonzalo, H. Fernandez, J. Solis, J. Garcia-Lopez, J. V. Garcia-Ramos, C. Domingo, and M. A. Villegas
  Poster in the 5$^{\text{a}}$ Reunión Española de Optoelectrónica (OPTOEL'07), Bilbao (Spain), July 2007.

- *Estructura y respuesta óptica no lineal de vidrios de óxidos de metales pesados en lámina delgada*
  D. Munoz-Martin, J. M. Fernandez-Navarro, J. Gonzalo, H. Fernandez, J. Solis, J. Garcia-Lopez, J. V. Garcia-Ramos, C. Domingo, and M. A. Villegas
  Poster in the 10° Congreso Nacional de Materiales, San Sebastián (Spain), June 2008.

- *Broadband emission of Tm^{3+}-Er^{3+} codoped TeO_2–WO_3–PbO glasses*
  R. Balda, J. Fernandez, J. M. Fernandez-Navarro, **D. Munoz-Martin**, and M. Al-Saled
  Oral presentation in the SPIE Conference Photonics West 2009 (OPTO 2009), San Jose (EE.UU.), January 2009.

- *PLD of heavy metal oxide thin film glasses: How metastable structures allow improving the nonlinear optical properties?*
  D. Munoz-Martin, J. Gonzalo, J. M. Fernandez-Navarro, J. Solis, C. N. Afonso,, C. Domingo, and J. V. Garcia-Ramos
  Oral presentation in the E-MRS 2007 Spring Meeting, Strasbourg (France), June 2007.

Participation in the organization of scientific events

- 9$^{\text{th}}$ International Conference on Laser Ablation (COLA'07), Tenerife (Spain), September 2007.
  Member of the local organization committee.